Experimental Investigations of Flow Boiling Heat Transfer and Flow Instability in a Horizontal Microtube with an Inlet Orifice

Yan Feng Fan

A thesis

in

The Department

of

Mechanical and Industrial Engineering

Presented in Partial Fulfillment of the Requirements

For the Degree of Doctor of Philosophy (Mechanical Engineering) at

Concordia University

Montréal, Québec, Canada

April 2013

CONCORDIA UNIVERSITY
SCHOOL OF GRADUATE STUDIES

This is to certify that the thesis prepared

By: Yan Feng Fan

Entitled: Experimental Investigations of Flow Boiling Heat Transfer and Flow Instability in a Horizontal Microtube with an Inlet Orifice

and submitted in partial fulfillment of the requirements for the degree of

DOCTOR OF PHILOSOPHY (Mechanical Engineering)

complies with the regulations of the University and meets the accepted standards with respect to originality and quality.

Signed by the final examining committee:

Dr. Adel M. Hanna	Chair
Dr. Carolyn Ren	External Examiner
Dr. Glenn Cowan	External to Program
Dr. Hoi Dick Ng	Examiner
Dr. Rolf Wuthrich	Examiner
Dr. Ibrahim Hassan	Thesis Supervisor

Approved by

Chair of Department or Graduate Program Director

April 12, 2013

Dean of Faculty

ABSTRACT

Experimental Investigations of Flow Boiling Heat Transfer and Flow Instability in a Horizontal Microtube with an Inlet Orifice

Yan Feng Fan, Ph.D.

Concordia University, 2013

Flow boiling heat transfer mechanism has been shown to be an attractive method for satisfying the expected cooling loads of microelectronic devices. One of the main challenges associated with flow boiling is the flow instability created by the two-phase flow process. The design of orifice placed at the entrance of microchannels has been proven to be an effective way of reducing or eliminating these flow instabilities in multichannel systems.

The present thesis experimentally investigated the effect of inlet orifice in a single microtube on flow boiling heat transfer and associated flow instabilities using FC-72 as working fluid. The hydraulic diameter and length of microtube were fixed at 889 μm and 150 mm, respectively. The area ratios of inlet orifice to main microtube were selected as 50%, 35%, and 20%. The results showed that the ratio of pressure drop by inlet orifice to the total pressure drop reduced as mass flux and vapor quality increased. Inlet orifice did not have significant effects on the forced convective boiling heat transfer and normal critical heat flux, but increased the nucleate boiling heat transfer and premature critical heat flux. A novel flow stability map was developed and two critical boundaries were identified, which divide the flow into stable and unstable regimes. The microtube with 20% inlet orifice had a best performance on flow stabilization since a large upstream pressure was created. A methodology was also developed in order to predict the onset of flow instability in single microtubes with different sizes of inlet orifices. The predicted heat flux at the onset of flow instability was compared with the experiment and showed a reasonable agreement within ± 30%.

Overall, the performance of inlet orifices on flow boiling heat transfer and flow instability has been investigated in a single microtube. The present fundamental work is expected to lead to creation and development of a number of miniaturized devices, which are associated with flow boiling.

Acknowledgments

I would like to thank my supervisor Dr. Ibrahim Hassan, who has guided me throughout my graduate study at Concordia, both Master program and PhD program. It would not have been possible to achieve the work without his help and support. He not only helped me to develop my professional skill, but also believe in me at every step of the work.

I would like to thank the research colleagues I have had the pleasure of working with. Many have graduated now including Dino, Wale, Mohamed Gaber, Chad, Tarek Elnady, Tina, Mohamed Rahman, and Tariq. As well, the present research group members, Othman Hassan, Carole, Amen, Haoming Li, Yingjie Zheng, and Qian You.

In addition, I would like to thank my parents for their continuous love, support, and encouragement to go this far in my academic study. I would also like to thank my cousins and my friends, Jian Liu, Jing Chen, XinYi Tan, MengWei Gao, and Huan Wu.

The only easy day was yesterday.

Contents

List of Figures

List of Tables

Nomenclature

A = area (m^2)

C_p = thermal capacity (J/kg·°C)

D_h = hydraulic diameter (mm)

D_{inner} = inner diameter (cm)

e = wall thickness (m)

$\dot{e}$ = electrical generation rate (W/m^3)

f = frequency (Hz)

f_L = friction factor in laminar flow

f_T = friction factor in turbulent flow

G = mass flux (kg/m^2·s)

h = heat transfer coefficient (kW/m^2·°C)

h_{fg} = latent heat of vaporization (J/kg)

H = enthalpy (J/kg)

i = index

I = current (A)

k = thermal conductivity (W/m·°C)

K = pressure loss coefficient

L = tube length (mm)

L_{heated} = heated length (cm)

$\dot{m}$ = mass flow rate (kg/s)

M = total number of recorded data

N = number of data

P = pressure (kPa)

q' = heat per length (W/m)

q'' = heat flux (W/cm^2 or kW/m^2)

Q_{loss} = heat loss (W)

T = temperature (°C)

V = voltage (V)

x = distance (mm)

y = measured parameter (T or P)

Abbreviations

AMP = oscillation amplitude

AR = area ratio

CHF = critical heat flux

FS = full scale

LD = compound of Ledinegg and density-wave oscillation

LDP = compound of Ledinegg, density-wave and pressure-drop oscillation

MAE = mean absolute error

MAG = oscillation magnitude

MAX = maximum value

OFI = onset of flow instability

OSV = onset of significant void

TPD = transition instability between pressure-drop and density-wave oscillations

Subscript

acc = acceleration

ave = averaged

con = contraction

cond = conduction

conv = convection

e = exit

exp = expansion

Exp = experimental

f = fluid

fr = friction

i = location of thermocouple, from 1 to 7

in = inlet

l = liquid

lo = liquid only

m = main tube

OFI = onset of flow instability

ot = orifice tube

out = outlet

$Pred$ = predicted

ref = reference

sat = saturated

sp = single-phase

tp = two-phase

u = upstream

v = vapor

vo = vapor only

w = wall

Dimensionless Parameters

Bo = Boiling number, $Bo = q'' / (Gh_{fg})$

Nu = Nusselt number, $Nu = hD / k_f$

Re = Reynolds number, $Re = GD / \mu$

Pr = Prandtl number, $Pr = C_p \mu / k_f$

We = Weber number, $We = G^2 D / (\rho\sigma)$

Greek Letters

α = void fraction

δ = thickness

ε = uncertainty

μ = dynamic viscosity (Pa·s)

ρ = density (kg/m^3)

σ = surface tension (N/m)

χ = vapor quality

Chapter 1

1 Introduction

1.1 Background

The semiconductor technology and micro-machining methodology develop fast and has changed our lives dramatically. The applications have been widely extended to many aspects including consumer products (computer, servers, workstation, cell phone, children's toys, portable entertainment devices), military (aircraft, spacecraft, satellite) and alternative energy (solar photovoltaic cell, solar heater, fuel cell), and so on. With increasing numbers of circuits being packed into single chip and shrinking the chip dimension from room size (ENIAC* built in 1946) to micro-scale, a large amount of Joule heat is generated in a small area, which creates a high heat flux. The heat dissipation in the circuit has gone up many folds with every new design. Furthermore, these chips are confined in a tight place in the system and this creates serious problem of cooling these microelectronic chips. The poor thermal management will influence the performance of microelectronic devices in short-term (decreasing the computational speed) and long-term (degradation), and shorten the lifespan of microchips. Nowadays, the industries are facing the problem of fast removal of heat from the microelectronic chips as the required heat dissipation rate from electronic chips is touching 200 W/cm^2.

Since high power-small size scenario is prevalent in the electronic industry for many years the microprocessor cooling system should be more and more compact, efficient and should be designed as an integrated part of the cooling system. In addition, the architecture of microelectronic chip, especially microprocessor with multi-cores, induces a non-uniform heating condition. This non-uniform heat flux causes a large temperature gradient over the chip, which results in a severe thermal stress and reduces the efficiency. Therefore, the effective cooling of microelectronic devices becomes more and more important in the future to ensure the normal performance under the non-uniform heating condition.

The simplest mode of cooling any component is the air cooling. The electronic units are normally cooled down by circulating air with a fan. Since the heat transfer coefficient of air cooling is very low, the required air velocity may become comparable to sonic velocity to attain high heat flux dissipation. Further, at high fan speed the noise level will also be high, which is not desirable in the electronic systems for most of the applications. Another limit of air cooling method is caused by the limited space in the reduced size of equipment and resistance to air flow by compact packing of components in the system. Essentially, it is not possible to dissipate high heat flux from future microelectronic chips by traditional air cooling.

In place of air cooling liquid cooling can provide high heat dissipation rate from the chip as the liquids are definitely a better heat transfer media than air. This type of system will have minimum audible noise. For the heat flux of 200 W/cm^2 or more the heat dissipation by the liquid vapor phase change in the microchannels attached / machined on the chip surface is the most viable solution.

Micro heat exchangers, or micro heat sinks, use forced convection to cool a heating source, and are mainly fabricated from a silicon wafer, or copper, in which parallel grooves, varying in shape, are machined. A cover plate is placed on top of the grooves, and the result is a parallel arrangement of microchannels through which a coolant fluid may flow. The coolant may be single-phase or two-phase. However, it has been shown that single-phase liquid flow in microchannel heat sinks requires either high flow rates or smaller hydraulic diameters, consequently resulting in larger pressure drops. Therefore, two-phase microchannel heat sinks are preferable since latent heat can be used to maintain the sink at a uniform temperature. Two-phase boiling heat transfer has been chosen since the mechanism yields larger heat transfer rates and improved stream-wise uniformity in comparison to single-phase microchannel heat sinks.

Two critical limitations of flow boiling heat transfer are flow instability and critical heat flux. Flow instability of boiling heat transfer in microchannels is a very important issue since it affects the local heat transfer characteristics and may cause boiling crisis (critical heat flux and burnout), structure vibration, and system control failure. Critical heat flux (CHF) refers to the replacement of liquid being in contact with the heated surface with a vapor blanket. Typically this transition is accompanied by a large temperature jump on the surface at which boiling is occurring. Often this increase in temperature can cause burn-out or failure of equipment.

1.2 Motivation

In general, the high temperature of microelectronic devices will result in the degradation of performance. Also, the large temperature gradient over the chip surface generates high thermal stress. Flow boiling heat transfer in microchannels has advantage to achieve the high heat transfer rate and temperature uniformity. Due to the complex physical phenomena, it is necessary to conduct a comprehensive study on flow boiling in microchannels. Instead of multiple microchannels flow boiling heat transfer in single microchannel is fundamental and has significant contributions on the future development of cooling systems. However, the studies on flow boiling heat transfer coefficient, two-phase pressure drop, critical heat flux, and flow instability in single microchannel are insufficient.

The present work focuses on the fundamental research on flow boiling heat transfer in single horizontal microtube with and without inlet orifice. Chapter 2 presents an extensive literature review of flow boiling heat transfer in microchannels, including five relevant research topics. Chapter 3 presents the experimental facilities, validation of measurement, and uncertainties. Chapter 4 presents the experimental study of flow boiling heat transfer in single horizontal microtube with inlet orifice. The experimental results of heat transfer coefficient, critical heat flux, and two-phase pressure drop in the microtubes with and without inlet restriction are compared to demonstrate the effect of inlet orifice. Chapter 5 presents the experimental study of flow boiling instability, while chapter 6 proposes a methodology to predict the onset of flow instability. Chapter 7 concludes the work and highlights goals for future research.

Chapter 2

2 Literature Review

This chapter provides an extensive review of flow boiling heat transfer in microchannels. The previous studies of relevant research parameters in the area of flow boiling, such as two-phase pressure drop, heat transfer, critical heat flux, flow pattern, and flow oscillation, in single microchannel/microtube and microchannel array are reviewed and summarized. The objectives of this study are listed at the end of this chapter.

2.1 Flow Boiling in Microchannels

Extensive research is being carried out, throughout the world, to study the heat transfer using coolant like refrigerants, methanol, water etc. in the heated microchannels. In this process a number of parallel microchannels are etched on silicon wafer using photolithography or by the laser machining on the surface attached to the electronic chips. The liquid flowing in these microchannels takes away the heat generated in the electronic chips. The surface area to volume ratio of microchannel is calculated as,

$$\frac{A}{V}=\frac{2(W+H)L}{WHL}=\frac{4}{D_h} \tag{2.1}$$

where, H is the height of microchannel; W is the width of microchannel; L is the length of microchannel; D_h is the hydraulic diameter of microchannel. A large ratio of surface area to volume is achieved by reducing the hydraulic diameter to micro-scale. This assists in developing a compact and efficient design of heat exchanger. These types of systems are quiet and can be accommodated in the restricted space inside the equipment. The advantage of cooling the electronic chips by dissipating heat through the liquid flowing in the microchannels is that the heat transfer coefficient is high as it is inversely proportional to the hydraulic diameter of the channel. It is to be noted that the coolant temperature rise along the channel is very high in case of single-phase flow because all the heat generated by the electronic device is carried away by relatively small amount of liquid. Therefore, it is preferred to have a two-phase flow cooling system. Flow boiling in microchannel heat sinks offers those same attributes while providing the following important advantages over their single-phase counterparts: much higher convective heat transfer coefficients due to large latent heat during boiling; better temperature uniformity; smaller coolant flow rate. The knowledge developed in the last fifty years in two-phase flow and boiling systems for macroscale devices cannot be extended to micro geometries. Flow boiling in macrochannels is different from those in microchannels, because there is a scale effect on phase-change phenomena that is still not well addressed and understood.

2.1.1 Non-dimensional Parameters

The most widely used non-dimensional parameters in both single-phase and two-phase heat transfer are listed in Table 2.1. These parameters are useful to develop the general correlations of two-phase pressure drop, flow boiling heat transfer coefficient, and critical heat flux. Some researchers also use them to define the channel size and classify the flow patterns.

Table 2.1: Non-dimensional parameters in flow boiling heat transfer

Non-dimensional parameter	Physical meanings	Notes
Boiling number, *Bo* $Bo = \frac{q''}{Gh_{fg}}$	Ratio of the evaporation mass flux to the total mass flux in a channel	*Boiling number* is widely used in the development of heat transfer and critical heat flux correlations, and classification of flow patterns
Bond number, *B* $B = \frac{g(\rho_l - \rho_v)D^2}{\sigma}$	Ratio of buoyancy force to surface tension force.	Since the effect of gravitational force is expected to be small, *Bond number* is not expected to play an important role in microchannels.
Confinement number, *Co* $Co = \left(\frac{\sigma}{g(\rho_l - \rho_v)D^2}\right)^{1/2}$	Ratio between the surface tension force and gravity.	*Confinement number* is widely used for classification of channel size.
Capillary number, *Ca* $Ca = \frac{\mu \cdot u}{\sigma}$	Ratio of viscous to surface tension forces. It is useful in analyzing the bubble removal process.	Capillary is expected to play a critical role as both the surface tension and the viscous forces are important in microchannel flows.
Eötvös number, *Eo* $Eo = \frac{g(\rho_l - \rho_v)D^2}{\sigma}$	Ratio between gravity and surface tension force.	The same as *Bond number*
Reynolds number, *Re* $Re = \frac{\rho D u}{\mu}$	Ratio of inertial forces to viscous forces and consequently quantifies the relative importance of these two types of forces for given flow conditions.	*Reynolds number* is often used to characterize different flow regimes, such as laminar or turbulent flow.

Table 2.1 (*continued*)

Weber number, *We* $We = \frac{DG^2}{\rho\sigma}$	Ratio of inertia to the surface tension forces.	*Weber number* is useful in studying the relative effects of surface tension and inertia forces on flow patterns in microchannels.
Nusselt number, *Nu* $Nu = \frac{Dh}{k}$	Ratio of convective to conductive heat transfer across (normal to) the boundary.	*Nusselt number* is widely used for single phase liquid heat transfer.
Knudsen number, *Kn* $Kn = \frac{\lambda}{D}$ λ is the free path	Ratio of the molecular mean free path length to a representative physical length scale.	*Knudsen number* is useful for determining whether statistical mechanics or the continuum mechanics formulation of fluid dynamics should be used.
K_1 proposed by Kandlikar (2004) $K_1 = Bo^2 \frac{\rho_l}{\rho_v}$	Ratio of evaporation momentum forces to inertia force.	A higher K_1 indicates that evaporation momentum forces are dominant and are likely to alter the interface movement.
K_2 proposed by Kandlikar (2004) $K_2 = \left(\frac{q''}{h_{fg}}\right)^2 \frac{D}{\sigma\rho_v}$	Ratio of evaporation momentum forces to surface tension force.	K_2 governs the movement of interface at the contact line. The high evaporation momentum force causes the interface to overcome the retaining surface tension force.

2.1.2 Classification of Channel Size

So far, there is no classification of channel size widely accepted by the community. The classification of channel size only can be used as a mere guide indicating the size range, rather than rigid demarcations based on specific criteria. The effects of fluid properties, their variation with pressure changes, flow conditions, such as single-phase liquid or gas flow, or flow boiling, or flow condensation, operation conditions, such as mass flux/mass flow rate, heat flux, and local vapor quality, and geometries of channels, including the dimensions, cross-sectional shape, and surface roughness, will present the different classification criteria.

Kandlikar and Grande (2002) gave the classification of channel size as follows:

- Conventional channel: $D_h > 3$ mm
- Minichannel: 3 mm $\geq D_h >$ 200 μm
- Microchannel: 200 μm $\geq D_h >$ 10 μm
- Transitional channel: 10 μm $\geq D_h >$ 0.1 μm
- Transitional Microchannel: 10 μm $\geq D_h >$ 1 μm
- Transitional Nanochannel: 1 μm $\geq D_h >$ 0.1 μm
- Molecular Nanochannel: 0.1 μm $\geq D_h$

Kew and Cornwell (1997) applied the *confinement number* to define the microscale flow. The hydraulic diameter of microchannel is considered as microscale channel as the *confinement number* is in excess of 0.5, $Co > 0.5$.

Cheng and Wu (2006) classified the microchannel, minichannel, and macrochannel using *Bond number*, as follows:

- Microchannel: $Bo < 0.05$ where gravity effect can be neglected;
- Minichannel: $0.05 < Bo < 3$ where surface tension effect becomes dominant and gravitational effect is small;
- Macrochannel: $Bo > 3$ where surface tension is small in comparison with gravitational force.

Ullmann and Brauner (2007) proposed a criterion to identify the channel size on the basis of flow pattern maps using the *Eötvös number*. The channel is considered as the microscale when $Eo \leq 1.6$.

Independence of which of these criteria is better, it may say that microscale in two-phase flow might be a channel of the order of the mm instead of microns. In this work, the channel size smaller than 1 mm is considered as microchannel.

2.2 Two-Phase Pressure Drop

The two-phase pressure drop in microchannels has been experimentally investigated by many researchers. Generally, two-phase pressure drop contains three components: gravitational pressure drop, frictional pressure drop, and accelerational pressure drop. In microchannels, the gravitational pressure drop is negligible compared to the other two pressure drops. Various correlations have been proposed to predict the frictional and accelerational pressure drop. Two models are widely used for the prediction of frictional pressure drop: homogeneous model and separated model.

2.2.1 Homogeneous Model

Homogeneous model considers the two-phase flow as a single-phase flow. Two-phase flow is well mixed and no velocity difference exits between vapor and liquid phases. The slip ratio is defined as the ratio of the velocity of gas to the velocity of liquid. In the homogeneous model of two-phase flow, the slip ratio is by definition assumed to be unity (no slip),

$$S = \frac{u_v}{u_l} = \frac{U_v(1-\alpha)}{U_l \alpha} = \frac{\rho_l \chi (1-\alpha)}{\rho_v (1-\chi)\alpha} = 1 \tag{2.2}$$

where, u is the velocity; U is the superficial velocity; α is the void fraction; χ is vapor quality. The accelerational pressure drop is calculated as,

$$\Delta P_{acc} = G^2 \left\{ \left[\frac{(1-\chi)^2}{\rho_l \cdot (1-\alpha)} + \frac{\chi^2}{\rho_v \cdot \alpha} \right]_{out} - \left[\frac{(1-\chi)^2}{\rho_l \cdot (1-\alpha)} + \frac{\chi^2}{\rho_v \cdot \alpha} \right]_{in} \right\} \tag{2.3}$$

The two-phase frictional pressure drop is calculated using the equations of single-phase flow,

$$\Delta P_{fr} = f \frac{L}{D_h} \frac{G^2}{2\rho_{tp}} \tag{2.4}$$

where, L is the channel length; D_h is the hydraulic diameter; G is the mass flux; f is the Darcy friction factor. The Darcy friction factor is calculated using the two-phase *Reynolds number* expressed as,

$$Re_{tp} = \frac{G D_h}{\mu_{tp}} \tag{2.5}$$

The properties of two-phase flow, such as density and viscosity, have been evaluated using different equations. The density of two-phase flow is calculated as,

$$\rho_{tp} = \rho_l (1-\chi) + \rho_v \chi \tag{2.6}$$

or

$$\frac{1}{\rho_{tp}} = \frac{1-\chi}{\rho_l} + \frac{\chi}{\rho_v} \tag{2.7}$$

Different viscosity models were proposed and listed in Table 2.2.

Table 2.2: The two-phase viscosity correlations for homogenous model

Reference	Viscosity correlation
McAdams et al. (1942)	$\frac{1}{\mu_{tp}} = \frac{1-\chi}{\mu_l} + \frac{\chi}{\mu_v}$
Davidson et al. (1943)	$\mu_{tp} = \mu_l(1+\chi\frac{\rho_l - \rho_v}{\rho_v})$
Cicchitti et al. (1960)	$\mu_{tp} = \chi\mu_v + (1-\chi)\mu_l$
Owen (1961)	$\mu_{tp} = \mu_l$
Dukler et al. (1964)	$\mu_{tp} = (1-\beta)\mu_l + \beta\mu_v$
Beattie and Whalley’s (1982)	$\mu_{tp} = (1+2.5\beta)(1-\beta)\mu_l + \beta\mu_v$
Lin et al. (1991)	$\mu_{tp} = \frac{\mu_l\mu_v}{\mu_v + \chi^{1.4}(\mu_l - \mu_v)}$
Garcia et al. (2003)	$\mu_{tp} = \mu_l\frac{\rho_{tp}}{\rho_l}$

where, β is the volumetric quality, which is the ratio of the volume flow rate of gas/vapor to the total volume flow rate,

$$\beta = \frac{\dot{Q}_v}{\dot{Q}_t} \tag{2.8}$$

2.2.2 Separated Model

Different from homogenous model, the separated model considers the velocity ratio of vapor and liquid phases. The slip ratio is not equal to unity. The frictional pressure drop, ΔP_{fr}, is caused by the velocity gradient at the interfaces of gas/liquid, liquid/solid, and gas/solid. The accelerational pressure drop, ΔP_{acc}, is caused by the increasing vapor quality (phase change), which leads to the increased vapor velocity along the flow direction. Table 2.3 lists some correlations of frictional and accelerational pressure drops using separated model. The properties of each phase flow, such as density and viscosity, are obtained based on the saturation temperature.

Table 2.3: Separated models for two-phase pressure drop prediction

Reference	Frictional pressure drop ΔP_{fr}	Accelerational pressure drop ΔP_{acc}
Lockhart and Martinelli (1949) laminar liquid-laminar vapor	$\Delta P_{fr} = \frac{L_{tp}}{\chi_e}\int_0^{\chi_e}\frac{2f_l G^2(1-\chi_e)^2 v_l}{D_h}\Phi_l^2 d\chi_e$ $f_l\ Re_l = 24\begin{pmatrix}1-1.355\beta+1.947\beta^2 \\ -1.701\beta^3+0.956\beta^4-0.254\beta^5\end{pmatrix}$ $Re_l = \frac{G(1-\chi_e)D_h}{\mu_l}$ $\Phi_l^2 = 1+\frac{C}{X_{vv}}+\frac{1}{X_{vv}^2}$, $C = 5$; $X_{vv} = \left(\frac{\mu_l}{\mu_v}\right)^{0.5}\left(\frac{1-\chi_e}{\chi_e}\right)^{0.5}\left(\frac{v_l}{v_v}\right)^{0.5}$	$\Delta P_{acc} = G^2\left[\frac{(1-\chi)^2}{\rho_l\cdot(1-\alpha)_e}+\frac{\chi^2}{\rho_v\cdot\alpha_e}-\frac{1}{\rho_l}\right]$ $\alpha_e = 1-\frac{1}{\sqrt{1+\frac{20}{X_{vv,e}}+\frac{1}{X_{vv,e}^2}}}$
Lockhart and Martinelli (1949) laminar liquid-turbulent vapor	$\Delta P_{fr} = \frac{L_{tp}}{\chi_e}\int_0^{\chi_e}\frac{2f_l G^2(1-\chi_e)^2 v_l}{D_h}\Phi_l^2 d\chi_e$ $\Phi_l^2 = 1+\frac{C}{X_{vt}}+\frac{1}{X_{vt}^2}$, $C = 12$; $X_{vt} = \left(\frac{f\ Re_v^{0.25}}{0.079}\right)^{0.5}\left(\frac{1-\chi_e}{\chi_e}\right)\left(\frac{v_l}{v_v}\right)^{0.5}$ $Re_v = \frac{G\chi_e D_h}{\mu_v}$	$\Delta P_{acc} = G^2\left[\frac{(1-\chi)^2}{\rho_l\cdot(1-\alpha)_e}+\frac{\chi^2}{\rho_v\cdot\alpha_e}-\frac{1}{\rho_l}\right]$ $\alpha_e = 1-\frac{1}{\sqrt{1+\frac{20}{X_{vt,e}}+\frac{1}{X_{vt,e}^2}}}$
Chisholm (1973)	$\Delta P_{fr} = \frac{2f_{lo}G^2 v_l}{D_h}\frac{L_{tp}}{\chi_e}\int_0^{\chi_e}\Phi_{lo}^2 d\chi_e$ $\Phi_{lo}^2 = 1+(\Gamma^2-1)\left[B\chi_e^2(1-\chi_e)^{0.5}+\chi_e\right]$ $\Gamma = \left(\frac{\mu_v}{\mu_l}\right)^{0.5}\left(\frac{v_v}{v_l}\right)^{0.5}$	$\Delta P_{acc} = G^2\left[\frac{(1-\chi)^2}{\rho_l\cdot(1-\alpha)_e}+\frac{\chi^2}{\rho_v\cdot\alpha_e}-\frac{1}{\rho_l}\right]$ $\alpha_e = 1-\frac{1}{\sqrt{1+\frac{20}{X_{vv,e}}+\frac{1}{X_{vv,e}^2}}}$
Mishima and Hibiki (1996)	$\Delta P_{fr} = \frac{L_{tp}}{\chi_e}\int_0^{\chi_e}\frac{2f_l G^2(1-\chi_e)^2 v_l}{D_h}\Phi_l^2 d\chi_e$ $\Phi_l^2 = 1+\frac{C}{X_{vv}}+\frac{1}{X_{vv}^2}$; $C = 21\left[1-exp\left(-0.319\times10^3 D_h\right)\right]$ $X_{vv} = \left(\frac{\mu_l}{\mu_v}\right)^{0.5}\left(\frac{1-\chi_e}{\chi_e}\right)^{0.5}\left(\frac{v_l}{v_v}\right)^{0.5}$	$\Delta P_{acc} = G^2\left[\frac{(1-\chi)^2}{\rho_l\cdot(1-\alpha)_e}+\frac{\chi^2}{\rho_v\cdot\alpha_e}-\frac{1}{\rho_l}\right]$ $\alpha_e = 1-\frac{1}{1+\left(\frac{1-\chi_e}{\chi_e}\right)\left(\frac{v_l}{v_v}\right)^{2/3}}$

Table 2.3 (*continued*)

Tran et al. (2000)	$\Delta P_{fr} = \frac{2 f_{lo} G^2 v_l}{D_h}\frac{L_{tp}}{\chi_e}\int_0^{\chi_e}\Phi_{lo}^2 d\chi_e$ $\Phi_{lo}^2 = 1+\left(4.3\Gamma^2-1\right)\left[\begin{array}{l} N_{conf}\chi_e^{0.875}\left(1-\chi_e\right)^{0.875} \\ +\chi_e^{1.75}\end{array}\right]$ $\Gamma = \left(\frac{\mu_g}{\mu_l}\right)^{0.5}\left(\frac{v_v}{v_l}\right)^{0.5}$ $N_{conf} = \left[\frac{\sigma}{g\left(\rho_l-\rho_g\right)}\right]^{0.5}/D_h$	$\Delta P_{acc} = G^2\left[\frac{(1-\chi)^2}{\rho_l\cdot(1-\alpha)_e}+\frac{\chi^2}{\rho_v\cdot\alpha_e}-\frac{1}{\rho_l}\right]$ $\alpha_e = 1-\frac{1}{1+\left(\frac{1-\chi_e}{\chi_e}\right)\left(\frac{\nu_l}{\nu_v}\right)^{2/3}}$
Lee and Lee (2001)	$\Delta P_{fr} = \frac{L_{tp}}{\chi_e}\int_0^{\chi_e}\frac{2 f_l G^2\left(1-\chi_e\right)^2 v_l}{D_h}\Phi_l^2 d\chi_e$ $\Phi_l^2 = 1+\frac{C}{X_{vt}}+\frac{1}{X_{vt}^2}$ $C = 6.185\times10^{-2}\,Re_{lo}^{0.726}$ $X_{vt} = \left(\frac{f\,Re_v^{0.25}}{0.079}\right)^{0.5}\left(\left(\frac{1-\chi_e}{\chi_e}\right)\left(\frac{\nu_l}{\nu_v}\right)\right)^{0.5}$	$\Delta P_{acc} = G^2\left[\frac{(1-\chi)^2}{\rho_l\cdot(1-\alpha)_e}+\frac{\chi^2}{\rho_v\cdot\alpha_e}-\frac{1}{\rho_l}\right]$ $\alpha_e = 1-\frac{1}{1+\left(\frac{1-\chi_e}{\chi_e}\right)\left(\frac{\nu_l}{\nu_v}\right)^{2/3}}$
Yu et al. (2002)	$\Delta P_{fr} = \frac{L_{tp}}{\chi_e}\int_0^{\chi_e}\frac{2 f_l G^2\left(1-\chi_e\right)^2 v_l}{D_h}\Phi_l^2 d\chi_e$ $\Phi_l^2 = \frac{1}{X_{vt}^{1.9}}$ $X_{vt} = \left(\frac{f\,Re_v^{0.2}}{0.046}\right)^{0.5}\left(\left(\frac{1-\chi_e}{\chi_e}\right)\left(\frac{\nu_l}{\nu_v}\right)\right)^{0.5}$	$\Delta P_{acc} = G^2\left[\frac{(1-\chi)^2}{\rho_l\cdot(1-\alpha)_e}+\frac{\chi^2}{\rho_v\cdot\alpha_e}-\frac{1}{\rho_l}\right]$ $\alpha_e = 1-\frac{1}{1+\left(\frac{1-\chi_e}{\chi_e}\right)\left(\frac{\nu_l}{\nu_v}\right)^{2/3}}$
Qu and Mudawar (2003)	$\Delta P_{fr} = \frac{L_{tp}}{\chi_e}\int_0^{\chi_e}\frac{2 f_l G^2\left(1-\chi_e\right)^2 v_l}{D_h}\Phi_l^2 d\chi_e$ $\Phi_l^2 = 1+\frac{C}{X_{vv}}+\frac{1}{X_{vv}^2}$ $C = 21\left[1-exp\left(-0.319\times10^3 D_h\right)\right]$ $\left(0.00418G+0.0613\right)$ $X_{vv} = \left(\frac{\mu_l}{\mu_v}\right)^{0.5}\left(\frac{1-\chi_e}{\chi_e}\right)^{0.5}\left(\frac{v_l}{v_v}\right)^{0.5}$	$\Delta P_{acc} = G^2\left[\frac{(1-\chi)^2}{\rho_l\cdot(1-\alpha)_e}+\frac{\chi^2}{\rho_v\cdot\alpha_e}-\frac{1}{\rho_l}\right]$ $\alpha_e = 1-\frac{1}{1+\left(\frac{1-\chi_e}{\chi_e}\right)\left(\frac{\nu_l}{\nu_v}\right)^{2/3}}$
Lee and Mudawar (2005)	$\Delta P_{fr} = \frac{L_{tp}}{\chi_e}\int_0^{\chi_e}\frac{2 f_l G^2\left(1-\chi_e\right)^2 v_l}{D_h}\Phi_l^2 d\chi_e$ $\Phi_l^2 = 1+\frac{C}{X}+\frac{1}{X^2}$ $C = 2.16\,Re_{lo}^{0.047}We_{lo}^{0.6}$ for laminar liquid-laminar vapor $C = 1.45\,Re_{lo}^{0.25}We_{lo}^{0.23}$ for laminar liquid-turbulent vapor	$\Delta P_{acc} = G^2\left[\frac{(1-\chi)^2}{\rho_l\cdot(1-\alpha)_e}+\frac{\chi^2}{\rho_v\cdot\alpha_e}-\frac{1}{\rho_l}\right]$ $\alpha_e = 1-\frac{1}{1+\left(\frac{1-\chi_e}{\chi_e}\right)\left(\frac{\nu_l}{\nu_v}\right)^{2/3}}$

2.3 Critical Heat Flux

Critical heat flux is one of limiting criteria in flow boiling heat transfer. It describes the thermal limit of a phenomenon where a phase change occurs during heating, which suddenly decreases the efficiency of heat transfer, thus causing localized overheating of the heating surface. Some studies have been done to investigate and predict the critical heat flux in single and multiple microchannels.

Hall and Mudawar (2000) collected 4860 points of subcooled CHF data and proposed a correlation for water in tubes with uniform axial heat flux. The correlation based on the inlet conditions was recommended. The parametric range of inlet conditions covered $0.25 \leq D_h \leq 15$ mm, $2 \leq L/D_h \leq 200$, $300 \leq G \leq 30000$ kg/m^2·s, $1\times10^5 \leq P \leq 200 \times 10^5$ Pa, $-2 \leq \chi_i \leq 0$, and $-1 \leq \chi_e \leq 0$. The mean absolute and root-mean-square errors were 10.3% and 14.3%.

Zhang et al. (2006) proposed a new correlation of critical heat flux for flow boiling of water in small diameter tubes ($0.33 < D_h < 6.22$ mm). The collected data included subcooled and saturated CHF, totally 3837 data points (2539 points for saturated CHF). The data covered $1 < L/D_h < 975$, 0.1 MPa $< P < 19$ MPa, 5.33 kg/m^2·s $< G < 1.34\times10^5$ kg/m^2·s, 0.0935 MW/m^2 $< q''_{CHF} < 276$ MW/m^2. They analyzed the effect of parameters on CHF and determined the functional form of correlation, which included the *Weber number*, density ratio, ratio of length to diameter, and inlet vapor quality. The new correlation had a mean deviation of 16.8% for this collected database.

Wojtan et al. (2006) experimentally studied the saturated critical heat flux in single microtubes with hydraulic diameters of 0.5 and 0.8 mm. The tested refrigerants were R134a and R245fa. The heated length varied between 20 and 70 mm. They found that the

CHF increased as mass flux increased and hydraulic diameter decreased. Also CHF decreased with increasing the heated length and vapor quality. CHF was independent on the subcooled inlet temperature. At mass flux was lower than 1000 kg/m^2·s, CHF was independent on saturated temperature. At mass flux was higher than 1000 kg/m^2·s, CHF increased as saturated temperature increased. A new correlation was proposed based on the version of Katto-Ohno correlation.

Qi et al. (2007a) measured the critical heat flux in vertical microtubes using liquid nitrogen as working fluid. Four microtubes with the hydraulic diameters, 0.531, 0.834, 1.042, and 1.931 mm were selected. They found that CHF increased with increasing the mass flux and microtube diameter. They proposed a correlation based on Katto correlation and suggested to limit the use to $\rho_v/\rho_l < 0.15$.

Roday and Jensen (2009) studied the critical heat flux in single microtubes with the diameters from 0.286 to 0.7 mm. They found that CHF increased with increasing mass flux. CHF decreased as vapor quality increased in the subcooled region. However, as quality approached zero, CHF increased as vapor quality increased in the saturated region. They developed a new subcooled CHF correlation.

Wu et al. (2011) proposed one simple, non-dimensional correlation to predict the saturated critical heat flux and validated their correlation by comparing 629 data points. This correlation was based on exit vapor quality and independent on *Weber number*.

Basu et al. (2011) studied the effects of mass flux, inlet subcooling, saturation pressure, and vapor quality on CHF in single horizontal microtubes with hydraulic diameters of 0.5 mm, 0.96 mm, and 1.6 mm. R134a was selected as working fluid. They found that the CHF increased with increasing the mass flux and inlet subcooled temperature; decreased with decreasing diameter of microtube and increasing the saturated temperature. They also proposed a correlation based on their experimental data.

Bowers and Mudawar (1994) experimentally measured the critical heat flux in minichannel and microchannel heat sinks with a heated length of 1 cm. The hydraulic diameters of minichannel and microchannel were 2.54 mm and 510 μm, respectively. R-113 was used as working fluid. They found that CHF increased as mass flux increased. However, CHF was independent of the subcooled inlet temperature. The correlation was proposed which included *Weber number* and ratio of length to hydraulic diameter.

Qu and Mudawar (2004) experimentally measured the critical heat flux in microchannels using water. They mentioned that past correlations accurate at predicting the CHF in single microchannel were not suitable for multiple microchannels due to the vapor backflow and the unique features of parallel microchannels. They proposed a new correlation for parallel microchannels, which considered the density ratio, *Weber number*, and ratio of length to hydraulic diameter.

Lee and Mudawar (2009) investigated the critical heat flux for subcooled flow boiling in microchannels using HFE 7100 as working fluid. They proposed two types of CHF: normal CHF and premature CHF. For normal CHF, the abundant liquid was surrounded by the bubble. A continuous vapor blanket was observed, which thermally insulated the wall from the liquid contact. For premature CHF, the large void fraction increased the pressure drop. Vapor was forced backwards into the inlet plenum until the increased inlet pressure was capable of resisting the vapor backflow. Premature CHF was accompanied with flow instability. A new correlation was proposed based on the one from Hall and Mudawar (2000). They replaced the diameter and *Weber number* with equivalent diameter, which is a function of channel aspect ratio.

Park and Thome (2010) investigated the critical heat flux in copper multi-microchannels using three refrigerants: R134a, R236fa and R245fa. They found that the critical heat flux increased as mass flow rate increased. Critical heat flux was increased moderately with increasing inlet subcooling temperature in macrochannels. However, inlet subcooling temperature did not affect the critical heat flux in microchannels. The effect of system pressure on CHF was dependent on the flow condition and channel size.

Mauro et al. (2010) experimentally investigated the critical heat flux in a parallel straight microchannel heat sink with a split flow inlet. Three different coolants were tested. The effects of mass flow rate, saturation temperature and inlet subcooled temperature on the critical heat flux were discussed. The results showed that the critical heat flux increased with the mass flow rate increased for three working fluids. The saturation pressure had a slight influence on the critical heat flux for R134a and R236fa, but not for R245fa. The inlet subcooling affected the critical heat flux slightly at low mass flow rates and the effect became larger at high mass flow rates for R134a and R236fa. However, the opposite phenomenon was observed for R245fa. They compared their experimental results with five prediction models and showed that the models of Wojtan et al. (2006), Katto and Ohno (1984) and Revellin and Thome (2008) had better predictions within an error of ±15%.

2.4 Heat Transfer Coefficient

It is widely accepted that the saturated flow boiling in microchannels is governed by two mechanisms: nucleate boiling and forced convective boiling. In nucleate boiling, liquid near the heated channel wall is superheated to a sufficiently high degree to sustain the nucleation and growth of vapor bubbles. The heat transfer coefficient in this region is dependent upon heat flux, but is generally far less sensitive to mass velocity and vapor quality (Thome, 2004; Hassan, 2006; Kuznetsov and Shamirzaev, 2009). Nucleate boiling regime is normally associated with bubbly and slug flow patterns. Forced convective boiling regime is associated with annular flow pattern. The large heat transfer causes the suppression of bubble nucleation along the heated wall, so the heat is transferred mainly by single-phase convection through the thin annular liquid film and is carried away by evaporation at the liquid-vapor interface. The heat transfer coefficient in this region is dependent upon coolant mass velocity and vapor quality, but is fairly independent of heat flux (Lee and Lee, 2001; Qu and Mudawar, 2003; Harirchian and Garimella, 2008; Agostini et al., 2008).

Lazarek and Black (1982) experimentally investigated the two-phase heat transfer in a vertical tube with an inner diameter of 0.31 cm. R-113 was used as working fluid. The heated lengths were 12.3 and 24.6 cm. They found that the heat transfer coefficient in subcooled and saturated regimes was dependent on the heat flux. In the subcooled regime, the heat transfer coefficient increased with increasing the vapor quality. They explained that the dependence of subcooled heat transfer on the vapor quality was due to the usage of T_w - T_b, instead of ΔT_{sat}, to calculate the heat transfer coefficient. However, the heat transfer coefficient in saturated regime remained constant. The nucleate boiling was dominant. They proposed a correlation of saturated flow boiling heat transfer coefficient,

$$h_{tp,sat} = 30\, Re_l^{0.857}\, Bo^{0.714} k_l / D_h \tag{2.9}$$

In addition, they measured the critical heat flux and developed a correlation based on the inlet condition to predict the vapor quality at the onset of critical heat flux,

$$\chi_{cr} = 1 - 6.075 \times 10^{-3}\, G D_h^{0.25} \left(\frac{D_h}{L_{heated}} \right)^{0.59} \left(1 + 3.11 \left(\frac{\Delta h_i}{h_{fg}} \right) \right) \tag{2.10}$$

Tran et al. (1996) experimentally investigated the flow boiling heat transfer in single circular and rectangular microchannels using R-133 and R-12 as working fluids. The hydraulic diameter was 2.4 mm. The measurement covered a range of vapor quality up to 0.94, mass flux range of 44 - 832 kg/m^2·s, and heat flux range of 3.6 - 129 kW/m^2. Their results showed that the heat transfer coefficient was independent of the vapor quality and mass flux at $\chi > 0.2$. It indicated that the nucleate boiling was dominant boiling mechanism. At low heat fluxes (low wall superheat), the boiling mechanism transited from nucleate boiling to forced convective boiling. The cross-sectional geometry did not have effect on heat transfer coefficient. They also proposed a correlation for nucleation-dominant regime,

$$h_{tp} = 8.4 \times 10^5 \left(Bo^2 We_l \right)^{0.3} \left(\frac{\rho_l}{\rho_v} \right)^{-0.4} \tag{2.11}$$

Shin et al. (1997) measured the forced convective boiling heat transfer in a horizontal stainless steel tube with a hydraulic diameter of 7.7 mm. The effective heating length was

5.9 m. Different refrigerants (R22, R32, R134a, R290, and R600a) were tested. Heat flux varied from 10 - 30 kW/m^2 and mass flux changed from 424 - 742 kg/m^2·s. The experimental results showed strong dependence of heat transfer coefficients on the heat flux in the low vapor quality region. Nucleate boiling was dominant at the beginning of evaporation, especially for high heat flux. Heat transfer coefficient decreased as vapor quality increased ($\chi < 0.2$) since the nucleate boiling effect diminished. At $\chi > 0.2$, the heat transfer coefficient increased as vapor quality increased and became dependent on the mass flux and independent of heat flux. It indicated that the forced convective boiling became dominant and the heat transfer coefficient increased due to the increased velocity of vapor phase.

Kew and Cornwell (1997) conducted the experiment to measure the two-phase pressure drop and flow boiling heat transfer coefficient for R141b flowing through the tube with a length of 500 mm and diameters of 1.39, 2.87, and 3.69 mm. They compared their experimental data with existing correlations. The comparison showed that the existing correlations predicted the heat transfer coefficients reasonably well for the largest tube but badly for smaller microtube. Nucleate pool boiling type correlations best predicted the data. Increasing vapor quality led to an increased heat transfer coefficient.

Warrier et al. (2002) experimentally investigated two-phase heat transfer coefficient in horizontally narrow rectangular channels using FC-84 as working fluid. The hydraulic diameter was 0.75 mm and length to diameter ratio was 409.8. They proposed two correlations for subcooled and saturated boiling heat transfer coefficients:

$$\text{Subcooled: } \frac{h_{tp}}{h_{sp\_FD}} = 1 + 6Bo^{1/16} + 290\left(1 - 855Bo\right)Sc^{4.15} \qquad (2.12)$$

$$0 \le Sc \le 0.8 ; 0.00014 \le Bo \le 0.00089$$

Sc is subcooled number and calculated as,

$$Sc(z) = \left(\frac{c_{p,l}(T_{sat} - T_l)}{h_{fg}} \right)_{ONB} - \left(\frac{Q(z - z_{ONB})}{L\dot{m}h_{fg}} - x_{sc}(z) \right) \tag{2.13}$$

$$x_{sc} = \left[\left(\frac{c_{p,l}(T_{sat} - T_l)}{h_{fg}} \right)_{ONB} - Sc(z) \right]^4 \tag{2.14}$$

$$\text{Saturated: } \frac{h_{tp}}{h_{sp\_FD}} = 1 + 6Bo^{1/16} - 5.3(1 - 855Bo)\chi^{0.65} \tag{2.15}$$

$$0.03 \le \chi \le 0.55 ; 0.00027 \le Bo \le 0.00089$$

Yen et al. (2003) experimentally measured the forced convective boiling heat transfer in single stainless steel horizontal tubes with hydraulic diameters of 0.19, 0.3, and 0.51 mm using HCFC123 and FC72 as working fluids. The heat flux varied from 1 - 13 kW/m^2 and mass flux changed from 50 - 300 kg/m^2·s. They considered that high liquid superheat was attributed to the lack of active nucleate sites. The experiment showed that the heat transfer coefficient decreased as vapor quality increased at $\chi < 0.3$ and remained almost constant as vapor quality increased at $\chi > 0.3$. Also, the heat transfer coefficient was independent of mass flux, which indicated the minor effect of forced convective boiling. They explained that the obtained trend of heat transfer coefficient was caused by the size of nucleate bubble limited in the confined space. The bubble immediately attached to the inner wall as it grew. Thus, the heat transfer coefficient was suppressed under higher heat flux or mass flux conditions because of the limited evaporating space.

Kandlikar and Balasubramanian (2004) proposed a correlation of flow boiling heat transfer coefficient for laminar flow regime (Re_{lo} < 1600). This correlation was based on the single-phase liquid heat transfer coefficient. They considered two boiling mechanisms: nucleation and forced convection in their correlation.

$$h_{tp} = max\left(h_{NBD}, h_{CBD}\right) \tag{2.16}$$

$$h_{NBD} = 0.6683 Co^{-0.2}\left(1-\chi\right)^{0.8} h_{lo} + 1058.0 Bo^{0.7}\left(1-\chi\right)^{0.8} F_{FI} h_{lo} \tag{2.17}$$

$$h_{CBD} = 1.136 Co^{-0.9}\left(1-\chi\right)^{0.8} h_{lo} + 667.2 Bo^{0.7}\left(1-\chi\right)^{0.8} F_{FI} h_{lo} \tag{2.18}$$

where, F_{FI} is a fluid-surface dependent parameter. They mentioned that F_{FI} = 1 for stainless steel for all fluids.

Saitoh et al. (2005) experimentally investigated the saturated flow boiling heat transfer in three horizontal tubes with inner diameters of 0.51, 1.12, and 3.1 mm. R-134a was selected as working fluid. The mass flux varied from 150 - 450 kg/m^2·s and heat flux from 5 - 39 kW/m^2. They found that contribution of forced convective heat transfer decreased with decreasing the diameter. Dryout occurred in the lower vapor quality with decreasing diameter. They also found that the Lockhart-Martinelli correlation for two-phase pressure drop can predict well at large diameters. With decreasing diameter, the pressure drop can be predicted well by homogeneous model.

Liu and Garimella (2007) experimentally investigated the flow boiling heat transfer in the microchannels and proposed a new model to predict the heat transfer coefficient of two-phase flow. The experimental range covered the mass flow rate from 221 - 1283 kg/m^{2}s, heat flux from 96.4 - 128.8 W/cm^2. The vapor quality was limited within 0.2. The water and copper were selected as working fluid and heat sink material. The results showed that the nucleate boiling was dominant in the tested range. The wall temperature was not dependent on inlet temperature and mass flow rate, but heat flux. The superposition correlation-based model was applied,

$$h_{tp} = Fh_{sp} + Sh_{nb} \tag{2.19}$$

where, h_{sp} was the single-phase convective heat transfer; h_{nb} was the nucleate boiling heat transfer; F was the enhancement factor for convection; S was the suppression factor for nucleate boiling.

$$F = \zeta\left(\varphi_l^2\right)^{1/4}\left(\frac{\mu_{tp}}{\mu_l}\right)^{0.105}\left(\frac{C_{p,tp}}{C_{p,l}}\right)^{1/4}\left(\frac{k_{tp}}{k_l}\right)^{3/4} Pr_r^{0.167} \tag{2.20}$$

here, ζ was determined as 2 in this model; ϕ_l^2 was the two-phase multiplier.

$$\varphi_l^2 = 1 + \frac{C}{X} + \frac{1}{X^2} \tag{2.21}$$

Here, X is the Martinelli parameter; C is a constant (20 for turbulent liquid and vapor; 12 for viscous liquid and turbulent vapor; 10 for turbulent liquid and viscous vapor, 5 for viscous liquid and vapor).

$$X^2 = \left(\frac{1-\chi}{\chi}\right)\left(\frac{\rho_v}{\rho_l}\right)\left(\frac{\mu_l}{\mu_v}\right) \tag{2.22}$$

$$S = exp\left[36.57 - 55746/\left(Re_l\, F^3\right) - 3.4\, ln\left(Re_l\, F^3\right)\right] \tag{2.23}$$

$$Re_{tp} = Re_l\, F^3 \tag{2.24}$$

Saitoh et al. (2007) proposed a correlation for the saturated flow boiling heat transfer coefficient of R-134a in horizontal tubes. The proposed correlation was developed based on the Chen's model and the constant values were determined by fitting 2224 data points.

$$h_{tp} = Fh_l + Sh_{pool} \tag{2.25}$$

$$F = 1 + \frac{\left(\frac{1}{X}\right)^{1.05}}{1 + We_v^{-0.4}} \tag{2.26}$$

$$S = \frac{1}{1 + 0.4\left(Re_{tp} \times 10^{-4}\right)^{1.4}} \tag{2.27}$$

$$X = \left(\frac{1-\chi}{\chi}\right)^{0.9}\left(\frac{\rho_v}{\rho_l}\right)^{0.5}\left(\frac{\mu_l}{\mu_v}\right)^{0.1} \text{ at } Re_l > 1000, Re_v > 1000 \tag{2.28}$$

$$X = \left(\frac{16}{0.046}\right)^{0.5} Re_v^{-0.4}\left(\frac{G_l}{G_v}\right)^{0.5}\left(\frac{\rho_v}{\rho_l}\right)^{0.5}\left(\frac{\mu_l}{\mu_v}\right)^{0.5} \text{ at } Re_l < 1000, Re_v > 1000 \tag{2.29}$$

$$We_v = \frac{G_v^2 D}{\sigma\rho_v};\ Re_{tp} = Re_l\, F^{1.25}$$

$$h_{pool} = 207\frac{k_l}{d_b}\left(\frac{q''d_b}{k_l T_l}\right)^{0.745}\left(\frac{\rho_v}{\rho_l}\right)^{0.581} Pr_l^{0.533};\ d_b = 0.51\left(\frac{2\sigma}{g\left(\rho_l - \rho_v\right)}\right)^{0.5} \tag{2.30}$$

Harirchian and Garimella (2008) systematically experimentally investigated the effect of microchannel size on the local boiling heat transfer. FC-77 was selected as working fluid and the mass fluxes ranged from 250 - 1600 kg/m^{2}s. The range of microchannel width varied from 100 - 5850 μm. The depth of microchannel was maintained at 400 μm. The results showed that the heat transfer coefficient was independent of the channel size for the width of microchannel greater than 400 μm. They also found that the heat transfer coefficient was independent of the mass flux in the nucleate boiling region, but affected by mass flux in the forced convective boiling regime. The forced convective boiling became important as the channel width and mass flux decreased. The pressure drop increased as the channel size reduced and mass flux increased.

Bertsch et al. (2009) developed a new correlation of two-phase heat transfer coefficient based on Chen's model. They collected 3899 data points from 14 studies covering 12 different fluids, hydraulic diameters ranging from 0.16 - 2.92 mm, *confinement numbers* from 0.3 - 40, mass fluxes from 20 - 3000 kg/m^2·s, heat fluxes from 0.4 - 115 W/cm^2, vapor quality from 0 - 1, and the saturated temperature from -194 - 97 ºC. The correlation was proposed as,

$$h_{tp} = h_{NB} \cdot (1-\chi) + h_{conv,tp} \cdot \left[1 + 80 \cdot \left(\chi^2 - \chi^6\right) \cdot e^{-0.6Co}\right] \tag{2.31}$$

$$h_{NB} = 55 P_r^{0.12-0.2 log_{10} R_P} \left(- log_{10} P_r\right)^{-0.5} M^{-0.5} \left(q''\right)^{0.67} \tag{2.32}$$

R_P is the roughness (= 1 if unknown). *M* is the molecular mass of the fluid (kg/kmol).

$$h_{conv,tp} = h_{conv,l}(1-\chi) + h_{conv,v}\chi \tag{2.33}$$

$$h_{conv,l} = \left(3.66 + \frac{0.0668 \frac{D_h}{L} Re_l \, Pr_l}{1 + 0.04 \left(\frac{D_h}{L} Re_l \, Pr_l \right)^{2/3}} \right) \frac{k_l}{D_h} \tag{2.34}$$

$$h_{conv,v} = \left(3.66 + \frac{0.0668 \frac{D_h}{L} Re_v \, Pr_v}{1 + 0.04 \left(\frac{D_h}{L} Re_v \, Pr_v \right)^{2/3}} \right) \frac{k_v}{D_h} \tag{2.35}$$

$$Re_v = \frac{GD_h}{\mu_v}, \quad Re_l = \frac{GD_h}{\mu_l}, \; Co = \left(\frac{\sigma}{g(\rho_l - \rho_v) D_h^2} \right)^{0.5}$$

Saisorn et al. (2010) studied the flow boiling heat transfer of R-134a in a horizontal mini-tube with an inner diameter of 1.75 mm. The mass flux ranged from 200 - 1000 kg/m^2·s and heat flux from 1 - 83 kW/m^2. The saturation pressure was 8, 10, and 13 bars. Five different flow patterns were observed, slug flow, throat-annular flow, churn flow, annular flow, and annular-rivulet flow. They compared flow maps from literatures and found that the adiabatic flow map and diabetic flow map in vertical tube were not suitable for horizontal tube. They found that nucleate boiling was dominant in the tested range. The heat transfer coefficient increased with increasing the heat flux and decreased with increasing the saturation pressure. Increasing the saturation pressure reduced the liquid viscosity so that the thin liquid film on the tube wall became easily broken.

Ali et al. (2011) measured two-phase heat transfer coefficient in single vertical microtube with an inner diameter of 1.7 mm and a heated length of 220 mm. R-134a was selected as working fluid. The mass flux ranged from 50 - 600 kg/m^2·s and heat flux from 2 - 156 kW/m^2. Two system pressures corresponding to saturated temperatures of 27 °C and 32 °C were tested. The results showed that the heat transfer coefficient increased with heat flux and system pressure, and was independent of the mass flux and vapor quality before dry-out incipience. After dry-out incipience, the heat transfer coefficient decreased with vapor quality.

Bang et al. (2011) studied the effect of pressure on the flow boiling heat transfer in single microtube with an inner diameter of 1.73mm using water as working fluid. The pressures of 2 and 16 bars were tested. They mentioned that the major tend of flow boiling heat transfer in microchannels was nucleate boiling since Freon type fluids were widely used. They found that the flow boiling heat transfer mechanism was forced convection at high vapor quality. At low vapor quality, the pressure did not have effect on heat transfer coefficient. However, the heat transfer was increased by increasing the pressure at high vapor quality.

Basu et al. (2011) experimentally investigated flow boiling of R-134a in horizontal microtubes with inner diameters of 0.5, 0.96, and 1.6 mm. They found that the heat transfer coefficient increased with increasing the heat flux and saturation pressure but was independent of mass flux. The tube diameter did not have a significant effect on heat transfer coefficient. A new correlation was developed based on Tran's correlation,

$$h_{tp} = 1.44 \times 10^{5} \left(Bo^{2} We_{d}\right)^{0.32} \left(\frac{\rho_{l}}{\rho_{v}}\right)^{0.31} \tag{2.36}$$

They mentioned that the present correlation cannot predict the heat transfer well at the onset of boiling and dry-out condition.

Oh et al. (2011) experimentally investigated flow boiling heat transfer of five refrigerants (R-22, R-134a, R-410A, C_3H_8 and CO_2) in horizontal microtubes with inner diameters of 0.5, 1.5 and 3 mm. The mass flux ranged from 50 - 600 kg/m^2·s and heat flux varied from 5 - 40 kW/m^2. They found that the heat transfer coefficient was independent of mass flux but heat flux in the low vapor quality regime, and increased with increasing mass flux in the moderate-high vapor quality regime. The dominant heat transfer mechanism changed from nucleate boiling to forced convective boiling. The heat transfer coefficient dropped suddenly at high vapor quality near dry-out condition. The heat transfer coefficient increased with increasing saturation temperature due to nucleate boiling domination. A low surface tension and high pressure provided a high heat transfer coefficient. A higher heat transfer coefficient was found in a smaller tube since more active nucleate boiling occurred. They also proposed a correlation of flow boiling heat transfer coefficient,

$$h_{tp} = Sh_{NB} + Fh_l \tag{2.37}$$

$$S = 0.279\left(\phi_l^2\right)^{-0.029} Bo^{-0.098} \tag{2.38}$$

$$F = Max\left[\left(0.023\varphi_l^{2.2} + 0.76\right), 1\right] \tag{2.39}$$

$$h_{NB} = 55P_r^{0.12-0.2log_{10}Rp}\left(-log_{10}P_r\right)^{-0.5} M^{-0.5}\left(q''\right)^{0.67} \tag{2.40}$$

$$h_l = 4.36\frac{k_l}{D} \text{ if } Re_l < 2300; \tag{2.41}$$

$$h_l = \frac{\left(Re_l - 1000\right)Pr_l\left(\dfrac{f_l}{2}\right)\left(\dfrac{k_l}{D}\right)}{1 + 12.7\left(Pr_l^{2/3} - 1\right)\left(\dfrac{f_l}{2}\right)^{0.5}} \text{ if } 3000 < Re_l < 10^4 \tag{2.42}$$

where, $\phi_l^2 = 1 + \frac{C}{X} + \frac{1}{X^2}$; $X = \left(\frac{f_l}{f_v}\right)^{0.5}\left(\frac{1+\chi}{\chi}\right)\left(\frac{\rho_v}{\rho_l}\right)^{0.5}$

C = 5 for $Re_l < 2300$ and $Re_v < 2300$;

C = 10 for $Re_l > 3000$ and $Re_v < 2300$;

C = 12 for $Re_l < 2300$ and $Re_v > 3000$;

C = 20 for $Re_l > 3000$ and $Re_v < 2300$

$f = 16/Re$ for $Re < 2300$; $f = 0.079\,Re^{-0.25}$ for $Re > 3000$.

Qu and Mudawar (2003) experimentally investigated the flow boiling heat transfer in straight parallel microchannel heat sink and compared with the previous correlations of macro- and mini- channel. In the tested range, the flow transited to the annular flow abruptly near the point of zero thermodynamic equilibrium quality. This was judged from the result that heat transfer coefficient was sensitive to the mass flow rate. The heat transfer coefficient decreased with increasing the exit vapor quality and increased with increasing the mass flow rate, which was the feature of forced convective boiling heat transfer mechanism. Eleven correlations were selected and compared. The results showed that the existing correlations were unable to predict the heat transfer coefficient in microchannel correctly.

Agostini et al. (2008) experimentally tested a silicon parallel straight microchannel heat sink at heat flux up to 221 W/cm^2 using R236fa and R245fa as working fluids, whose boiling temperature is 25 °C. The saturation pressures of R236fa and R245fa were fixed at 282 kPa and 149 kPa, respectively. Five mass flow rates and up to thirty-one heat fluxes were selected as the test matrix. The results showed that the heat transfer coefficient increased with increasing vapor quality and was independent of the heat flux and mass flow rate at low heat fluxes. At medium heat fluxes, the heat transfer coefficient increased with increasing heat flux as $q^{0.67}$, was independent of the vapor quality, and increased with increasing the mass flow rate for R245fa and was independent of the mass flow rate for R236fa. At high heat fluxes, the heat transfer coefficient was independent of the mass flow rate and decreased with increasing heat flux and vapor quality. The heat transfer coefficient of R245fa was 11% higher than one of R236fa. The critical heat flux of R236fa was also investigated experimentally. The results showed that the critical heat flux increased significantly with increasing the mass flow rate. The saturation temperature and inlet subcooled temperature had minor or negligible influence on critical heat flux. The pressure drop can be predicted by the homogenous model within an error of 30%. The total pressure drop increased with vapor quality linearly and decreased with the saturation temperature.

Kuznetsov and Shamirzaev (2009) experimentally investigated the heat transfer in parallel straight microchannels at low mass fluxes. The heat sink was manufactured by stainless steel. They found that the higher subcooling of the entrance flow induced larger temperature gradient along heat sink. At mass flux of 52 $kg/m^2 \cdot s$, the nucleate boiling was dominant, which was dependent on the local heat flux, not mass flux. However, the liquid film evaporation replaced nucleate boiling to be the dominant heat transfer mechanism at the low mass flux of 17 $kg/m^2 \cdot s$.

2.5 Flow Pattern

Jiang et al. (2001) did the flow visualization in two silicon micro heat sinks with hydraulic diameters of 26 and 53 μm. The cross-section shape was triangular. Di-water was used as the working fluid. The constant inlet pressure of 240 kPa was supplied by the pressurized gas. The images showed that the bubbly flow appeared at low heat fluxes. As heat flux increased, more activities were launched and bubble growth and departure with high frequency were observed. The slug flow was found as heat flux increased. Due to the high-speed vapor velocity, only few cases were captured. As heat flux increased further, the wavy-annular flow with liquid droplets in the vapor core was observed. They found that the wavy-annular flow had a short life and the nucleation at the wall was suppressed. When the heat flux was close to the critical heat flux, the annular flow was formed. No liquid droplets were observed in the vapor core, which indicated higher temperature of vapor core than the saturation temperature. The liquid film thickness decreased as heat flux increased. The reversed flow was found due to the change of pressure drop during phase change.

Steinke and Kandlikar (2004) experimentally investigated the flow boiling in microchannels using water as working fluid. The hydraulic diameter was 207 μm. Seven flow patterns including nucleate boiling, slug flow, annular flow, annular flow with nucleation in the liquid film, churn flow, and dry-out. Flow reversal was observed. They considered that the flow reversal was caused by the presence of parallel channels, which allowed a path of lower flow resistance during explosive growth of nucleating bubbles. The flow and pressure in the other channels compensated and allowed for the high pressure of vapor generation to dissipate through the other channels. The dry-out condition was caused by the fast evaporation of liquid film in the contact line region. The interface moved backwards into the inlet. The heat transfer coefficient at all tested mass fluxes decreased with increasing the vapor quality. At low mass fluxes, the heat transfer coefficient was dependent on the heat flux. However, the heat transfer coefficient became independent of heat flux at high mass fluxes.

Revellin and Thome (2007) proposed a diabatic flow pattern map. This map was built for R-134a and R-245fa in a horizontal microtube with inner diameter ranging from 0.5 - 0.8 mm. The mass flux and heat flux varied in the ranges of 210 - 2094 kg/m^2·s and 3.1 - 597 kW/m^2, respectively. This flow pattern included four regimes: isolated bubble regime (IB), coalescing bubble regime (CB), annular regime (A), and partially dry-out regime (PD). The transition curves between two regimes were expressed as,

$$\chi_{IB/CB} = 0.763\left(\frac{Re_{lo}\, Bo}{We_{vo}}\right)^{0.41} \tag{2.43}$$

$$\chi_{CB/A} = 0.00014\, Re_{lo}^{1.47}\, We_{lo}^{-1.23} \tag{2.44}$$

$$\chi_{A/PD} = 0.437\left(\frac{\rho_v}{\rho_l}\right)^{0.073} We_{lo}^{-0.24}\left(\frac{L}{D}\right)^{-0.72}\frac{4L}{D} \tag{2.45}$$

Lee and Mudawar (2008) investigated the subcooled flow boiling in microchannels with four different hydraulic diameters, 176, 200, 334, and 416 μm. HFE 7100 was selected as the working fluid. Two inlet temperatures of 0 and -30°C was tested, and outlet pressure was kept a constant of 1.138 bar. The mass flux and heat flux varied from 670 - 6730 kg/m^2·s and 0 - 750 W/cm^2, respectively. The flow visualization was performed to capture the flow patterns. The bubbly flow was dominant at low heat fluxes.

The reversed-annular flow was observed at the critical heat flux condition. Reducing inlet temperature increased superheat of wall temperature, delayed the onset of flow boiling, and increased the critical heat flux. The bubbles grew faster as the hydraulic diameter of microchannel reduced. The visualization also revealed that the reversed flow caused the flow instability and premature critical heat flux. They proposed that the premature critical heat flux could be prevented by increasing the upstream pressure or decreasing the inlet temperature.

Harirchian and Garimella (2009) experimentally investigated the effects of channel dimension, heat flux and mass flux on the flow pattern by visualization. The experiment was carried out at four mass fluxes ranging from 225 - 1420 $kg/m^2 \cdot s$ using FC-77 as working fluid. The channel depth was fixed at 400 μm and width varied from 100 - 5850 μm. The comprehensive flow patterns were discussed at different mass fluxes and heat fluxes. The observed flow pattern was classified as bubbly flow, slug flow, churn flow, wispy-annular, and annular flow, and reversed-annular flow. They found that, no bubbly flow was observed in smaller channels. The flow patterns in the microchannels whose width was smaller than 400 μm were similar. The flow patterns in microchannels whose width was greater than 400 μm were similar, but different from the previous ones. As channel width increased, the slug flow and wispy-annular flow disappeared. As mass flow rate increased, the bubbles became smaller and more elongated in bubbly flow regime. In the microchannels with width smaller than 400 μm, the nucleate sites were suppressed at a relatively low heat flux. The new flow pattern map was created. The flow pattern transited from bubbly or slug flow to intermittent churn/wispy-annular or churn/annular flow occurred at a larger vapor quality or a larger vapor superficial velocity as channel became smaller.

Park et al. (2009) tested the effect of the inlet orifice on saturated CHF and flow pattern using R134a, R236fa, and R245fa as working fluids. Two copper multiple microchannels heat sinks with cross-sectional dimensions of 467 × 4052 μm and 199 × 756 μm were manufactured. They observed that the flow easily went back into the inlet plenum in the absence of orifice. The reversed bubble quickly moved to one of the adjacent channel and broke down into smaller parts before entering these channels. The bubble recirculation in the inlet plenum was observed. The non-uniform flow patterns amongst the channels were observed implying the mal-distribution of flow in parallel multiple microchannels. In addition of orifice, the reversed flow from the position of onset of boiling was blocked, thus suppressing instability. The reversed flow at the exit of orifice made a recirculation loop. Bubble recirculation near the inlet formed an elongated bubble zone at high heat fluxes. As inlet fluid was highly subcooled, the flow out of the orifice took a form of a liquid jet without flashing to pass through the elongated bubble zone near the exit of orifice. At low subcooled condition, the flashing was observed, which was caused by the pressure drop through the orifice. Hence, the fluid entering the channel was two-phase mixture. The flashing effect reduced the wall temperature overshoot for the onset of boiling as well as providing a spatially more uniform wall temperature distribution.

Celata et al. (2011) did the flow boiling visualization of FC-72 in a single microtube with inner diameter of 0.48 mm. The mass flux ranged from 50 - 3000 kg/m^2·s. Five flow patterns were observed, bubbly flow, bubbly/slug flow, slug flow, slug/annular flow, and annular flow. They proposed a flow instability map which showed the linear boundaries between the stable and unstable regimes. The heat transfer coefficient was independent of the mass flux and vapor quality at $\chi_e < -0.1$, which indicated the dominated nucleate boiling. The forced convective boiling became dominant at $\chi_e > -0.1$. They also found that the flow instability did not influence the heat transfer coefficient.

Choi et al. (2011) visualized the flow boiling behaviors in hydrophilic and hydrophobic microchannels. The DI-water was using as the working fluid. The hydraulic diameter was 505 μm. Two mass fluxes of 25 and 75 kg/m^2·s were tested. The heat flux varied from 10 - 430 kW/m^2. They found that a much higher number of bubbles generated in the hydrophobic microchannel. Also, the moving bubbles in the hydrophobic microchannel were unstable. The bubble inception in the liquid film was detected. The reversed flow occurred in both hydrophilic and hydrophobic microchannels.

Galvis and Culham (2012) did the water boiling visualization in two single horizontal microchannels with cross-sections of 198 × 241 and 378 × 471 μm. Four mass fluxes were tested, 350, 700, 1000, and 1300 kg/m^2·s. The outlet pressure was set at atmospheric pressure and inlet temperature was fixed at 50 °C. Six flow patterns were observed, bubbly flow, slug flow, churn flow, annular flow, wavy-annular flow, and reversed-annular flow. They also found that the flow reversal was caused by the vapor expansion in the upstream direction. The oscillating pressure drop occurred during the intermittent flow pattern. The amplitude of oscillations in the pressure drop and channel wall temperature increased with increasing the heat flux and can be attributed to the growth of confined bubbles, re-wetting, and flow reversal. The heat transfer was dominated by nucleate boiling in the smaller microchannel. However, the heat transfer was controlled by the combination of nucleate boiling and forced convective boiling in the lager microchannel.

2.6 Flow Instability

Flow boiling heat transfer is always accompanied with the flow instability due to the bubble detachment from walls, bubble growth, and bubble leaving from the microchannel. Flow boiling instability in microchannels is a very important issue since it affects the local heat transfer characteristics and may cause boiling crisis (critical heat flux and burnout), structure vibration, and system control failure. Therefore, it is crucial to evaluate flow instabilities to ensure system normal operation and safety. Researchers have been investigating this topic in various ways; some have devoted their efforts on vertical or horizontal single tubes while others focused on multiple microchannels.

Single mini/micro tube:

Boure et al. (1973) reviewed the two-phase flow instabilities. They classified the flow instabilities as static instabilities including the Ledinegg instability and flow pattern transition instability, and dynamic instabilities including the acoustic/pressure wave oscillation, density-wave oscillation, and thermal oscillation. The pressure-drop oscillation was considered as the compound of static instability and dynamic instability. The mechanisms and features of different flow oscillations are listed in Table 2.4.

Wang et al. (1994) experimentally studied the density-wave type oscillation in a vertical minichannel with a diameter of 16 mm. The frequency and amplitude of density-wave oscillation were relative to the mass flux, inlet subcooling, and system pressure. The amplitude of mass flow rate oscillation was quite large and flow reversal occurred during the oscillation. Increasing the system pressure effectively reduced the density difference between the vapor and liquid phases. Therefore, a higher heat can be input without experiencing density-wave oscillation. Also, increasing the mass flux delayed the onset of density-wave oscillation.

Ding et al. (1995) investigated dynamic instabilities of boiling two phase flow in a stainless steel horizontal microtube with a diameter of 10.9 mm. The experiment was carried out in the range of mass fluxes from 75 - 1050 kg/m^2s, heat fluxes from 0 - 100 kW/m^2, and fluid inlet temperature from 2 - 24 °C. Three types of dynamic instabilities were observed: pressure-drop oscillation, density-wave oscillation and thermal oscillation. Wang et al. (1996) found a new type of dynamic instability in an upflow system: the boiling onset oscillation, which started at the boiling point of working fluid and featured as lower frequency and larger amplitude than density-wave and pressure-drop oscillations. This oscillation occurred at low heat fluxes. As decreasing the inlet subcooling temperature, the boiling onset oscillation vanished.

Kennedy et al. (2000) experimentally investigated the onset of flow instability in horizontal microchannels with uniform heating condition. Two diameters of 1.17 mm and 1.45 mm copper microtubes were tested. They compared the experimental data with the correlation. The results showed that the heat flux at the onset of flow instability is approximately equal to the 90% of bulk exit saturation heat flux within an error of 6.9%. Diaz and Schmidt (2007) tested the flow boiling heat transfer in a vertical microchannel with a cross-section of $0.3 \times 12.7\ mm^2$. The heat flux was set up to 400 kW/m^2 and the mass flux was from 50 - 500 kg/m^2s. The results showed that the maximum amplitude of flow oscillation was observed in the subcooled boiling region. The heat transfer coefficient for water decreased with increasing vapor quality and depended on the heat flux, which indicated the dominance of nucleate boiling. However, the heat transfer coefficient for ethanol flow increased with increasing vapor quality at low heat fluxes, which was different with water flow.

Huh et al. (2007) studied the flow boiling instabilities in a rectangular single horizontal microchannel. The deionized water was used. The hydraulic diameter was 103.5 μm and the length of microchannel was 40 mm. The heated length was 30 mm. The tested mass fluxes and heat fluxes were from 170 - 360 kg/m^{2}s and 200 - 530 kW/m^2, respectively. The results showed that there was a phase difference between the pressure drop and mass flux fluctuation. This phenomenon was considered due to the pressure build-up at the inlet until the inlet pressure reached to a sufficiently high value to force the flow move downwards. The period of fluctuation lengthened and amplitude became larger as heat flux increased. The mass flow rate suddenly increased and the wall temperature decreased as the inlet pressure reached the maximum. The fluctuations of the wall temperature and mass flux were out of phase whereas the heat flux fluctuated in phase with mass flux. At high mass fluxes and high heat fluxes with low wall temperature, the bubbly/slug flow was observed. Elongated bubbles appeared as heat flux increased. As mass flux decreased, the elongated slug bubble started to move backwards into the inlet. The reversed flow occurred, which caused the increased inlet pressure.

Barber et al. (2009) experimentally studied the flow boiling instability in a vertical rectangular microchannel with a hydraulic diameter of 727 μm. The heat flux and mass flow rate were fixed at 4.26 kW/m^2 and 1.13×10^{-5} kg/s, individually. The de-wetting was observed at the edge of the microchannel wall and caused the interface oscillation of

Table 2.4: Summary of different types of flow instabilities

Classification	Type	Mechanism	Characteristics
Static instabilities	Ledinegg instability	Internal characteristics steeper than external characteristics in a negative slope region	Flow undergoes sudden, large amplitude excursion to a new stable operating condition
	Flow pattern transition instability	Bubbly flow has less void but higher pressure drop than annular flow	Cyclic flow pattern transition and flow rate variations
Dynamic instabilities	Density-wave oscillations	Delay and feedback effects in relationship between flow rate, density, and pressure-drop	Frequencies related to transit time as a continuity wave
	Pressure-drop oscillations	Dynamic interaction between channel and compressible volume	Very low frequency periodic Process
	Thermal oscillations	Interaction of variable heat transfer coefficient with flow dynamics	High magnitude temperature oscillations in the solid due to transitions between different boiling regimes
	Parallel channel instability	Interaction among parallel channels	Various modes of flow redistribution

slug flow. A bubble was produced in the bulk flow due to the perturbation and deformation of interface of slug flow. The vapor recoil was considered as the dominant effect to generate the reversed flow and thermocapillary instability. The high wall temperature led to the strong evaporation, which caused the instability of the thin liquid film at the wall.

Many researchers have been denoting their efforts on flow stabilization during boiling heat transfer in microchannels. The synthetic jet was applied to stabilize the flow (Fang et al., 2011). The synthetic jet was driven by AC power and no fresh flow was needed. The effects of synthetic jet and throttling valve on flow instability were tested. The synthetic jet introduced momentum helped to push and pull the nucleating bubbles. The bubble detached from the wall at a smaller diameter. The results showed that increasing the frequency of synthetic jet can improve the stabilization. The combination of synthetic jet and throttling valve was able to stabilize the flow. Some groups investigated the seed bubble technique in the microchannels from the upstream to change the flow pattern of boiling (Xu et al., 2009 and Liu et al., 2010). The results showed that the seed bubbles had no influence on the flow and heat transfer in the subcooled liquid flow and vapor flow at high-vapor-mass qualities. However, seed bubbles changed the flow pattern of superheated liquid flow and unsteady boiling flow to the quasi-steady boiling flow. Heat transfer was enhanced. Also, increasing the seeding frequency of bubbles was able to decrease the surface temperature.

Multiple microchannels:

Wu and Cheng (2003) investigated the periodic boiling in silicon parallel microchannels of trapezoidal cross-section with the hydraulic diameters of 158.5 and

82.8 μm. They presented the alternation of single-phase flow and two-phase flow with time in the microchannels, and estimated the large-amplitude/long-period boiling fluctuations of wall temperature, fluid temperature, pressure and mass flux with time. The mass flux changed by changing heat flux since the temperature could change the fluid properties. They explained that the fluctuation was caused by the alternation between pressure drop and mass flux since they applied pressure-driven flow. At smaller microchannels, the bubbly flow, slug flow, churn flow and other peculiar two-phase flow were observed. Next year, this group, Wu and Cheng (2004), found three periodic boiling modes: liquid/two-phase, continuous two-phase and liquid/two-phase/vapor alternation flows as the heat flux increased. The results showed that the maximum temperature oscillation appeared at the inlet in all tested cases from 61.1 - 80.5 °C corresponding to the heat flux ranging from 13.5 - 22.6 W/cm^2.

Muwanga et al. (2007) studied flow boiling instability characteristics of straight and cross-linked microchannel heat sinks. Each design consisted of 45 microchannels. Channels were etched in a silicon substrate with a width of 269 μm, height of 283 μm, and a cross-linked width of 269 μm. Distilled water was used as the working fluid. Tests were carried out at mass fluxes ranging from 91 - 228 kg/m^2·s and inlet temperatures of 70 °C and 80 °C for the straight microchannel heat sink, while an inlet temperature of 70 °C and a mass flux of 137 kg/m^2·s were used for the cross-linked microchannel heat sink. They concluded that the frequency of oscillations depended on the heat flux, flow rate, and inlet subcooling. Results showed that the straight microchannels had higher inlet pressure amplitudes than the cross-linked microchannels, while the straight microchannels had lower inlet and outlet temperature amplitudes than the cross-linked microchannels.

Wang et al. (2007) generated a flow map to state the stable and unstable flow boiling conditions. They found that the stable flow boiling with no periodic oscillation existed at $q/G < 0.96$ kJ/kg, unstable flow boiling regime with long-period oscillation (more than 1 s) ranged at 0.96 kJ/kg $< q/G <$ 2.14 kJ/kg, and unstable flow boiling regime with short-period oscillation (less than 0.1 s) existed at $q/G >$ 2.14 kJ/kg for inlet water temperature of 35 °C. At stable flow boiling regime, the isolated bubble grew, elongated, coalesced, and expanded in both upstream and downstream with decreasing mass flux under constant heat flux. At the long-period oscillation, the bubbly flow changed to annular/mist flow due to rapid bubble expansion. They found that the oscillation period of temperature was dependent only on the heat-to-mass flux ratio, but independent of the heat flux. At the short-period oscillation, the backward expansion of bubble entered to the deeper inlet plenum and mixed with subcooled liquid. The condensation of bubbles caused the oscillation. The frequency of inlet pressure oscillation increased with increasing heat flux, but was independent of mass flux.

Orifice has been proven to be a passive method to stabilize the flow during flow boiling in microchannels. Wang et al. (2008) proposed three types of inlet and outlet configurations and experimentally investigated the effects on the flow boiling instability in a parallel microchannel heat sink with trapezoidal cross-section. The area ratio of orifice to the microchannel was 20%. The results showed that the reversed flow was eliminated by the orifice which reduced the flow oscillation. However, the pressure drop was increased due to the restriction. Also, the orifice delayed the onset of flow boiling.

Kandlikar et al. (2006) addressed the basic causes of instabilities and studied the effects of pressure drop elements and fabricated nucleation sites on the flow reversal phenomenon and the corresponding heat transfer performance of the microchannels. Six parallel microchannels were machined on the copper block and water was selected as working fluid. The channel depth and width were 197 μm and 1054 μm with a hydraulic diameter of 332 μm. They proposed that the rapid expansion of bubbles was one of the main factors resulting in the flow instability. As a bubble nucleated in the superheated liquid environment, the evaporation rate was very high due to release of the liquid superheat at the bubble interface. The superheated liquid adjacent to the bubble transferred heat to the bubble. The bubble grew to fill the channel and expanded in the reverse direction to the overall flow direction. The introduction of vapor into the inlet manifold was considered as the main source of instability during flow boiling. The pressure drop elements were positioned at the inlet of each microchannel with two area reductions of 51% and 4%. The results showed that the pressure drop element with 51% area reduction cannot eliminate the reversed flow completely but reduced the severity of backflow. Pressure drop element of 4% area reduction was able to eliminate the instability completely with a significantly increased pressure drop.

Park et al. (2009) experimentally investigated the effect of orifice on the saturated critical heat flux in parallel straight microchannel heat sink. Two copper microchannel heat sinks with different dimensions of microchannels were manufactured. Three refrigerants were used as working coolant. Flow visualization was observed to show the flow pattern in order to understand the effect of orifice. The results showed that the bubbles flowed backwards into the inlet plenum without orifice, which created the flow instability. However, the reversed flow was blocked by the orifice, thus suppressing the instability. Also, a stable recirculation flow was observed in the microchannels with orifice. Comparing with the microchannel heat sink without orifice, the critical heat flux was increased by the orifice. Boiling occurred at lower heat flux.

The prediction of onset of flow instability is necessary to prevent the system vibration and burnout. The measurements of the onset of flow instability in single channel have been conducted (Siman-Tov et al., 1995; Stelling et al., 1996; Kennedy et al., 2000; Roach et al. 1999; Whittle and Eogran, 1967). The widely applied experimental procedure is to keep constant heat flux and reduce the coolant mass flux with constant inlet temperature to obtain the demand curve (ΔP-G curve). The onset of flow instability is defined as the minimum point on the demand curve. Siman-Tov et al. (1995) experimentally studied the subcooled flow instability in a vertical upward rectangular channel. The test to capture the onset of flow instability was conducted by fixing the flow rate and increasing the heat flux. The flow instability was detected at the minimum point of demand curve. Stelling et al. (1996) measured the onset of flow instability for downward subcooled flow in vertical conventional channels with hydraulic diameters from 9 to 28 mm. They considered that the flow instability occurred as the minimum in demand curve reached. A model was also proposed to predict the onset of flow instability. Kennedy et al. (2000) measured the onset of flow instability in circular tubes with hydraulic diameters of 1.17 and 1.45 mm. The tubes were placed horizontally. The results showed that the heat flux at the onset of flow instability was about 90% of the bulk exit saturation heat flux, which indicated subcooled flow instability. However, Roach et al. (1999) did the experiment using the same facility as Kennedy et al. (2000) at lower mass fluxes. The heat flux at the onset of flow instability was 10% higher than the bulk exit saturation heat flux. Whittle and Forgan (1967) carried out the experiment of OFI measurement in both rectangular and circular conventional channel, and proposed a correlation based on their experimental data. They mentioned that the method of assessing excursive-flow instability only applied to the non-throttled systems. If the throttling system was present, the system would be more stable than the prediction by the proposed method. It cannot be used for throttling system unless the new demand curve was acquired.

The widely accepted method to predict the onset of flow instability is to consider the onset of flow instability (OFI) as same as the onset of significant void (OSV) since they are very close. The theoretical models to predict the bubble departure from heated wall have been developed. The various flow conditions were covered in the previous studies such as stable flow (Levy, 1967; Staub, 1968; Rogers et al., 1987) and transient flow (Lee and Bankoff, 1993; Khater et al., 2007). These models are based on two restraints: hydrodynamic and thermal. The hydrodynamic restraint is that the sum of forces tending to detach the bubble from the surface exceeds the sum of forces holding it on the surface at bubble departure. The typical forces on the bubbles include the drag force/frictional force, buoyancy force, and surface tension force. The thermal restraint is that the temperature at the top of bubble should be at least equal to the saturation temperature for bubble departure. The empirical models have also been developed (Saha and Zuber, 1974; Ahmas, 1970; Sekoguchi et al., 1974; Unal, 1975). Lee and Bankoff (1998) compared the theoretical and empirical models of onset of significant void. It showed that the correlation of Saha-Zuber (1974) was best to predict the OSV in vertical subcooled boiling flow.

The above-mentioned models only consider the subcooled flow in vertical conventional channels. Chedester and Ghiaasiaan (2002) stated that the models and correlations developed in convectional channels were not suitable for microchannels. They proposed a hydrodynamic-controlled model to predict OSV for turbulent flow in the microtube and compared with the experimental data (Inasaka et al., 1989). Farhadi (2009) proposed an analytical model to predict the onset of Ledinegg instability in vertical two-phase flow system under both upflow and downflow conditions. The major work focused on the prediction of pressure drop, which was based on the separated model, in a heated microchannel. The slope of pressure drop to flow rate can be obtained by differentiation. The onset of Ledinegg instability was determined as the slope of internal curve was smaller than the external curve.

2.7 Summary and Objectives

- Flow boiling heat transfer can acquire a large heat transfer coefficient with small power consumption since phase change is the main heat transfer mechanism. A large amount of researches related to flow boiling in a single microchannel and microchannel array have been conducted. Due to the complex phenomena of flow boiling, many problems still remain.
- Critical heat flux (CHF) constricts the applications of flow boiling heat transfer since it will lead to the cooling failure. New methods to increase the critical heat flux need to be developed.

- Flow instabilities, one of the limiting criterions, are undesirable in microchannel heat sinks as they may cause system vibration, boiling crisis (dry-out) and system control failure. More work is necessary to study the flow instability. Novel scheme is required to stabilize the flow.
- Inlet orifices have proven to be an efficient method on flow stabilization. The previous studies of the performance of inlet orifices were limited to multiple microchannels. Fundamental studies to understand the effect of orifice sizes on flow instability in single microtube are necessary for achieving passive control of flow oscillation.
- Prediction of onset of flow instability have been developed by considering the onset of flow instability as same as the onset of significant void. Some correlations have also been proposed. However, no convenient and general prediction methodology exits.

The objectives of this work are:

- To explore the effects of inlet orifices on the critical heat flux, two-phase pressure drop, and heat transfer coefficient in single horizontal microtube.
- To fundamentally investigate the effect of inlet orifice on the onset of flow boiling instability. It will aim to provide a guide to select the size of the orifice for micro heat sink designs.
- To create a flow stability map presenting the stable and unstable flow operation ranges.
- To study the features of flow instability at different heat and mass fluxes, and quantify the flow instability by oscillation frequency, amplitude, and magnitude.

- To develop a methodology to predict the onset of flow instability in single horizontal microtube.
- To provide experimental data for the future correlations and analytical models of the heat transfer coefficient, two-phase pressure drop, and critical heat flux in both single microchannel and multiple microchannels.

Chapter 3

3 Experimental Investigations

3.1 Facility

The test facility is shown in Figure 3.1. The major test rig comprises a closed flow loop, a degassing loop, and a data acquisition system. The dielectric FC-72 is selected as the working fluid and stored in a tank. A 1 kW heater (TEMPCO, TSP02228), connected to the power supply (Staco Energy Products Company, 3PN501B) is submerged in the FC-72 tank to heat the working fluid in the degassing process. The flow loop is driven by a magnetically coupled gear pump (Cole-Parmer, 75211-22). The pump is equipped with a variable speed drive allowing up to 250 ml/min of flow rate, with a maximum pressure of 517 kPa (75 psi). A 15 µm filter (Swagelok, SS-4TF-15) is mounted before the flow meters to filter out the small particles. Three rotameters (Omega, FL-1463-S, FL-1445-G and FL-1446-S) are used to measure the different ranges of volume rates. A heat exchanger installed before the entrance to the test-section is used for degassing and preheating the FC-72 in the experiment. The FC-72 exits the test-section and returns to

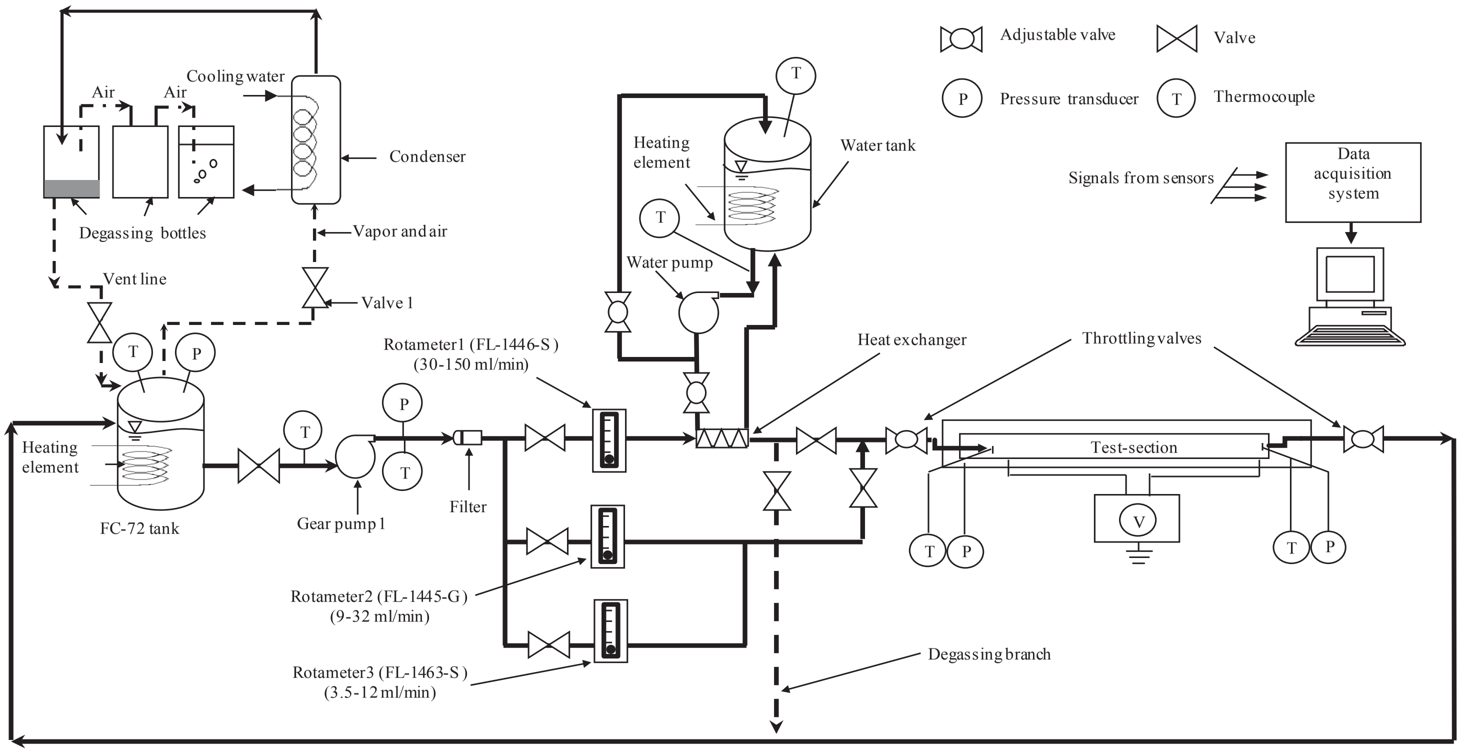

Figure 3.1: Experimental facility.

the tank. Water is heated by a 1.5 kW immersed heater (TEMPCO, TSP02244) which is connected to a power supply (Staco Energy Products Company, 3PN1010B). A water pump is used to circulate the hot water through the heat exchanger. DC power is used to supply the heat flux to the test-section. Two pressure transducers (Omega, PX01C1-075GV and PX02C1-050GV) and T-type thermocouples (Omega, TQSS-116G-6) are used to measure pressures and temperatures at the inlet and outlet. The measured signals are recorded by a data acquisition system from National Instrument Company. All uncertainties of measured and calculated parameters are listed in Section 3.5.

3.2 Test-Section

The schematic of the present microtube package is shown in Figure 3.2. Four stainless steel microtubes are selected; their inner diameter ranges from 400 μm to 889 μm. The dimensions of the microtubes are listed in Table 3.1. The microtube with an inner diameter of 889 μm is used as the main channel. The remaining three microtubes are connected individually to the main channel in order to achieve the inlet restriction structure. The acrylic supports are designed to hold the microtubes. The hydraulic fittings

Table 3.1: Dimensions of microtubes

Nominal Name	D_{ot} (mm)	Uncertainty (mm)	D_m (mm)	Area ratio $(D_{ot}/D_m)^2$	Uncertainty of area ratio
Single microtube	0.889	± 0.0254	0.889	100%	
50% orifice	0.635	± 0.0127		51%	± 3.6%
35% orifice	0.5334	+ 0.0254/-0.0127		36%	+ 4.0%/-2.7%
20% orifice	0.4064	± 0.01905		21%	± 2.3%

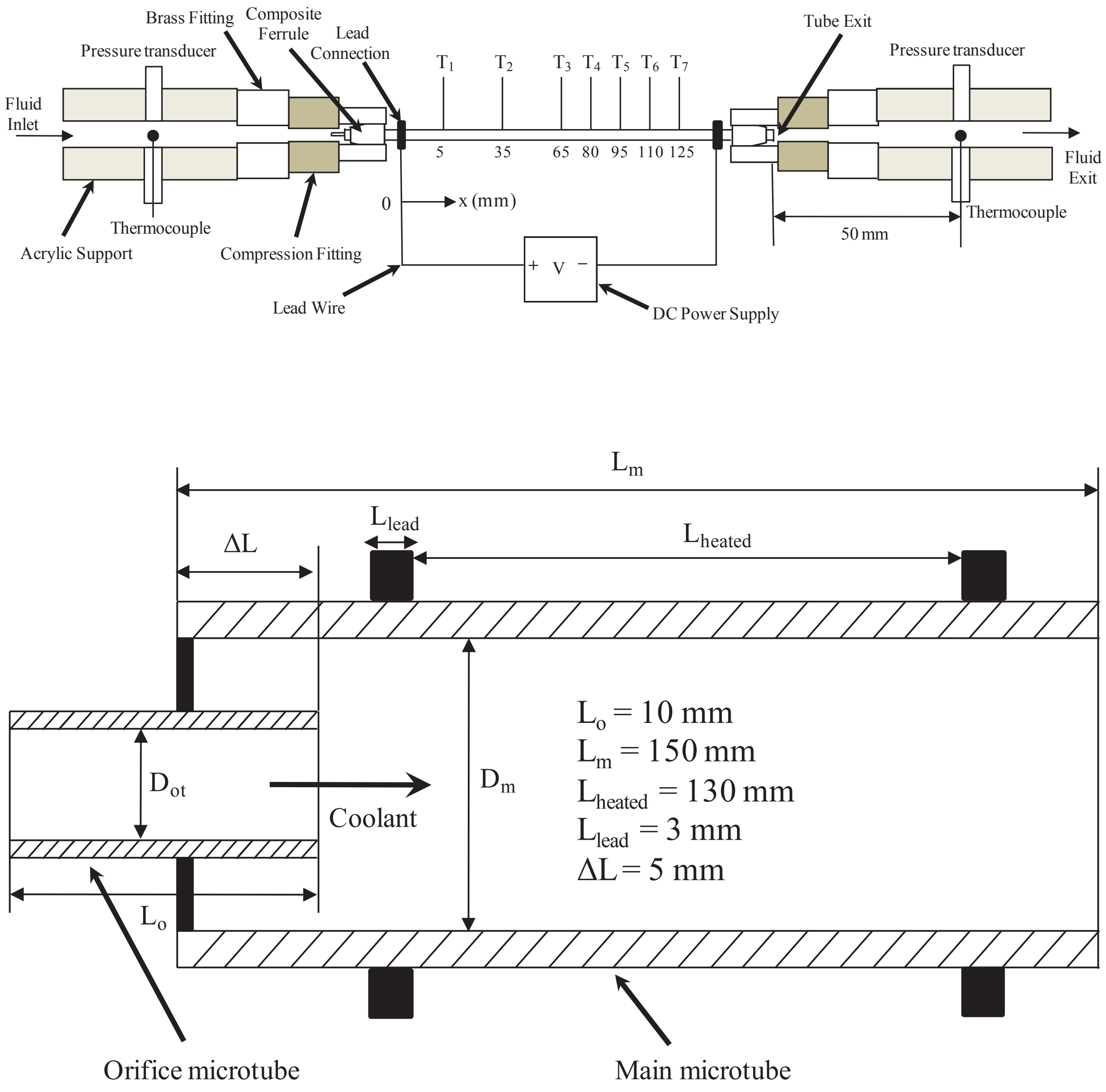

Figure 3.2: The schematic of present microtube package (not to scale).

are used to assemble the microtubes on the supports and prevent the channel from leakage. The wire lead is clipped on the microtube to ensure a closed electric circuit. A uniform heat flux is applied to the microtube by passing DC through the microtube wall. Seven T-type thermocouples with the junction diameter of 80 μm are attached at the outer wall of microtubes. The locations of thermocouples are shown in Figure 3.2.

3.3 Degassing

Due to the large solubility of air in FC-72 (approximately 50% by volume), degassing is a necessary process before proceeding with the experiment. The degassing procedure consists of the following major steps:

1. The water is preheated to 40 °C.
2. The electrical power is switched on to heat FC-72 in the tank.
3. The valve 1 is opened to connect the condenser with the FC-72 tank, and the cooling water is turned on.
4. Both pumps are turned on to circulate water and FC-72. The flow rate of FC-72 is set to 60 ml/min. Heat transfer between the hot water and the cold FC-72 occurs in the coil heat exchanger.
5. When the bulk boiling of FC-72 occurs in the heat exchanger, only vapor can be observed in the degassing branch and the temperature at the inlet of water pump is approximate 70°C. The power of heating the water is turned off to maintain the temperature at the inlet of water pump below 80°C (maximum working temperature of water pump). The facility is run about 30 minutes to allow all FC-72 to be boiled in

the heat exchanger. (Note: the volume of FC-72 in the tank and flow loop is approximate 1.5 L.)

6. The power to the heater in FC-72 tank and water pump are turned off. The facilities are run for 10 minutes to push the vapor in the heat exchanger back to the FC-72 tank.
7. Gear Pump 1 and the cooling water are turned off. All valves are closed. The facility is left for two hours to be cooled to the room temperature. The FC-72 vapor in the tank is condensed. The degassing is completed.

The quality of degassing is checked before the measurement. The mass flow rate is set to the tested value. FC-72 is heated in the microtube by electrical power until bubbles generate at the exit of test-section. If the outlet temperature is below the local saturation temperature, which is determined by outlet pressure, and the flow condition is very stable, it indicates the poor degassing. Thus, the degassing needs to be repeated. If the outlet temperature is approximately equal to the local saturation temperature, and the flow oscillation occurs, the degassing is considered to be completed well.

3.4 Validations of Experimental Measurement

3.4.1 Pressure Drop Measurement

The measurement of adiabatic single-phase liquid pressure drop in the microtube without orifice is carried out first to validate the facility. In the experiment, the hydraulic fittings are used to assemble the microtube on the support. The inner diameters of support, hydraulic fittings, and microtube are different, which cause the minor pressure losses due to the contraction and expansion. Besides, there is a certain distance between the measured location and the entrance of microtube, as shown in Figure 3.2. It is necessary to consider the frictional pressure drop in the support and hydraulic fittings. Since at the entrance of microtube is only subcooled liquid, the pressure loss coefficients of single-phase liquid by sudden contraction and expansion are obtained from Munson et al. (2009). The measured pressure drop in the experiment is written as,

$$\Delta P_{meas} = \Delta P_{loss} + \Delta P_{sp} \tag{3.1}$$

The total pressure loss between the measured location and the entrance/exit of microtube is calculated as,

$$\Delta P_{loss} = \Delta P_{in,loss} + \Delta P_{e,loss} = \frac{8\dot{m}^2}{\rho_{in}\pi^2} \sum_{i=1} \frac{1}{D_i^4} \left(K_i + f_i \frac{L_i}{D_i} \right) \tag{3.2}$$

where, K is the pressure loss coefficients. The pressure drop in the microtube can be obtained by subtracting the pressure loss from measured pressure drop. The Darcy friction factor is calculated as,

$$f = \frac{2\Delta P_{sp} D_h}{G^2 \, L} \rho_{in} \tag{3.3}$$

Figure 3.3 shows the friction factor at *Reynolds numbers* ranging from 220 to 7000, which correspond to the mass fluxes ranging from 160 to 3000 kg/m^2·s. This range covers laminar flow, transition flow and turbulent flow. The validation is completed by comparing the friction factor with the classical correlation and literatures. For laminar flow, the friction factor is calculated by,

$$f_L = \frac{64}{Re} \tag{3.4}$$

The correlation proposed by Blasius (1913) is used to calculate the friction factor for turbulent flow,

$$f_T = 0.3164 \times Re^{-0.25} \tag{3.5}$$

Results show good agreement with the correlation in the laminar flow regime, and the surface roughness does not have an effect on the pressure drop. The same conclusion has been obtained for minitubes and microtubes with various inner diameters (Rands et al., 2006, Ghajar et al., 2010, and Barlak et al., 2011). In the transition flow regime, the friction factor increases as *Reynolds number* increases. In the present work, the transition flow starts at a *Reynolds number* of 2000, which is earlier than what has been observed in previous works. A possible reason for this behavior might be the surface roughness, vibrations by the gear pump, or the overall assembly of the microtube package. In the turbulent regime, the friction factor obtained in the experiment is larger than one proposed by Blasius (1913), but it is worth noting that the friction factor in Blasius's correlation corresponds to a hydraulically smooth tube. The surface roughness has been identified as a critical parameter for the pressure drop of internal flow, especially in a micro-scale tube as reported by Qi et al. (2007b). The deviation between the current experimental data and the correlation is within 15%. Some data from previous literatures with similar hydraulic diameters have also been selected for the comparison. The same trend of friction factor against *Reynolds number* is observed.

3.4.2 Temperature Measurement

The temperature data at the outer wall are acquired by thermocouples. Data reduction is carried out to obtain the heat transfer coefficient. It is necessary to estimate the heat loss since the microtube is directly exposed to the atmosphere. For determining the heat loss, the microtube is emptied and the electrical power is applied on the microtube. The temperature data of the outer wall is recorded. The heat generated by the electricity is only transferred to the surrounding air. The heat loss at different locations can be expressed using second order polynomial curving fitting,

$$q'_{loss,i} = \frac{V \cdot I}{L_{heated}} = a_i \left(T_i - T_{i,ref}\right)^2 + b_i \left(T_i - T_{i,ref}\right) + c_{\mathrm{i}} \tag{3.6}$$

$T_{i,ref}$ is the reference value which is measured without applying the electrical power. The averaged total heat loss is calculated as,

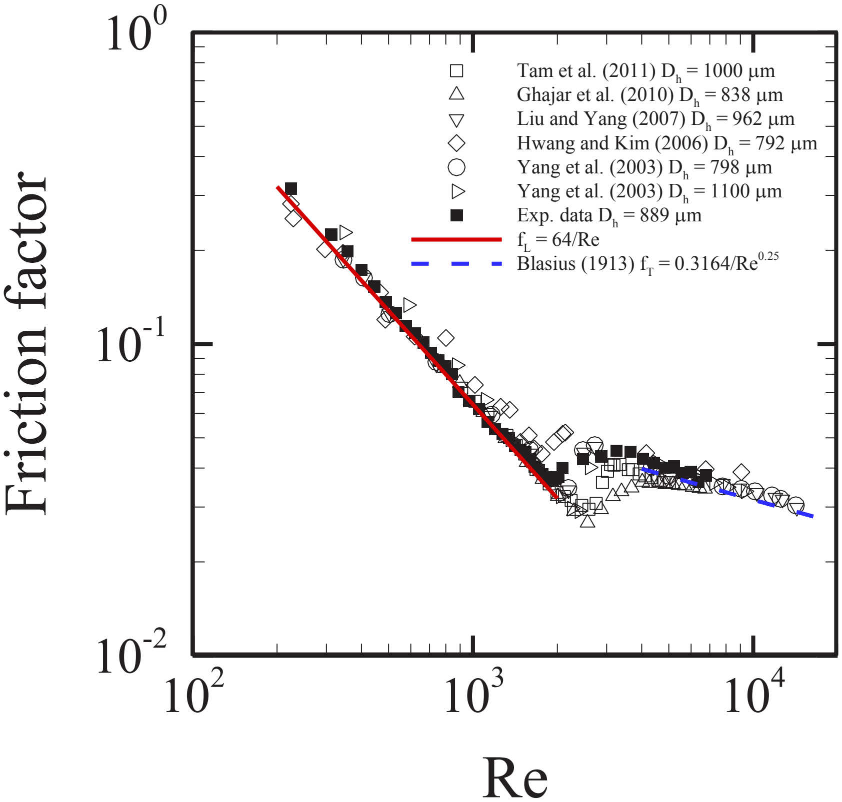

Figure 3.3: Comparison of single-phase liquid friction factor in the microtube with an inner diameter of 889 μm at 220 < *Re* < 7000.

$$Q_{loss} = q'_{loss,ave} L_{heated} = \left(\frac{1}{5} \sum_{i=1}^{5} q'_{loss,i} \right) L_{heated} \tag{3.7}$$

The effect of axial heat conduction in the wall is evaluated using the dimensionless parameter called *axial conduction number* proposed by Maranzana et al. (2004),

$$M = \frac{q''_{cond}}{q''_{conv}} = \frac{k_{tube} \delta_{tube}}{\rho_l C_p \delta_l L u} \tag{3.8}$$

The axial heat conduction is negligible as *axial conduction number* is lower than 0.01. In the current experiment, the maximum *axial conduction number* is 2.5×10^{-4}. Hence, the axial heat conduction in the wall is neglected and the inner wall temperature is derived by one dimensional steady state heat conduction in radial direction,

$$\frac{1}{r} \frac{\partial}{\partial r} \left(r \frac{\partial T}{\partial r} \right) + \frac{\dot{e}}{k_{tube}} = 0 \tag{3.9}$$

The electrical generation is calculated as,

$$\dot{e} = \frac{4V \cdot I}{\pi \left(D_{outer}^2 - D_{inner}^2 \right) L_{heated}} \tag{3.10}$$

After applying the thermal boundary conditions,

$$T_{w,i} = T \big|_{r = r_{outer}} \tag{3.11}$$

$$q''_{loss,ave} = -k_{tube} \frac{\partial T}{\partial r} \bigg|_{r = r_{outer}} \tag{3.12}$$

The inner wall temperature can be obtained,

$$T_{w,inner} = T_{w,outer} + \frac{\dot{e}\left(D^2_{outer} - D^2_{inner}\right)}{16k_{tube}} + \left(\frac{\dot{e}D^2_{outer}}{8k_{tube}} - \frac{q''_{loss,ave}}{2k_{tube}}D_{outer}\right) ln\left(\frac{D_{inner}}{D_{outer}}\right) \tag{3.13}$$

The fluid temperature is calculated based on thermodynamics,

$$C_{p@T_{f,i}} T_{f,i} = C_{p@T_{f,in}} T_{f,in} + \frac{x_i\left(V \cdot I - Q_{loss}\right)}{\dot{m}L_{heated}} \tag{3.14}$$

The local fluid temperature can be obtained using Equation 3.14 since the thermal capacity is a function of fluid temperature. As soon as the inner wall temperature and fluid temperature are known, the local heat transfer coefficient is calculated as,

$$h_i = \frac{q''}{T_{w,inner,i} - T_{f,i}} \quad \text{if } T_{f,i} < T_{sat,i} \text{ (single-phase heat transfer)} \tag{3.15}$$

$$h_i = \frac{q''}{T_{w,inner,i} - T_{sat,i}} \quad \text{if } T_{f,i} \geq T_{sat,i} \text{ (Two-phase heat transfer)} \tag{3.16}$$

The uniform heat flux at the inner wall is calculated as,

$$q'' = \frac{V \cdot I - Q_{loss}}{\pi D_{inner} L_{heated}} \tag{3.17}$$

As soon as the flow boiling occurs, the local vapor quality can be calculated as,

$$\chi_i = \frac{H_i - H_{l,sat}}{h_{fg}} \tag{3.18}$$

The measurement of single-phase liquid heat transfer is carried out for the validation of test facility. The *Nusselt number* in laminar flow obtained from experiment is compared with the correlation proposed by Grigull and Tratz (1965),

$$Nu_L = 4.364 + 8.68 \times \left(1000x^*\right)^{-0.506} exp\left(-41x^*\right) \tag{3.19}$$

where, $x^* = x/\left(D_h\ Re\, Pr\right)$

and the *Nusselt number* in transition flow and turbulent flow is compared with the correlation proposed by Gnielinski (1976),

$$Nu_T = \frac{\left(f_T/8\right)\left(Re-1000\right)Pr}{1+12.7\left(f_T/8\right)^{1/2}\left(Pr^{2/3}-1\right)} \tag{3.20}$$

The friction factor of turbulent flow in Equation 3.20 is calculated using the correlation proposed by Filonenko (1954),

$$f_T = \left[1.82 \times log\left(Re\right) - 1.64\right]^{-2} \tag{3.21}$$

The *Reynolds number* and *Prandtl number* are calculated based on the local properties of the working fluid. Figure 3.4a shows the *Nusselt number* variation along the flowing direction. It is noted that the *Nusselt number* in the experiment is lower than the correlation at $x^* < 0.001$. A similar phenomenon was also observed by Warrier et al. (2002) and Muwanga and Hassan (2006). However, the experimental results show good agreement with the correlation at $x^* > 0.001$. The *Nusselt number* tends to be 4.36. In transition flow and turbulent flow, the derivation of comparison between the experiment and correlation is within 30%, as shown in Figure 3.4b. The comparisons in laminar flow and turbulent flow indicate that the temperature measurement is valid for the future experiment.

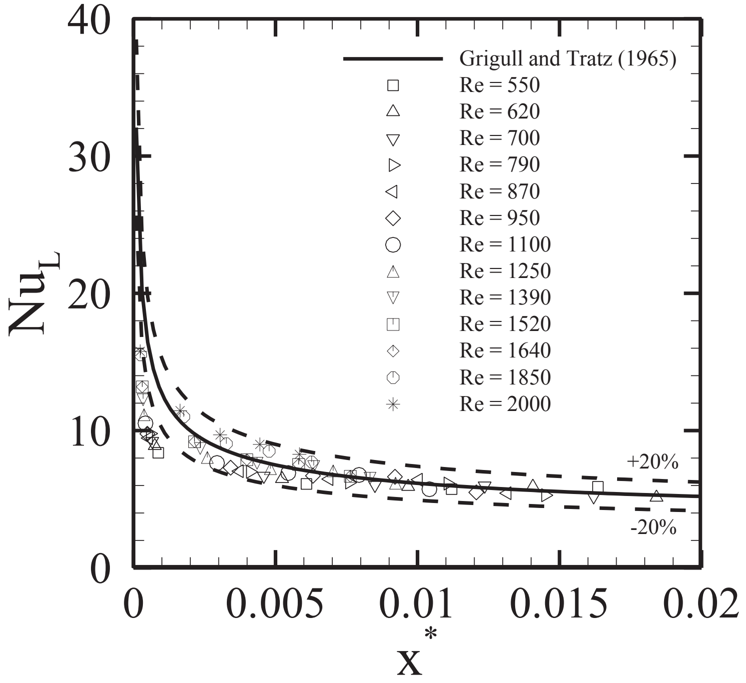

(a)

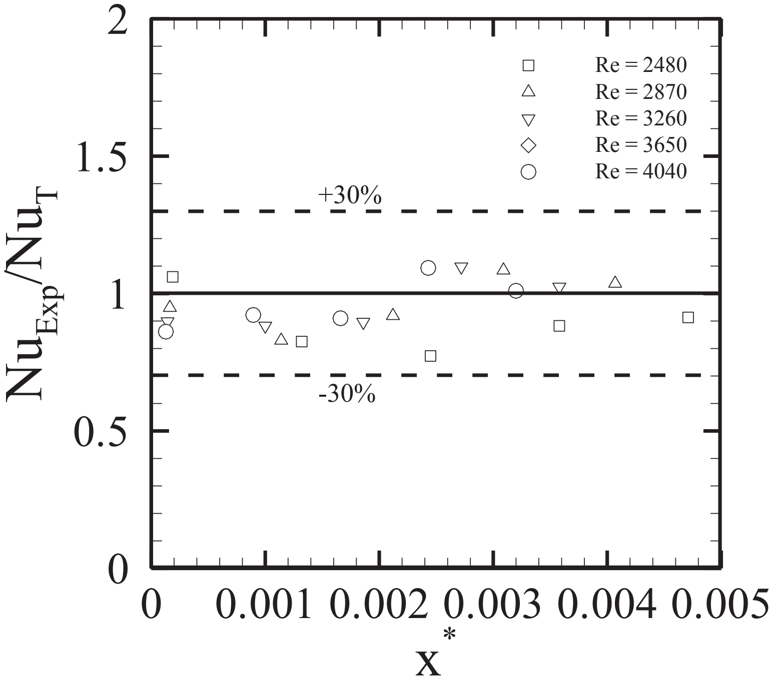

(b)

Figure 3.4: The validation of heat transfer measurement in the microtube with an inner diameter of 889 μm.

3.5 Uncertainty

The uncertainty of each parameter is listed in Table 3.2. Three flow rotameters are used to measure the volume rate; their uncertainties are 5% Full Scale. The T-type thermocouple and the pressure transducer have uncertainties of 0.5°C and 0.05% Full Scale, respectively. The Equations 3.22-3.27 are used to calculate the uncertainties of pressure drop, heat flux, mass flux, heat transfer coefficient, and area ratio using the method proposed by Moffat (1988).

$$\varepsilon_{\Delta P} = \sqrt{\varepsilon_{P_{in}}^2 + \varepsilon_{P_{out}}^2} \tag{3.22}$$

$$\varepsilon_{q''} = \sqrt{\left(\varepsilon_V \frac{\partial q''}{\partial V}\right)^2 + \left(\varepsilon_I \frac{\partial q''}{\partial I}\right)^2 + \left(\varepsilon_A \frac{\partial q''}{\partial A}\right)^2} \tag{3.23}$$

$$\varepsilon_G = \sqrt{\left(\varepsilon_T \frac{\partial G}{\partial T}\right)^2 + \left(\varepsilon_Q \frac{\partial G}{\partial Q}\right)^2 + \left(\varepsilon_{D_{inner}} \frac{\partial G}{\partial D_{inner}}\right)^2} \tag{3.24}$$

$$\varepsilon_{\Delta T} = \sqrt{\varepsilon_{T_{w,inner}}^2 + \varepsilon_{T_f}^2} \tag{3.25}$$

$$\varepsilon_h = \sqrt{\left(\varepsilon_{\Delta T} \frac{\partial h}{\partial (\Delta T)}\right)^2 + \left(\varepsilon_{q''} \frac{\partial h}{\partial q''}\right)^2} \tag{3.26}$$

$$\varepsilon_{AR} = \sqrt{\left(\varepsilon_{D_{ot}} \frac{\partial AR}{\partial D_{ot}}\right)^2 + \left(\varepsilon_{D_m} \frac{\partial AR}{\partial D_m}\right)^2} \tag{3.27}$$

Table 3.2: Uncertainty

Parameters	**Uncertainty**
T-type Temperatures, T	± 0.5 ºC
Volumetric flow rate, Q, Rotameter1	± 8.52 ml/min
Volumetric flow rate, Q, Rotameter2	± 1.65 ml/min
Volumetric flow rate, Q, Rotameter3	± 0.97 ml/min
Inlet pressure transducer, P_{in}	± 0.259 kPa
Outlet pressure transducer, P_{out}	± 0.173 kPa
Voltage, V	± 0.05 V
Current, I	± 0.05 A
Calculated Parameters	
Microtube pressure drop, ΔP	± 0.31 kPa
Heat flux, q''	± 0.4 - 5.6 kW/m^2
Mass flux, G, Rotameter1	± 0.345 kg/m^2·s
Mass flux, G, Rotameter2	± 0.07 kg/m^2·s
Mass flux, G, Rotameter3	± 0.04 kg/m^2·s
Temperature difference, ΔT	± 0.7 ºC
Heat transfer coefficient, h	± 3.8% - 17.5%

Chapter 4

4 Experiments on Flow Boiling Heat Transfer

The inlet orifice has been validated to be an effective method to stabilize the flow in multiple microchannels. However, the performance of inlet orifice in single microtube has not been studied yet. The fundamental research is still lack. This chapter is to investigate the effect of inlet orifice on flow boiling heat transfer in single horizontal microtube. Two different area ratios, 50% and 20%, are tested. The two-phase pressure drop, critical heat flux and flow boiling heat transfer coefficient in the microtube with and without inlet orifices are obtained and compared with the existing correlations.

4.1 Test Matrix

The test-section has been introduced in Section 3.2. Table 4.1 lists the test matrix in the measurement of flow boiling heat transfer in single microtube with and without orifices.

Table 4.1: Test Matrix

Parameter	Nominal value
Heat flux, q''	6 - 170 kW/m^2
Mass flux, G	160 - 870 kg/m^2·s
Area ratio, AR	50%, 20%
Inlet temperature, T_{in}	23, 35 °C
Saturation pressure, P_{sat}	10, 45 kPa

Two area ratios are selected to study the effects of inlet orifice on two-phase pressure drop, critical heat flux, and flow boiling heat transfer coefficient at two inlet temperatures and saturation pressures.

4.2 Two-Phase Pressure Drop

4.2.1 Effect of Inlet Orifice

It is commonly considered that addition of inlet orifice increases the pressure drop. However, it is necessary to study how significantly the inlet orifice increases two-phase pressure drop in single microtube. Figure 4.1 shows the ratio of two-phase pressure drop in microtubes with and without orifices at P_{sat} = 10 kPa. The vapor quality, χ_7 corresponds to the location of x = 125 mm, as shown in Figure 3.2. At G = 160 kg/m^2·s, the pressure drop in microtubes with orifices is more than 30% higher than one in the microtube without orifice. The ratio of two-phase pressure drop decreases as vapor quality increases. The same trend is also observed at G = 550 kg/m^2·s. As mass flux increases to 550 kg/m^2·s, the ratio of two-phase pressure drop falls within 30% at χ_7 >

0.2. The above phenomena are due to the reduced percentage of pressure drop by orifice in the total pressure drop as the mass flux or vapor quality increases. Two major components in the total pressure drop are the pressure drop by inlet orifice and two-phase pressure drop in the main microtube. The experimental results indicate that, at low mass fluxes or vapor quality, the orifice has a significant effect on the total pressure drop. As the mass flux or vapor quality increases, the two-phase pressure drop in the main microtube takes the dominant portion in the total pressure drop, resulting in a reduced difference of total pressure drop between the microtubes with and without orifice. Therefore, at high mass fluxes or vapor qualities, the orifice shows a slight effect on the total pressure drop.

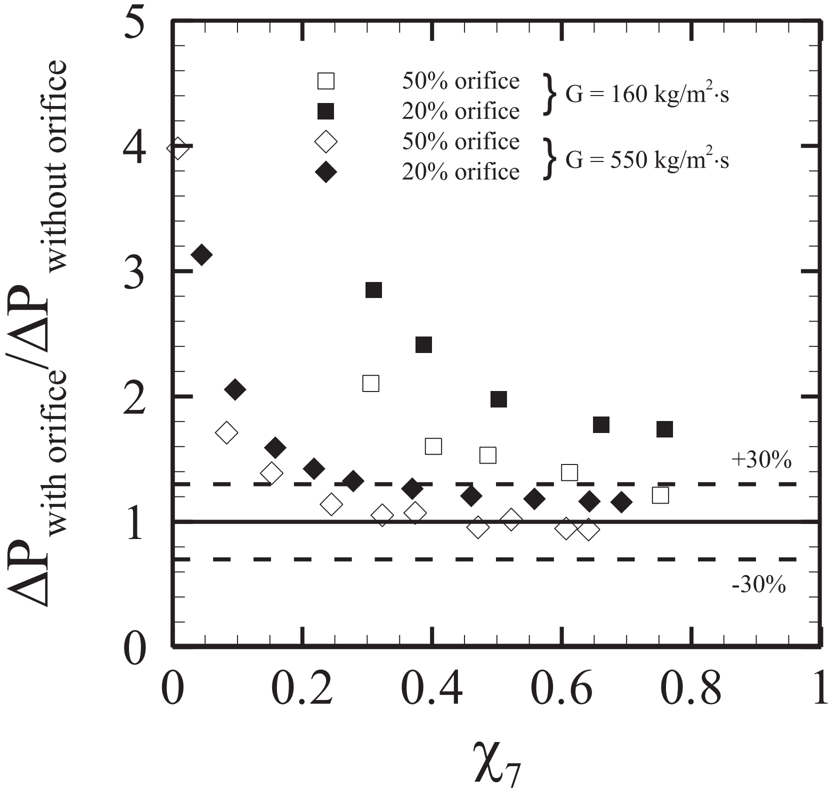

Figure 4.1: Comparisons of two-phase pressure drop in the microtubes with and without orifice at G = 160 and 550 kg/m^2·s (χ_7 is the vapor quality at T_7).

4.2.2 Effect of Saturation Pressure

Figure 4.2 shows the comparison of two-phase pressure drop in the microtube with 20% orifice at two saturation pressures. At $\chi_7 < 0.3$, the two-phase pressure drop seems independent of saturation pressure. However, at $\chi_7 > 0.3$, the two-phase pressure drop decreases as saturation pressure increases. It is considered that, at low vapor quality, the accelerational component is dominant, which is determined by the vapor quality. As vapor quality increases, the frictional component plays a dominant role in two-phase pressure drop. Hence, the pressure drop at high vapor quality is mainly dependent on the viscosity. The viscosity decreases as the saturation pressure increases, as shown in Table 4.2, which leads to the lower pressure drop at higher saturation pressure and vapor quality.

Table 4.2: FC-72 properties at two saturation pressures

P	T_{sat}	C_p	h_{fg}	k	μ	Pr	ρ_l/ρ_v	σ
kPa	°C	J/kg·°C	J/kg	W/m·°C	Pa·s	NA	NA	N/m
10	60.00	1103.66	83535.7	5.18E-2	4.39E-4	9.36	109.08	0.80E-2
45	67.98	1115.99	81158.7	5.08E-2	4.06E-4	8.92	83.47	0.73E-2

4.3 Critical Heat Flux

The effect of the orifice on the critical heat flux at mass flux ranging from 160 to 870 kg/m^2·s is studied. Figure 4.3 shows the typical boiling curve in the microtube without orifice at G = 420 kg/m^2·s. The wall temperature increases almost linearly as heat flux increases in single-phase flow regime. As soon as the flow boiling occurs, the wall temperature suddenly drops to a value close to the saturated temperature. In two-phase

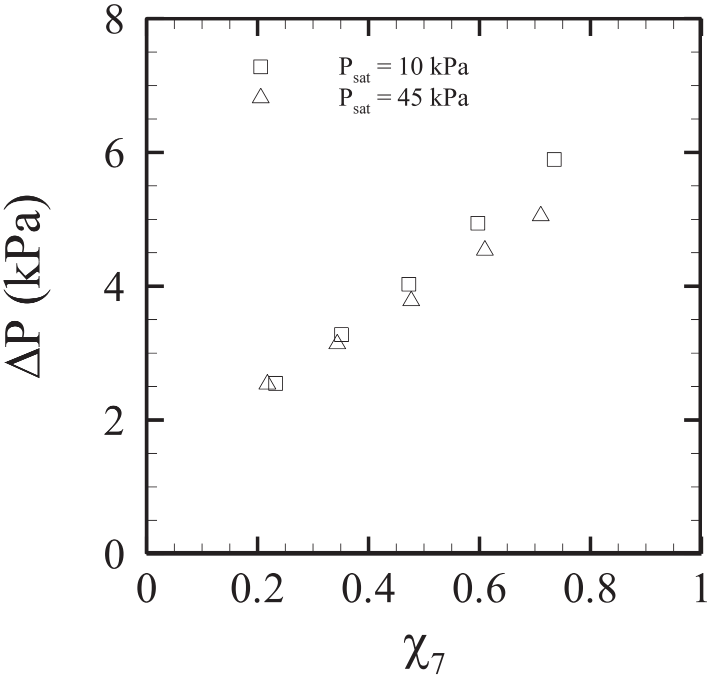

(a)

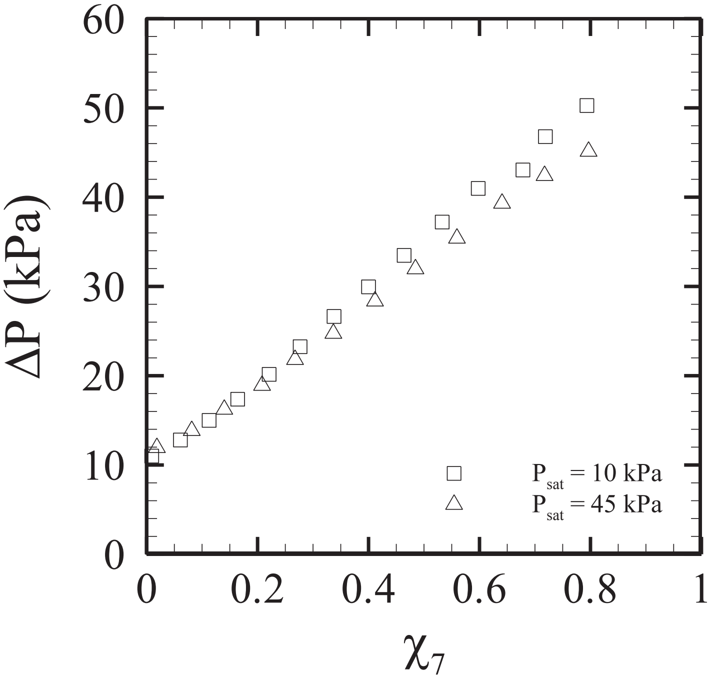

(b)

Figure 4.2: Effect of saturation pressure on two-phase pressure drop in the microtube with 20% orifice. (a) $G = 160$ kg/m^2·s; (b) $G = 550$ kg/m^2·s.

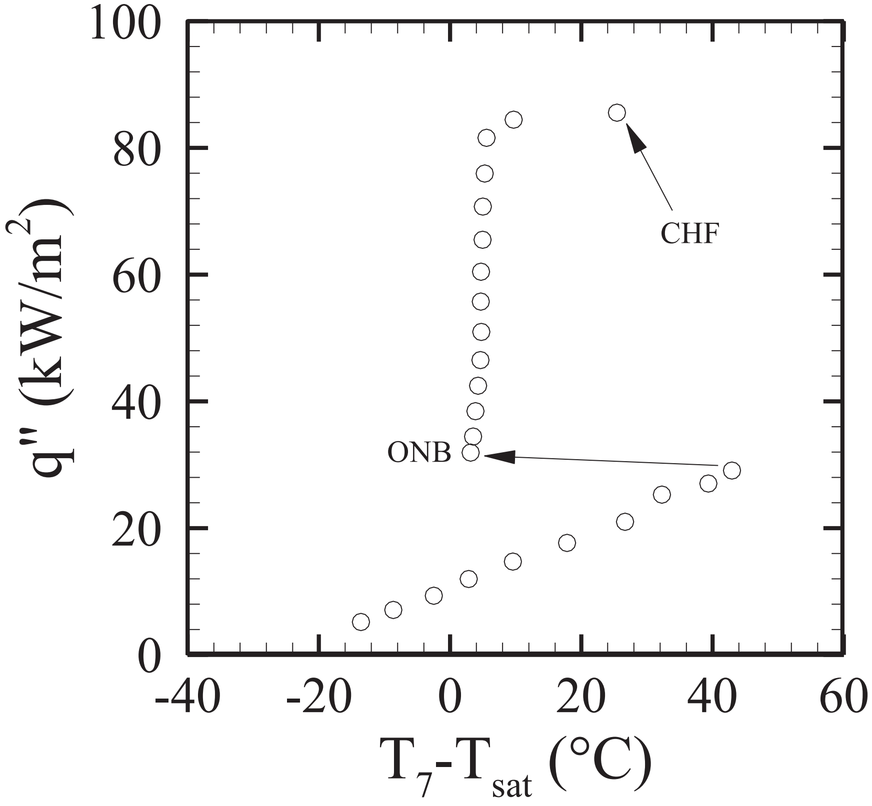

Figure 4.3: The typical boiling curve in the microtube without orifice at G = 420 kg/m^2·s, T_{in} = 23 °C and P_{sat} = 10 kPa.

flow regime, the wall temperature increases slightly with increasing heat flux. The slope of superheated temperature to the heat flux in two-phase flow is much larger than one in single-phase flow. As the heat flux increases to a certain value, the wall is superheated to an extremely high degree. A small increment of heat flux results in a large jump of wall temperature. In this work, the heat flux is considered as critical heat flux, q''_{CHF} ,when the wall temperature is 20°C higher than the fluid saturated temperature, which is approximately equal to thermal critical temperature of semiconductive device, 85°C.

In the present experiment, only saturated critical heat flux (CHF) is measured. Seven correlations to predict the saturated CHF in both single microchannel and parallel microchannels are selected to compare with the experimental data obtained in the microtube without orifice. These correlations were developed under uniform heating condition and contain some of following parameters: the density ratio (ρ_l/ρ_v), ratio of heated length to hydraulic diameter (L_{heated}/D), mass flux (G), *Weber number*, inlet condition (χ_{in} *or* H_{in}), and exit vapor quality (χ_e). The summary of selected correlations is listed in Table 4.3. Figure 4.4 shows the comparison of critical heat flux between the experimental data and correlations at the mass fluxes ranging from 160 to 550 $\mathrm{kg/m^2{\cdot}s}$. Bowers and Mudawar (1994) and Qu and Mudawar (2004) developed the correlations in parallel microchannels. Their correlations over predict the critical heat flux in current experiment. As mentioned by Qu and Mudawar (2004), the correlations for the multiple microchannels are not suitable for the single microchannel due to the vapor back flow to the inlet plenum and the feature of parallel microchannels. Wojtan et al. (2006) and Qi et al. (2007a) developed their correlations in single microchannel based on their experimental data which are not sufficient for general correlation development. Wu et al. (2011) collected 629 data points to correlate the saturated CHF using the exit vapor quality. It also over predicts the critical heat flux. Zhang et al. (2006) developed their correlation by collecting 2539 saturated CHF data points using inlet condition. The comparison shows that the correlations developed by Basu et al. (2011) and Zhang et al. (2006) can predict the critical heat flux well. The correlation proposed by Zhang et al. (2006) shows the best agreement with current experimental data since their correlation was developed based on the sufficient data points and using inlet condition as recommended by Hall and Mudawar (2000). The derivation of Zhang et al.'s correlation from the experiment is within 15%.

Table 4.3: The selected correlations for predicting the saturated critical heat flux

Reference	Correlation of saturated CHF	Notes
Bowers and Mudawar (1994)	$Bo_{CHF} = 0.16 We^{-0.19} \times \left(\frac{L_{heated}}{D_h}\right)^{-0.54}$	Microchannel arrays; Developed based on their data; Water; D_h = 510 µm; L_{heated} = 10 mm; G = 120-480 kg/m^2·s; P_{in} = 1.38 bar; ΔT_{sub} = 10-32 ^{o}C; $q'' < 260$ W/cm^2
Qu and Mudawar (2004)	$Bo_{CHF} = 33.43 \left(\frac{\rho_v}{\rho_l}\right)^{1.11} \times \left(\frac{1}{We}\right)^{0.21} \times \left(\frac{L_{heated}}{D_h}\right)^{-0.36}$	Microchannel arrays; Water and R113; D_h = 340 µm; L_{heated} = 44.8 mm; G = 86-368 kg/m^2·s; P_{out} = 1.13 bar; T_{in} = 30 and 60 ^{o}C; $q'' < 220$ W/cm^2
Zhang et al. (2006)	$Bo_{CHF} = 0.0352 \times \left(\frac{L_{heated}}{D_h}\right)^{-0.311} \times \left[2.05\left(\frac{\rho_v}{\rho_l}\right)^{0.17} - \chi_{eq,in}\right]$ $\times \left[We + 0.0119\left(\frac{L_{heated}}{D_h}\right)^{2.31} \times \left(\frac{\rho_v}{\rho_l}\right)^{0.361}\right]^{-0.295}$	Single microtubes; Water; 2539 data points for saturated CHF; $330 \le D_h \le 6220$ µm; $1 \le L_{heated}/D_h \le 975$; G = 5.33-1.34 × 10^5 kg/m^2·s; P_{out} = 0.101-19 MPa; χ_{in} = -235 - 0; q'' = 9.35-27600 W/cm^2
Wojtan et al. (2006)	$Bo_{CHF} = 0.437 \left(\frac{\rho_v}{\rho_l}\right)^{0.073} \times \left(\frac{1}{We}\right)^{0.24} \times \left(\frac{L_{heated}}{D_h}\right)^{-0.72}$	Single microtube; R134a and R245fa; Developed based on their data; D_h = 500 and 800 µm; T_{sat} = -30 and 35 ^{o}C; L_{heated} = 20, 30, 50, 70 mm; G = 400-1600 kg/m^2·s; q'' = 0.32-60 W/cm^2
Qi et al. (2007a)	$Bo_{CHF} = (0.214 + 0.14 Co) \times \left(\frac{\rho_v}{\rho_l}\right)^{0.133} \times \left(\frac{1}{We}\right)^{0.333}$ $\times \frac{1}{1 + 0.03 L_{heated}/D_h}$	Single microtube; Nitrogen; Developed based on their data; D_h = 531, 834, 1042, 1931 µm; L_{heated} = 250 mm; G = 500-3000 kg/m^2·s; q'' = 7-25 W/cm^2
Basu et al. (2011)	$Bo_{CHF} = 0.3784 \left(\frac{\rho_v}{\rho_l}\right)^{0.051} \times \left(\frac{L_{heated}}{D_h}\right)^{-1.03} \times \chi_e^{0.8}$	Singe horizontal microtube; R134a; Developed based on their data; 113 data points; D_h = 500, 960, 1600 µm; L_{heated} = 120, 127, 128 mm; G = 300-1500 kg/m^2·s; $q'' < 27$ W/cm^2; ΔT_{sub} = 5-40 ^{o}C; P_{sat} = 490-1160 kPa;

Table. 4.3 (*continued*)

Wu et al. (2011)	$Bo_{CHF} = 0.6\left(\frac{L_{heated}}{D_h}\right)^{-1.19} \times \chi_e^{0.817}$	Weber number excluded; 629 data points; Micro/minichannels; Various working fluids $200 \leq D_h \leq 3000$ µm; $L_{heated} / D_h \leq 500$ G = 23.4-3000 kg/m^2·s; P_{sat} = 10-2300 kPa; χ_e = 0-1

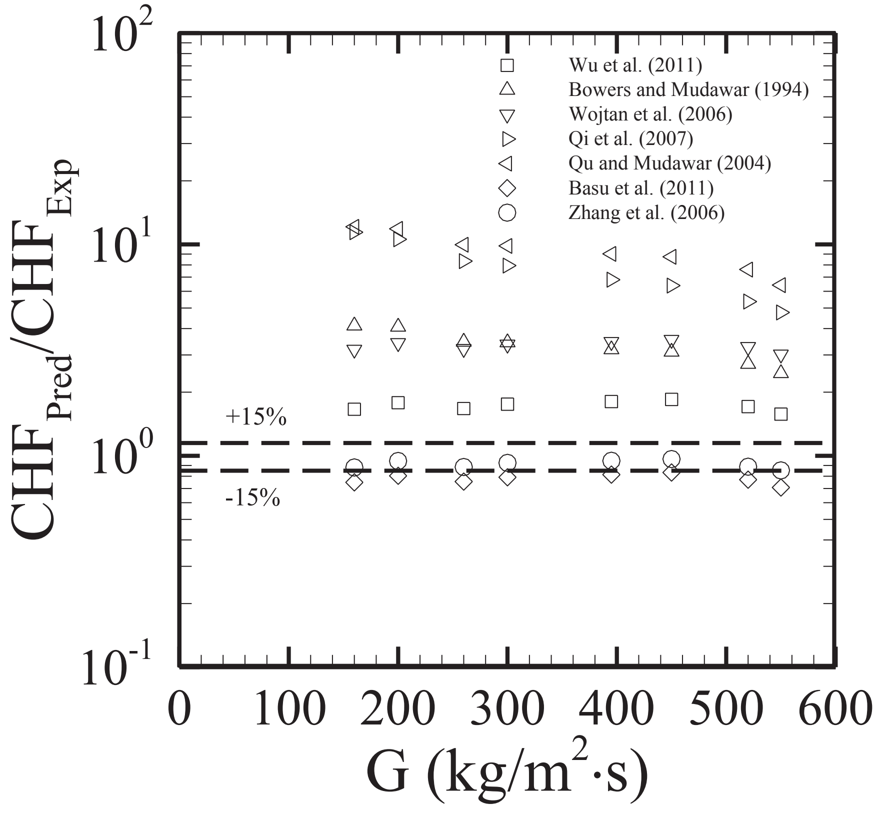

Figure 4.4: Comparisons of saturated CHF between experiment and correlations at $160 \leq G \leq 550$ kg/m^2·s, P_{sat} = 10 kPa and T_{in} = 23 °C.

Figure 4.5 shows the critical heat flux at different mass fluxes in the microtubes with and without orifices at P_{sat} = 10 kPa and T_{in} = 23 °C. The critical heat flux is classified into normal CHF and premature CHF. Normal CHF is measured at the stable flow operating condition while the premature CHF is usually accompanied with flow oscillation. Therefore, normal CHF and premature CHF can be distinguished by the flow condition in the experiment. Premature CHF usually has a lower value than the normal CHF since the flow stays longer in the microtube and absorbs more energy if the flow oscillation occurs in the microtube. More liquid evaporates and dry-out occurs at lower heat flux under unstable condition than stable condition. At $G < 550$ kg/m^2·s, the stable flow condition is observed in the microtubes with and without orifices. The flow

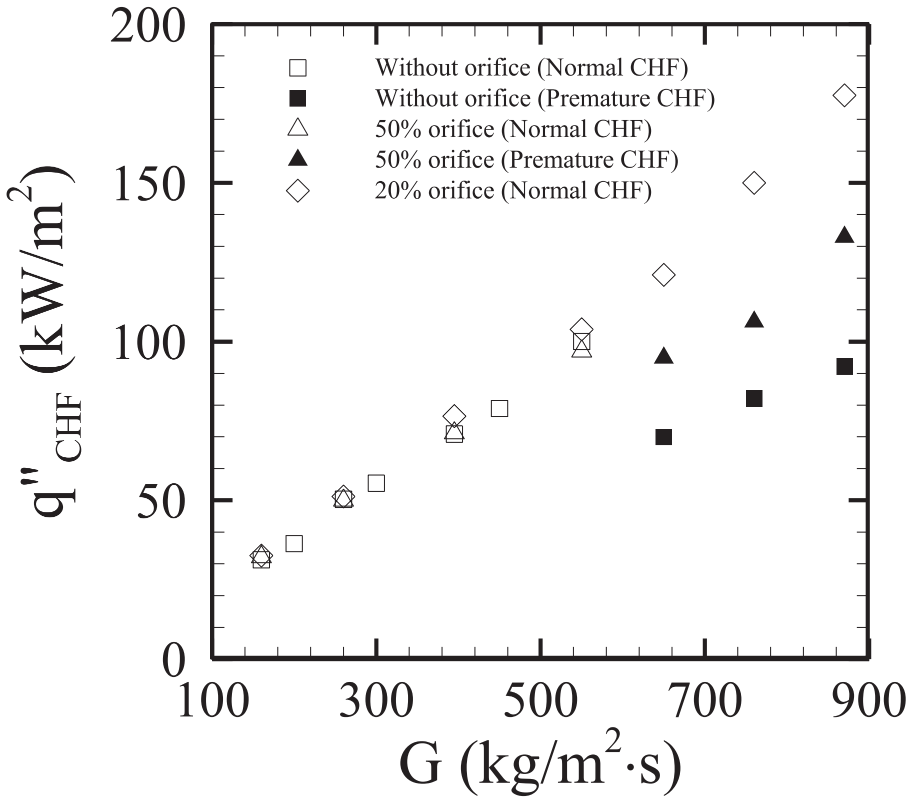

Figure 4.5: Comparison of saturated CHF in the microtubes with and without orifice.

oscillation is eliminated by the upstream throttling valve and/or orifice. The measured CHF is considered as normal CHF. The orifice doesn't enhance the critical heat flux in single horizontal microtube at $G \leq 550$ kg/m^2·s, as shown in Figure 4.5. However, Park et al. (2009) proposed that the orifice was able to increase the CHF in parallel multiple microchannels. It could be explained that, in their work, the throttling valve was assembled upstream of inlet plenum instead of the entrance of each microchannel. The throttling valve was not able to block the vapor back flow towards the inlet plenum in the heat sink without orifice. Therefore, the flow instability cannot be eliminated completely only by the throttling valve, which led to the early occurrence of CHF (premature CHF). However, the addition of the orifice placed at the entrance of each channel effectively prevented reversed flow. The measured CHF was normal CHF which is larger than the premature CHF at the same mass flux. The same phenomenon was observed by Lee and Mudawar (2009). In this work, there is no inlet plenum in the single microtube measurement. The function of orifice is same as the upstream throttling valve. The flow is stabilized by the throttling valve or the combination of throttling valve and orifice. Since the microtube is very long (L/D = 170), the jet flow from the orifice cannot affect the flow pattern downstream close to the exit. Therefore, the orifice is not capable of normal CHF enhancement in single microtube at $G \leq 550$ kg/m^2·s.

The premature CHF is observed in the microtubes with 50% orifice and without orifice at $G > 550$ kg/m^2·s. At $G > 550$ kg/m^2·s, the system cannot be stabilized by throttling valve in the microtubes with 50% orifice and without orifice. However, the system remains stable at all tested mass fluxes in the microtube with 20% orifice. Therefore, the measured CHF in the microtube with 20% orifice is normal CHF and shows higher values than the other two at $G > 550$ kg/m^2·s. In addition, the premature CHF in 50% orifice microtube is larger than one in the microtube without orifice. It indicates that the addition of the orifice cannot increase the normal CHF in single microtube but increase premature CHF. Moreover, the small orifice can avoid or delay the premature CHF due to the improved flow stability.

Figure 4.6 shows the comparisons of critical heat flux at different saturation pressures and inlet temperatures. Increasing saturation pressure reduces the density ratio, which contributes to the enhancement of CHF. However, the decreased surface tension and enthalpy of vaporization by increasing saturation pressure tend to reduce CHF. Hence, the effect of saturation pressure on critical heat flux is determined by the superimposed result of all factors. In this measurement, the critical heat flux slightly increases by increasing the saturation pressure. For a fixed mass flux, CHF is increased by decreasing the inlet temperature due to the higher subcooling or smaller equilibrium subcooled vapor quality at the inlet. Also, CHF increases as mass flux increases at all operating conditions. Changing inlet temperature and saturation pressure cannot make inlet orifice contribute to the critical heat flux, as shown in Figure 4.7.

4.4 Heat Transfer Coefficient

4.4.1 Single-Phase Heat Transfer

Figure 4.8 shows the single-phase heat transfer coefficients of first three measured locations in three microtubes. At $G = 160$ kg/m^2·s, the orifice does not affect the heat transfer at $x = 5$ mm. It indicates that the recirculation flow generated by diverging

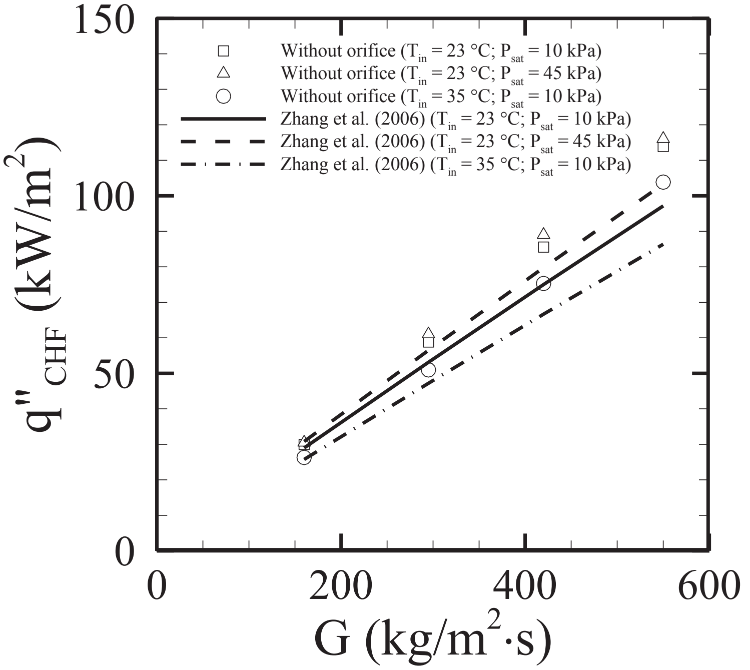

Figure 4.6: Comparisons of critical heat flux in the microtubes without orifice at different saturation pressures and inlet temperatures.

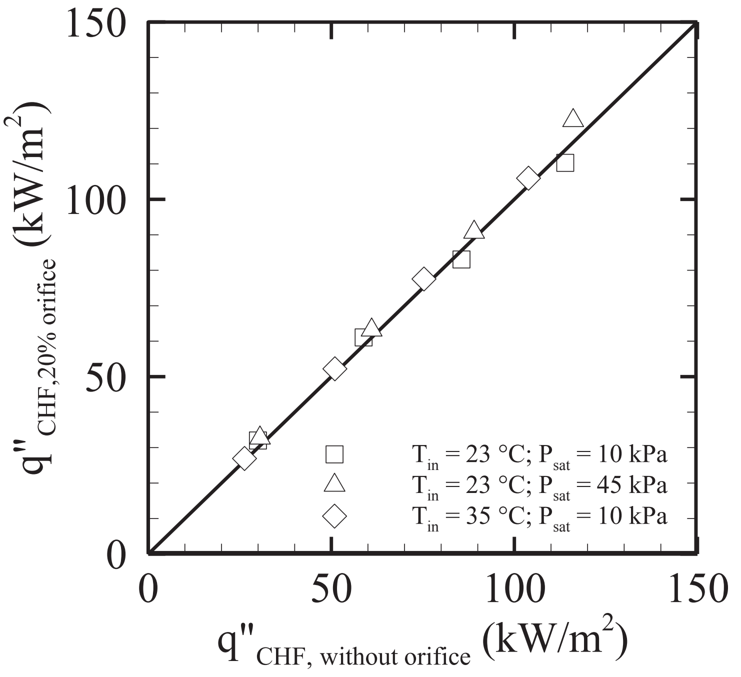

Figure 4.7: Comparisons of critical heat flux in the microtubes without orifice and with 20% orifice at different operating conditions.

structure does not spread to the location of x = 5 mm at G = 160 kg/m^2·s. As the mass flux increases to 260 kg/m^2·s, the heat transfer is slightly enhanced by the inlet orifice with 20% area ratio since the secondary flow extends downstream, which increases the local velocity. However, the heat transfer coefficient in the microtube with 50% orifice is almost same as one in the microtube without orifice. The same result is obtained at G = 395 kg/m^2·s, but the 20% orifice increases the heat transfer dramatically. As mass flux keeps increasing, the 50% orifice also enhances the local heat transfer. The heat transfer coefficient increases as mass flux increases due to the strengthened recirculation flow. A slight enhancement on heat transfer coefficient by 20% orifice is observed at x = 35 mm. At x = 65 mm, the heat transfer coefficient has no difference at tested mass fluxes. The flow becomes fully unidirectional. Orifice no longer influences the heat transfer.

4.4.2 Flow Boiling Heat Transfer

Flow boiling heat transfer measurements are carried out at mass fluxes ranging from 160 to 550 kg/m^2·s. Figure 4.9 shows the saturated flow boiling heat transfer coefficient at the location of x = 125 mm in the microtube without orifice. The saturation pressure is 10 kPa. At G = 160 kg/m^2·s, the heat transfer coefficient decreases as vapor quality increases. It is considered that, at low mass fluxes, the drag force on the bubble is weak. The departure diameter of bubble is so large that it fills the channel before departure. The corresponding flow regime is annular flow. It suppresses the bubble nucleation. In the meantime, the forced convective boiling cannot enhance the heat transfer due to the low liquid film velocity. Saitoh et al. (2005) obtained the same trend of heat transfer coefficient with vapor quality in the microtube with a diameter of 0.51 mm. At G > 160

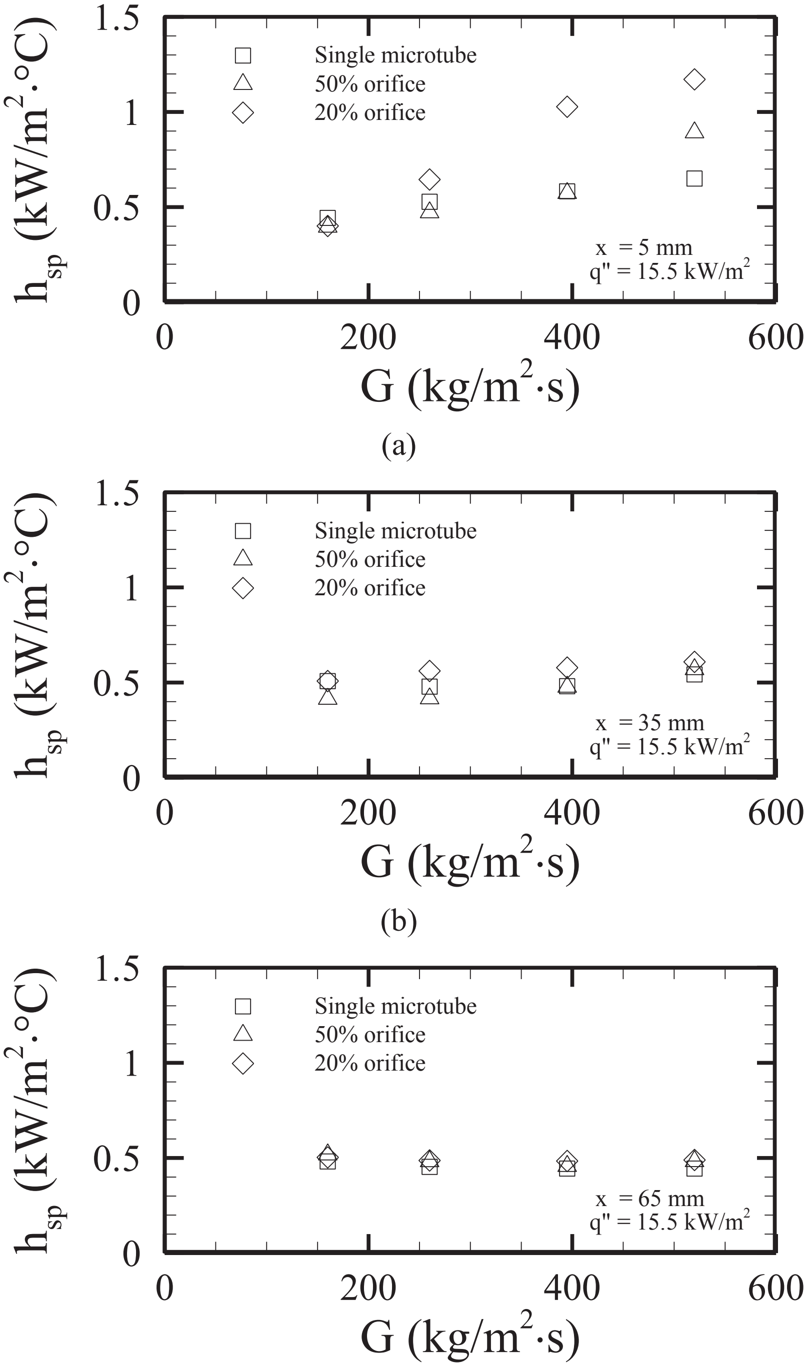

(a)

(b)

(c)

Figure 4.8: Comparisons of single-phase heat transfer coefficients at three locations in three microtubes.

kg/m^2·s, the heat transfer coefficient decreases slightly at $\chi_7 < 0.1$, and increases as vapor quality increases. Besides, the heat transfer coefficient is independent of the mass flux at $\chi_7 < 0.2$ and increases as mass flux increases at $\chi_7 > 0.2$. It is considered that the dominant boiling mechanism transits from nucleate boiling to forced convective boiling. At $\chi_7 < 0.1$, the nucleate boiling is dominant. The decreasing heat transfer coefficient with the increase of vapor quality is caused by the suppression of bubble nucleation. At $\chi_7 > 0.1$, the forced convective boiling becomes dominant. The heat transfer coefficient starts to increase as vapor quality increases. Also, it becomes dependent on mass flux. Some previous studies obtained the same trend of flow boiling heat transfer coefficient (Saitoh et al., 2005; Oh et al., 2011; Huo et al., 2004). Figure 4.9b shows the heat transfer coefficient at T_{in} = 35 °C. The same phenomena are observed as one at T_{in} = 23 °C. However, the transition point of vapor quality shifts from 0.1 to 0.2. Hence, increasing the inlet temperature enhances the nucleate boiling or enlarges the range of nucleate boiling dominated region.

Figure 4.10a shows the effect of heat flux on the flow boiling heat transfer coefficient in the microtube without orifice at G = 550 kg/m^2·s. In the subcooled regime, the heat transfer coefficient increases as vapor quality increases. Similar results were also observed in previous studies (Lazarek and Black, 1982; Ali et al., 2011; Basu et al., 2011) Ali et al. (2011) explained that the flow was characterized as bubbly flow in the subcooled regime. Heat was transferred from liquid to bubbles. As heat flux increased, more nucleation sites were activated. As a result, the heat transfer was enhanced. In the saturated boiling regime, the heat transfer coefficient increases as heat flux increases at $\chi < 0.2$. It indicates the nucleate boiling as dominated mechanism. Basu et al. (2011)

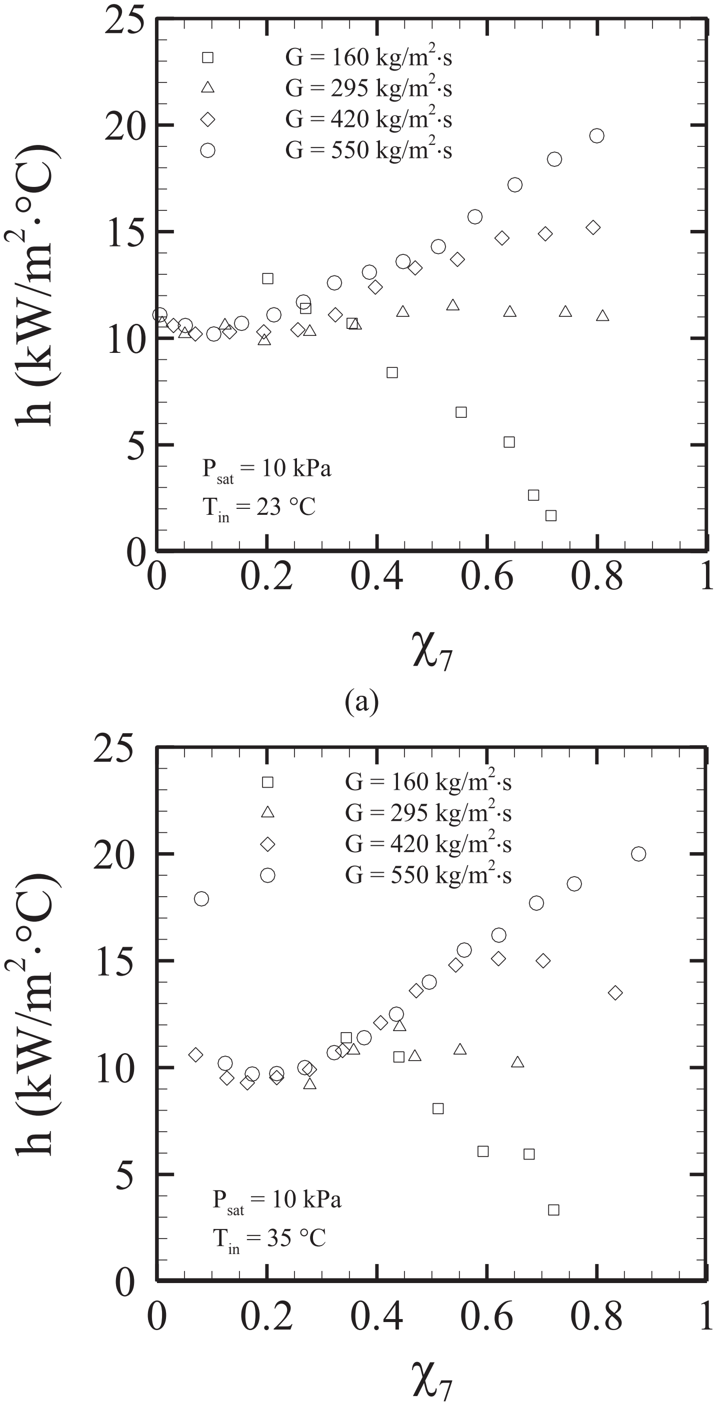

(a)

(b)

Figure 4.9: Heat transfer coefficient at the location of x = 125 mm. (a) T_{in} = 23 °C; (b) T_{in} = 35 °C.

suggested that the transient evaporation of the thin film liquid surrounding elongated bubbles was also a heat flux dependent process. High heat flux increased the evaporation rate, which led to more vapor generation and increased mixing. The heat transfer was enhanced and increased as heat flux increased. Due to the lack of flow visualization in current experiment, the physical mechanism of heat transfer needs to be proven. At $\chi < 0.2$, the heat transfer coefficient decreases as vapor quality increases. Basu et al. (2011) found the same trend and explained that the increased vapor mass inhibited the heat transfer process, which decreased heat transfer coefficient at high vapor quality. Ali et al. (2011) considered that the annular flow with waves was formed at medium vapor quality. The slow decrease in heat transfer coefficient with increasing the vapor quality could be caused by decreasing influence of waves generated at the collapse of the liquid plugs. Yen et al. (2003) explained that the decreasing heat transfer characteristic with vapor quality was caused by the size of nucleate bubble limited in the confined space. When bubble grew, they immediately attached to the surrounding wall of the microtube. Thus, the heat transfer coefficient was suppressed under high heat fluxes or mass fluxes conditions because of the limited evaporation space. At $\chi > 0.2$, the heat transfer coefficient is independent of heat flux and increases as vapor quality increases, which indicate the forced convective boiling as dominated mechanism. The increase of heat transfer coefficient with vapor quality is caused by the increased local velocity. The similar trend of heat transfer coefficient was also presented by Basu et al. (2011). Yen et al. (2006) did the flow visualization. They reported that at high vapor quality, no bubble nucleation was observed. The flow pattern consisted only of annular flow and dry-out

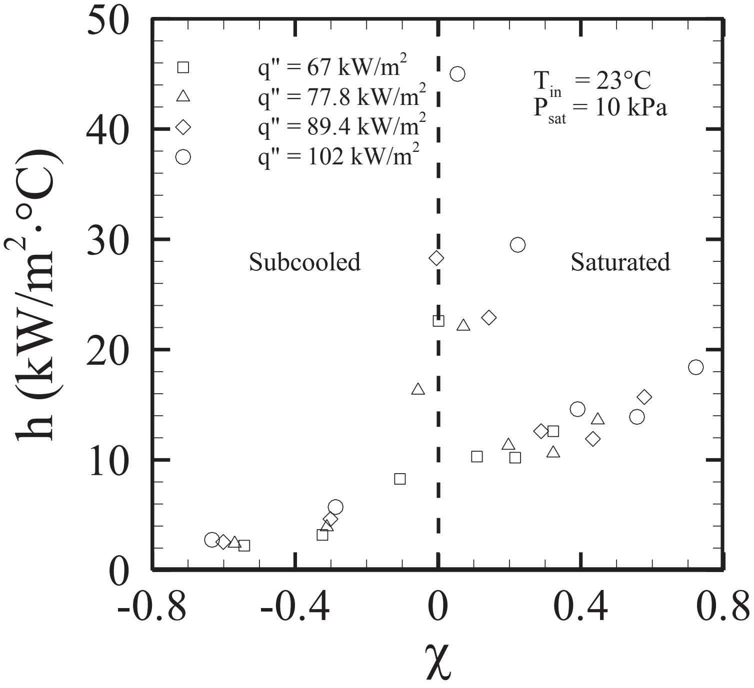

(a)

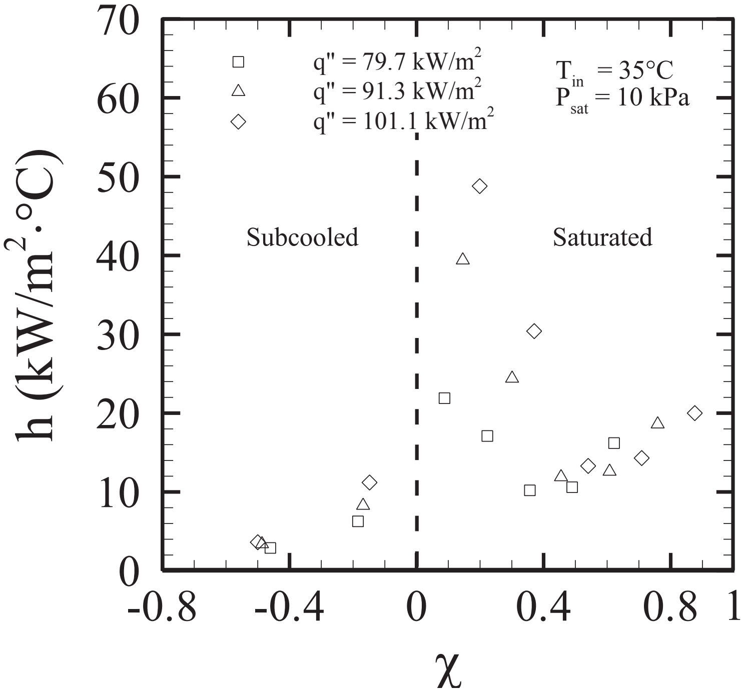

(b)

Figure 4.10: Local heat transfer coefficient at G = 550 kg/m^2·s and P_{sat} = 10 kPa. (a) T_{in} = 23°C; (b) T_{in} = 35°C.

As mentioned by Basu et al. (2011), increasing saturation pressure decreases the surface tension and density ratio (ρ_l/ρ_v) that could affect flow patterns and bubble growth, and regions. The same phenomenon is observed at T_{in} = 35 °C, as shown in Figure 4.10b. The transition point shifts from 0.2 to 0.4.

Figure 4.11 shows the local heat transfer coefficient at G = 295 kg/m^2·s. The heat transfer coefficient increases as saturation pressure increases. The same phenomenon was observed by the previous studies (Ali et al., 2011; Saitoh et al., 2005; Basu et al., 2011). increases the degree of inlet subcooling and decreases the enthalpy of vaporization that affect the onset of boiling. Thus, the effect of saturation pressure on flow boiling heat

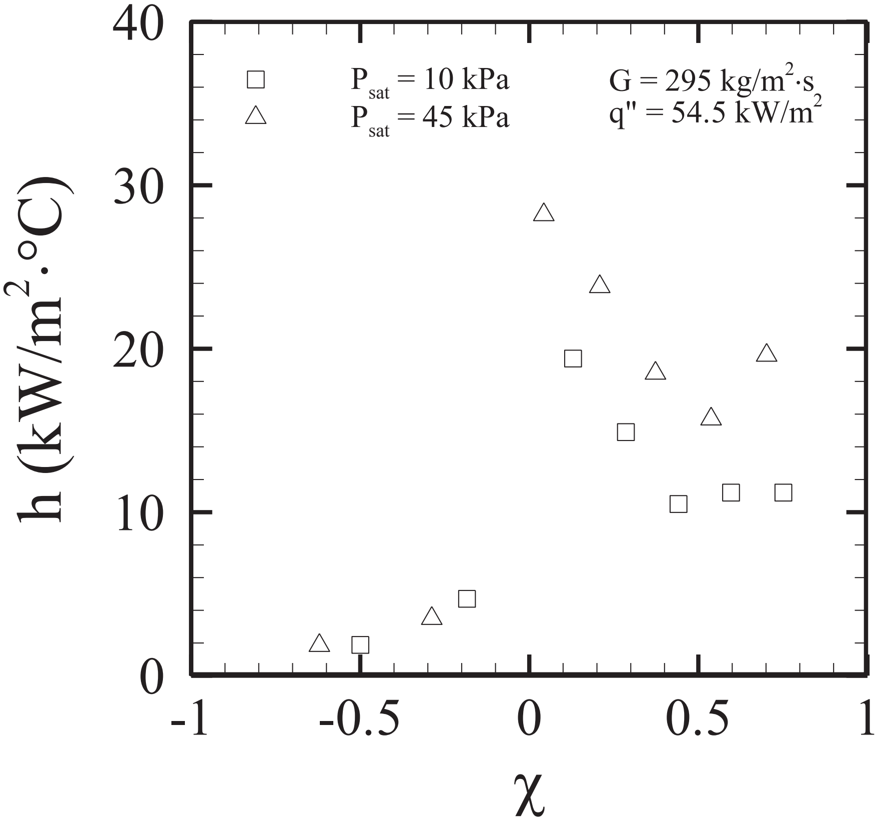

Figure 4.11: Local heat transfer coefficient in the microtube without orifice at G = 295 kg/m^2·s.

transfer is the combined result of all factors. Saitoh et al. (2005) also reported an increase in heat transfer coefficients with an increase of saturation pressure in their study with R134a as working fluid. They found the effect of saturation pressure to be more dominant at smaller diameters. Huo et al. (2004) did the experiment in the small tube with a diameter of 2.01 mm using R134a as working fluid. They found that the heat transfer coefficient increased as saturation pressure increased.

Six flow boiling heat transfer correlations are selected to compare with the experiment. Some details of correlations are listed in Table 4.4. The equations of correlations have been introduced in Chapter 2. The mean absolute error is calculated as,

$$MAE = \frac{1}{N}\sum_{i=1}^{N}\left|\frac{y_{Exp,i} - y_{Pred,i}}{y_{Exp,i}}\right| \tag{4.1}$$

where, N is the number of data; y is the objective parameter. In this work, 367 data points of saturated flow boiling heat transfer coefficients are obtained. Figure 4.12 shows the comparisons between the experiment and previous correlations from literatures. The existing correlations either over predict or under predict the heat transfer coefficient. A new correlation is developed based on the current experimental data,

$$h = 1.7 \times 10^{10} Bo^{0.1} We^{-0.037} \left(\frac{\rho_l}{\rho_v}\right)^{-2.89} \tag{4.2}$$

Figure 4.13 shows the comparison of heat transfer coefficient between experiment and new correlation. The mean absolute error is 32.7%. Figure 4.14 shows the heat transfer coefficient at two mass fluxes and saturation pressures in the microtubes with 20% orifice and without orifice at T_{in} = 23 °C. Generally, the heat transfer coefficient in both microtubes with 20% orifice and without orifice increases as the saturation pressure increases. At P_{sat} = 10 kPa, there is no obvious difference of heat transfer coefficients between the microtubes with 20% orifice and without orifices at G = 160 and 420 kg/m^2·s. However, the difference can be observed at G = 160 kg/m^2·s as the saturation pressure increases to 45 kPa. It indicates that the addition of inlet orifice can enhance the heat transfer at low mass flux and high saturation pressure, where the nucleate boiling is dominant. At high mass flux and low saturation pressure, the forced convective boiling also contributes to the heat transfer. The orifice shows a negligible effect on heat transfer coefficient in this regime.

Table 4.4: The selected correlations for predicting the flow boiling heat transfer

Reference	Notes	MAE
Lazarek and Black (1982)	R113; D_h = 3.15 mm; G = 125 - 750 kg/m^2·s; q'' = 1.4 - 38 W/cm^2; Re_{lo} = 860 - 5500; $Bo = 2.3\times10^4 - 76\times10^4$ Vertical; Circular microchannel;	50.7%
Tran et al. (1996)	R12, R113; D_h = 2.4 - 2.92 mm; G = 44 - 832 kg/m^2·s; q'' = 0.36 - 12.9 W/cm^2; Horizontal; Circular and rectangular;	55.1%
Warrier et al. (2002)	FC-82; Bo = 0.00027 - 0.00089; χ = 0.03 - 0.55; D_h = 0.75 mm; L/D_h = 409.8; G = 557 - 1600 kg/m^2·s; q'' = 0 - 0.6 W/cm^2; Horizontal; Rectangular channel;	76.6%
Kandlikar and Balasubramanian (2004)	Correlation Paper	77.5%
Baus et al. (2011)	R134a; P_{sat} = 490 - 1160 kPa; G = 300 - 1500 kg/m^2·s; q'' = 0 - 35 W/cm^2; ΔT_{in} = 5 - 40 °C; χ_e = 0 - 1; Horizontal; Circular channel;	83.9%
Saitoh et al. (2007)	Correlation Paper	95.9%

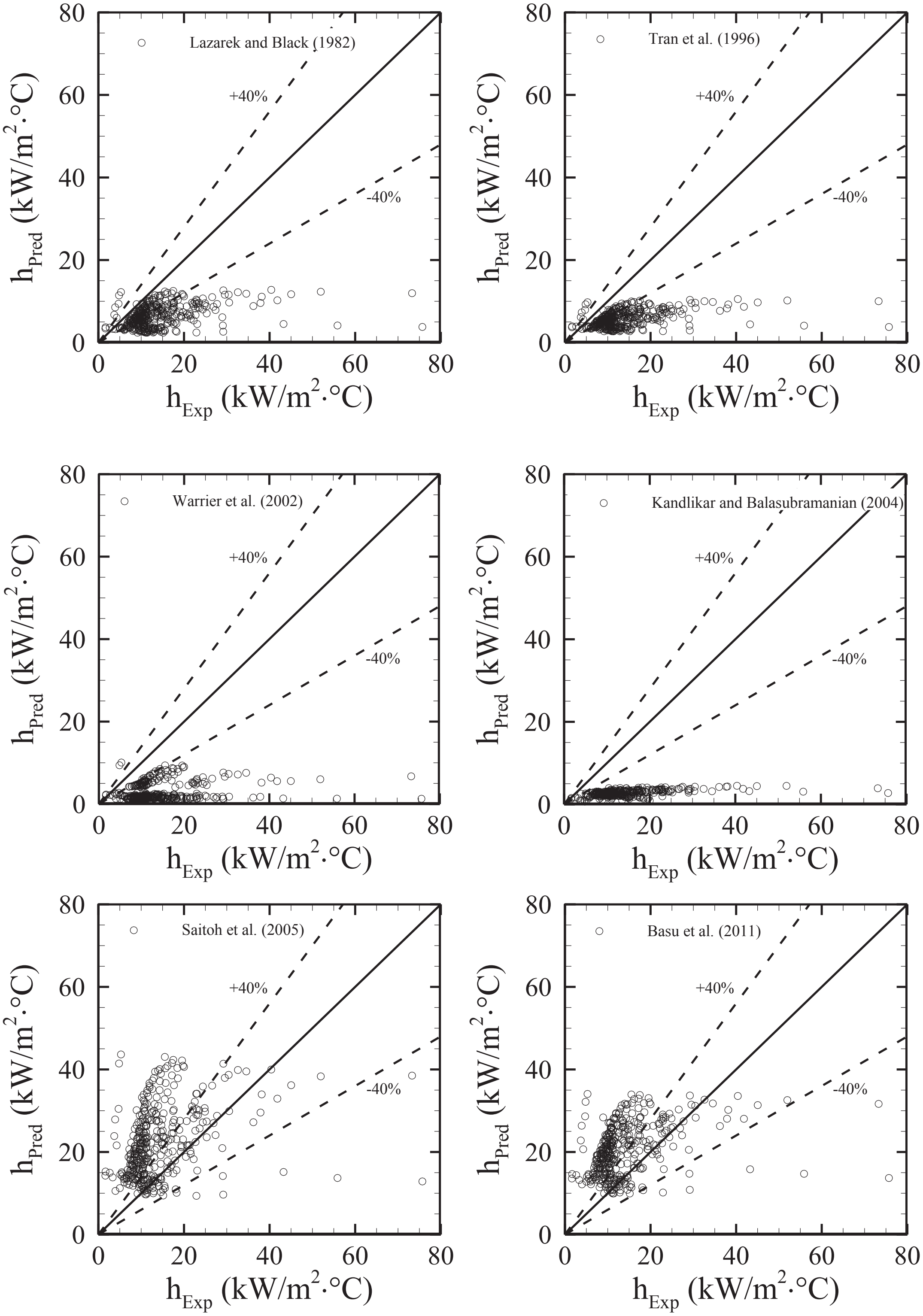

Figure 4.12: Comparisons of flow boiling heat transfer coefficients between experimental data and existing correlations in literatures.

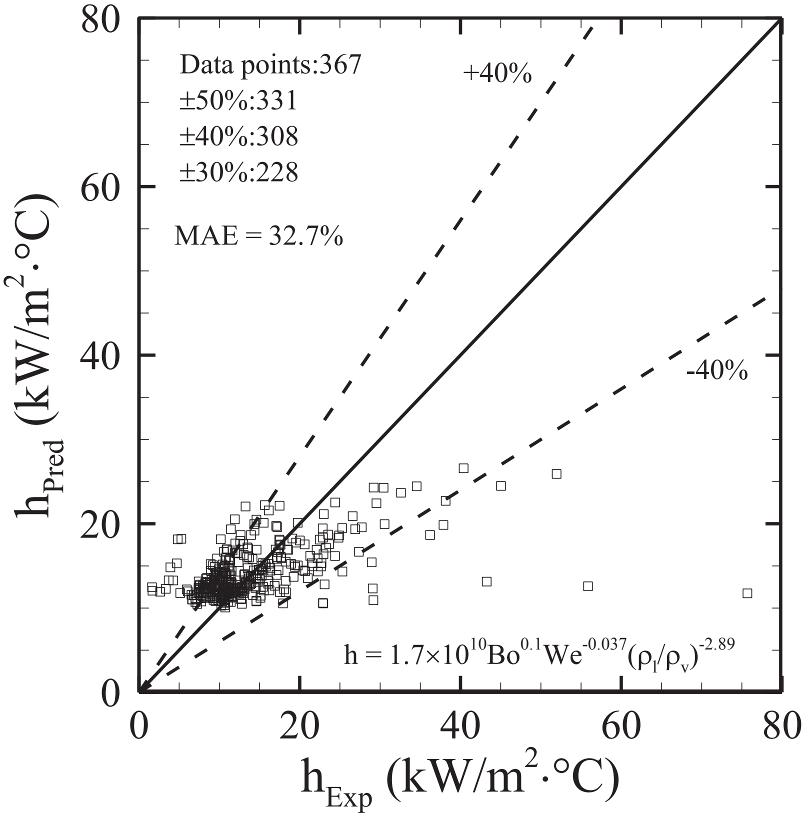

Figure 4.13: Comparison of heat transfer coefficient between experiment and new correlation.

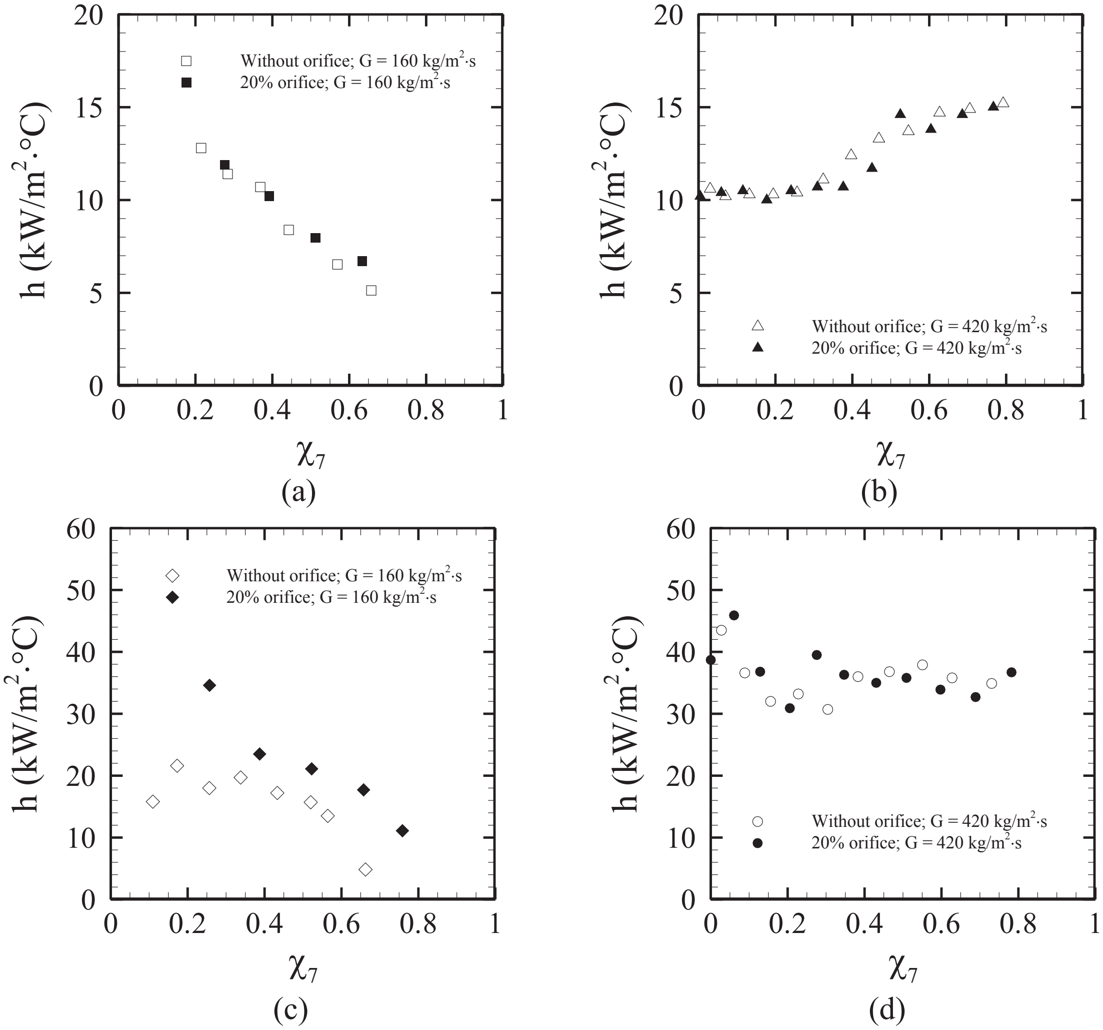

Figure 4.14: Heat transfer coefficient at the location of *x* = 125 mm. (a) G = 160 kg/m^2·s, P_{sat} = 10 kPa; (b) G = 420 kg/m^2·s, P_{sat} = 10 kPa; (c) G = 160 kg/m^2·s, P_{sat} = 45 kPa; (d) G = 420 kg/m^2·s, P_{sat} = 45 kPa.

Chapter 5

5 Effect of Inlet Orifice on Flow Instability

The previous chapter investigated the effects of inlet orifice with different sizes on the two-phase pressure drop, critical heat flux, and flow boiling heat transfer. The flow instability was eliminated completely by the orifice and upstream throttling valve. The operating condition was stable. This chapter is to investigate the effect of inlet orifice on flow boiling instability in single horizontal microtube. No throttling valve is applied in this experiment. The real-time pressure and temperature oscillations in the microtubes with area ratios of 50%, 35%, and 20% are recorded and compared. The magnitude, amplitude, and frequency of flow oscillation are present.

5.1 Experimental Procedure

In the measurement of flow instability, the mass flux ranges from 700 to 3000 $kg/m^2 \cdot s$ and the heat flux varies from 6 to 27 W/cm^2. The exit pressure and inlet temperature are fixed at 17 kPa and 24 °C. The flow map of instability can be divided by two boundaries: the onset of flow instability and the onset of flow re-stability, as shown in Figure 5.1. The onset of flow instability is defined as the beginning of oscillations or the transition from a stable regime to an unstable regime. The onset of flow re-stability is defined as the transition from an unstable regime to a stable regime. The oscillation magnitude and amplitude are calculated as,

$$MAG = \frac{1}{M}\sum y_i \tag{5.1}$$

$$AMP = Max\{y_i\} - MAG \tag{5.2}$$

where, M is the total number of data points; y is the measured parameter. Two measurement procedures are carried out to acquire these two boundaries.

1. The onset of flow instability: The experiment is conducted by fixing the mass flux applied to the microtube. The electrical power is increased by a small increment until fluctuation starts. If the fluctuation is due to a disturbance of operation, the flow will return to the original stable condition after a period of time, as mentioned by Kakac and Bon (2008). The measurements are first carried out in the microtube without orifice to determine the time after which the flow instability caused by operation disappears. The result shows that the flow oscillation caused by the operation disappears after 10 to 20 minutes, as was observed for the tested range of mass fluxes. Hence, in the experiment, the flow is considered to be stable if the flow oscillation vanishes within 30 minutes. The electrical power is then increased with a small increment until fluctuation occurs again. If the oscillation persists for longer than 30 minutes, the flow is deemed to be unstable. The

pressure and temperature at the inlet and outlet are recorded for a time span of 5 minutes at a frequency of 400 Hz in order to capture the oscillation features.

2. The onset of flow re-stability: The onset of flow re-stability is defined as the transition from an unstable regime to a stable regime. Therefore, the mass flux cannot be maintained constant. In order to obtain the mass flux at the onset of flow re-stability, the mass flux is first selected in the single-phase liquid regime. As the heat flux increases, the flow instability occurs due to flow boiling. Further increase of the heat flux causes the flow to follow a stable trend again at a lower mass flux than the original value. This mass flux corresponds to the onset of flow re-stability. The pressure and temperature at inlet and outlet are recorded.

5.2 Onset of Flow Instability without Inlet Orifice

5.2.1 Real-time Pressures and Temperatures

The flow instability in the single microtube without inlet orifice is investigated first to understand the features of flow oscillations. The stable and unstable regimes are captured and shown in Figure 5.1. Curve fitting is performed and shows that the ratios of heat flux to mass flux at the onset of flow instability and re-stability exhibit an almost linear relationship. A similar stable and unstable regimes map of heat flux versus mass flux was proposed by Wang et al. (2007), Wang and Cheng (2008) and Celata et al. (2010). They also found that the mass flux and heat flux have a linear relationship at the boundaries of stable and unstable regimes. Wang et al. (2007) investigated the flow oscillation in a single trapezoidal microchannel with a hydraulic diameter of 186 μm and a length of 30 mm. They captured the boundary of onset of flow instability which exhibited the same behaviour as the one observed in the current work. However, they did not capture the onset of flow re-stability. Wang and Cheng (2008) proposed that the stable and unstable flow boiling regimes depended on the *Boiling number* and inlet temperature. Celata et al. (2010) built a similar flow pattern map in a microtube with a hydraulic diameter of 480 µm using FC-72 as the working fluid. The heat fluxes obtained at the onsets of flow instability and re-stability were lower than the ones obtained in the present work for the same mass flux. This may be attributed to the reduced hydraulic diameter, which induces the flow pattern to shift, and forms bubbles which depart from the walls to fill up the tube

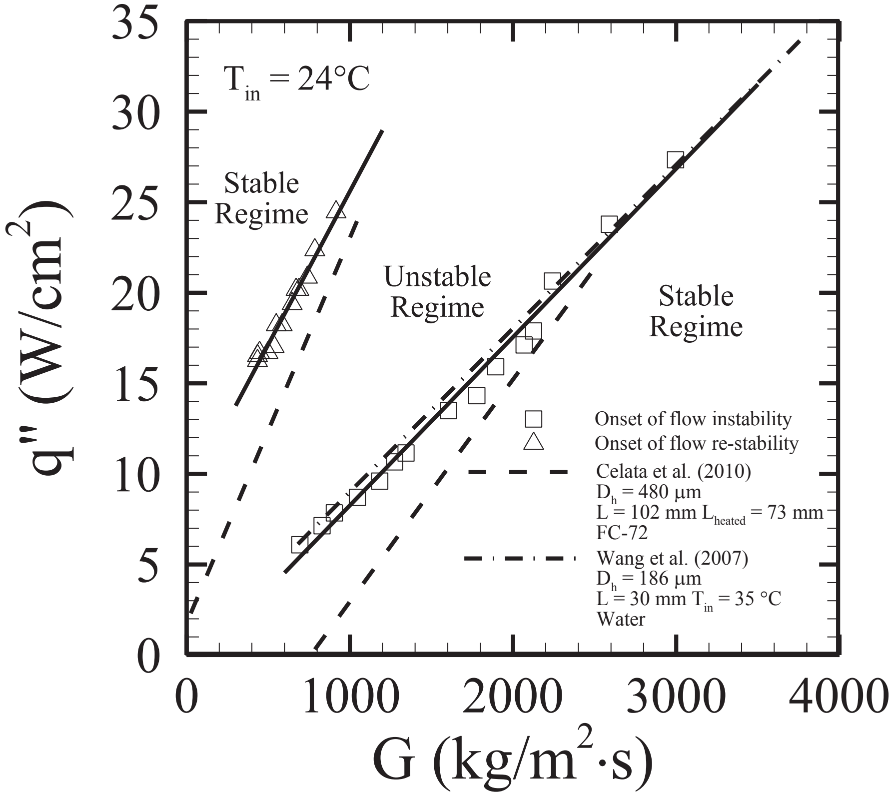

Figure 5.1: The map of flow stability regimes in single microtube without orifice at different heat and mass fluxes (solid lines are the curve fittings of experimental data).

at a lower heat flux. The mass flux mentioned in this work corresponds to the one at the onset of flow instability.

Four types of oscillations are observed at the onset of flow instability at the tested range of mass fluxes and heat fluxes: a combination of Ledinegg and density-wave oscillation (LD); a combination of Ledinegg, density-wave and pressure-drop oscillation (LDP); pressure-drop oscillation; transition instability between pressure-drop and density-wave oscillations (TPD). At low mass fluxes (< 1000 kg/m^2·s), the onset of flow instability occurs at a small heat flux. A combination of Ledinegg and density-wave instability (LD) is observed, as shown in Figure 5.2. When oscillation begins, the mass flow rate suddenly drops to a lower value corresponding to the Ledinegg instability. Then, the flow starts to fluctuate at a high frequency and small amplitude. The frequency of fluctuation is close to the transit time of a continuous wave (~ 1 Hz), as shown in Figure 5.2b. This feature indicates the existence of density-wave oscillation. Kandlikar (2006) assumed that the pressure increase inside the bubble introduced a pressure spike in the microtube. This pressure spike overcame the inertia of the incoming liquid and the pressure inside the inlet reservoir and thus the reversed flow was created. A similar flow oscillation was also observed by Schilder et al. (2010).

As mass flux increases to 977 kg/m^2·s, the amplitude of oscillation increases while the frequency decreases, as shown in Figure 5.3a. In Figure 5.3b, two oscillations, one at a low, and the other at a high frequency, can be distinguished. A high frequency and small amplitude are characteristics of the LD oscillation. The inlet pressure suddenly drops after the LD oscillation and increases with a gradually increasing tendency. A large amplitude and low frequency characterize the pressure-drop oscillation. Pressure

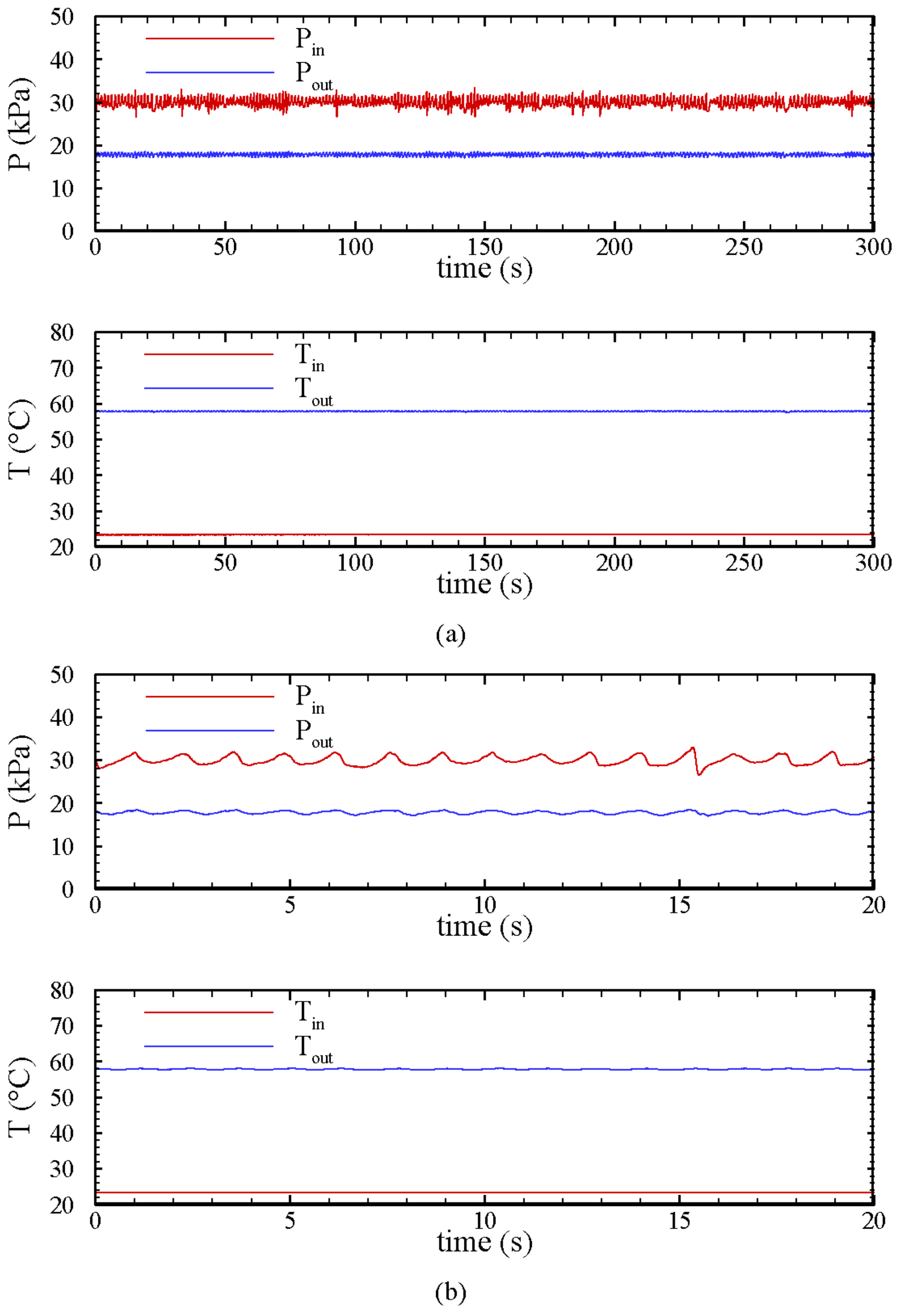

(a)

(b)

Figure 5.2: The combination of Ledinegg and density-wave oscillation (LD) at the mass flux of 763 kg/m^2·s (a) Oscillation in a period of 300s (b) Oscillation in a period of 20s.

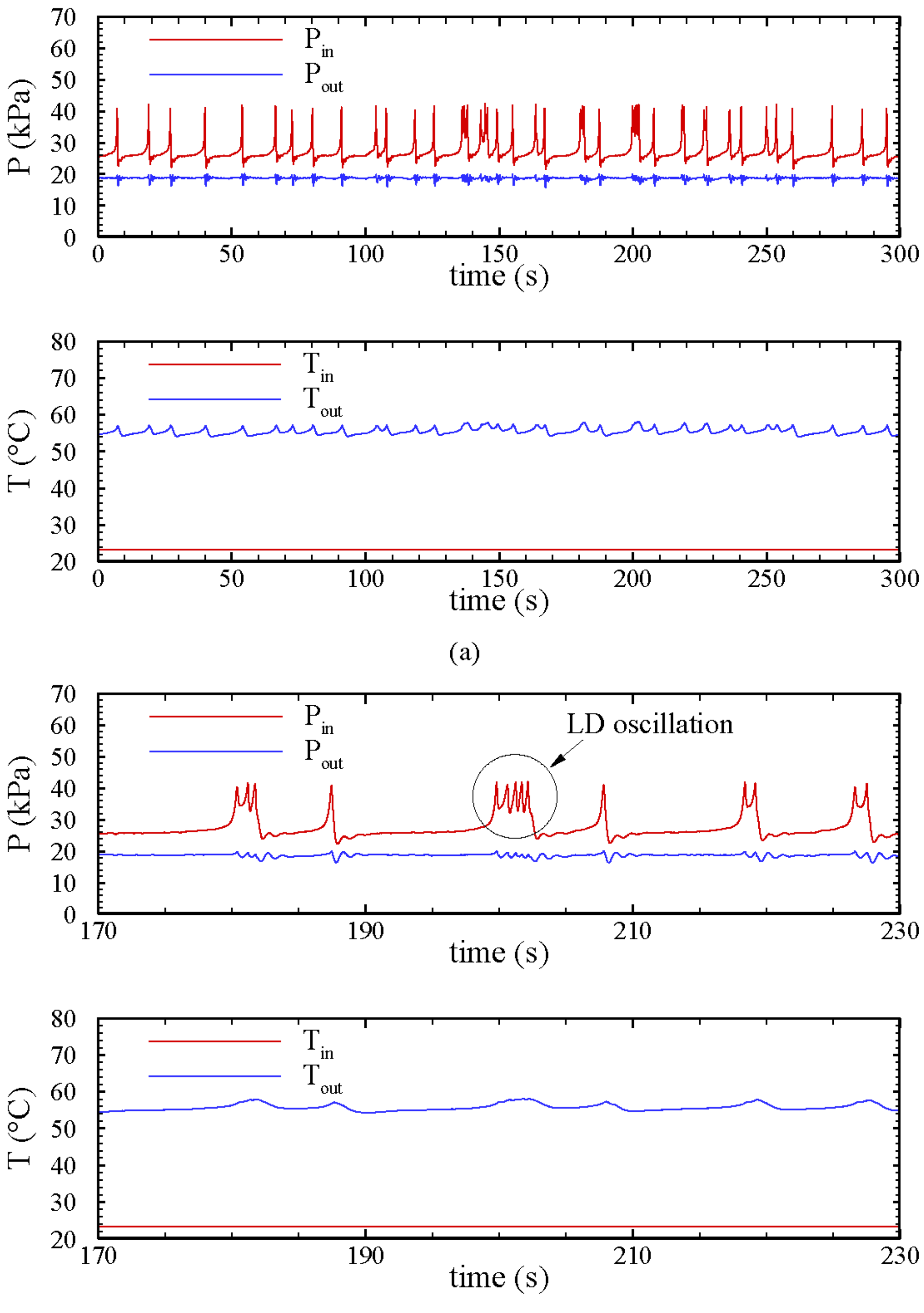

(a)

(b)

Figure 5.3: The combination of Ledinegg, density-wave, and pressure-drop oscillation (LDP) at the mass flux of 977 kg/m^2·s (a) Oscillation in a period of 300s (b) Oscillation in a period of 50s.

fluctuation occurs as soon as the peak of the temperature fluctuation is reached. A similar type of oscillation was also depicted by Barber et al. (2009) in single rectangular microchannel with a hydraulic diameter of 727 μm. Xu et al. (2005) observed the small oscillations as well. They noted that the fresh liquid suddenly invaded and occupied the whole microchannel, leading to a sharp decrease in inlet pressure, and outlet temperature. This was followed by bulk boiling in the microchannels causing small amplitude/high frequency oscillation. This flow oscillation is defined as a combination of Ledinegg, density-wave, and pressure-drop oscillations (LDP).

Figure 5.4 shows the inlet and outlet pressure and temperature oscillations at a mass flux of 1166 kg/m^2·s. LD oscillation cannot be observed. After reaching a maximum value, the inlet pressure suddenly drops, and the oscillation frequency is not periodic. Two different frequencies are observed as shown in Figure 5.4b. Transition oscillation is identified and defined as a combination of pressure-drop and density-wave oscillations (TPD). The high frequency is due to the density-wave oscillation and the low frequency is due to the pressure-drop oscillation. In Figure 5.5, similar oscillations can be detected at a high mass flux, (e.g. 2990 kg/m^2·s). Periodic pressure-drop oscillation cannot be observed at high mass fluxes either. TPD oscillation at low and high mass fluxes has different dominant components. For instance, at the mass flux of 1166 kg/m^2·s, the frequency is very low since the dominant component is the pressure-drop oscillation, and the oscillation consequently transit from density-wave oscillation to pressure-drop oscillation. However, density-wave oscillation dominates at the mass flux of 2990 kg/m^2·s, yielding a high frequency, and causing a transition from pressure-drop oscillation to density-wave oscillation.

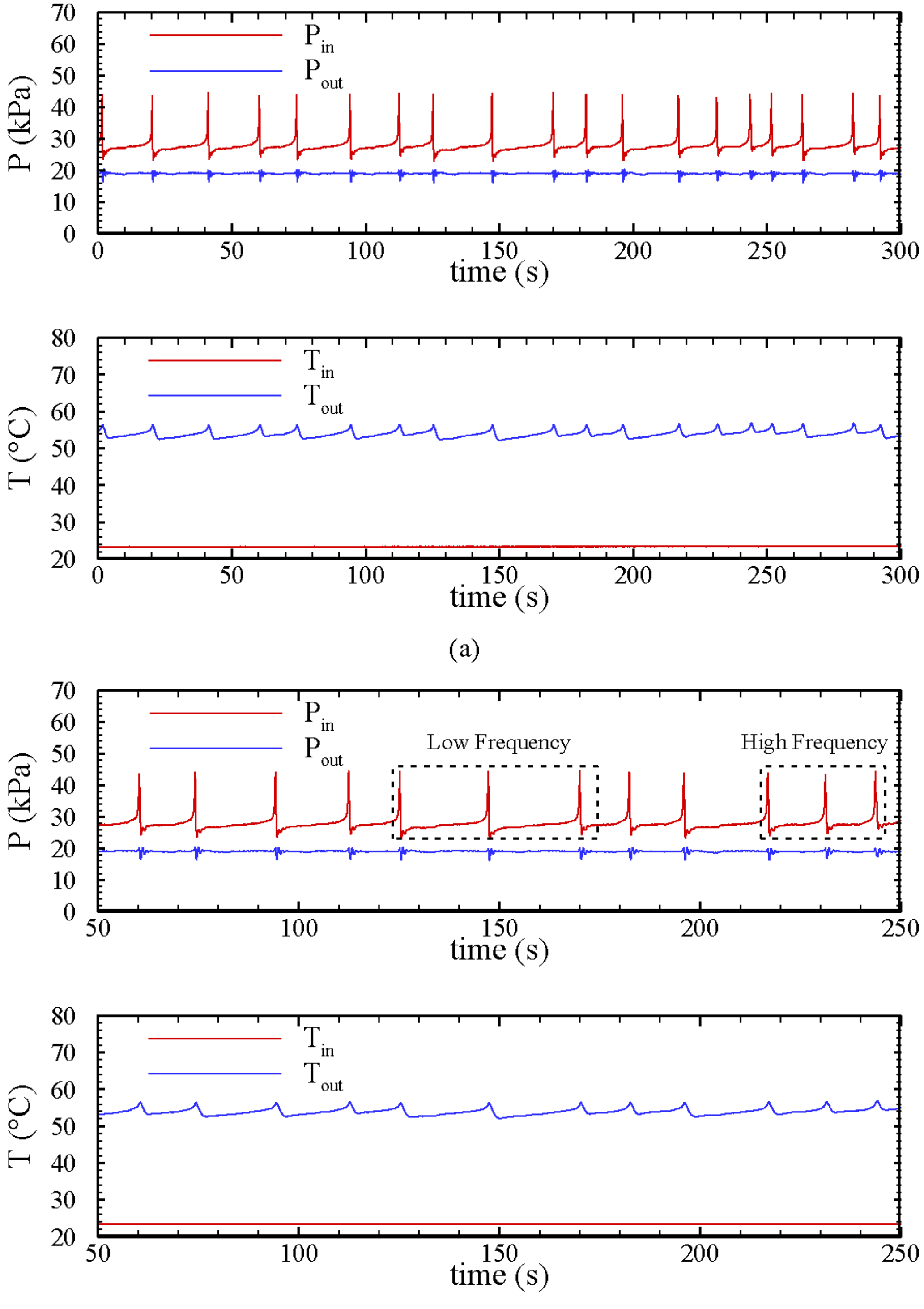

(a)

(b)

Figure 5.4: The transition instability between pressure-drop and density-wave oscillations (TPD) at the mass flux of 1166 kg/m^2·s (a) Oscillation in a period of 300s (b) Oscillation in a period of 200s.

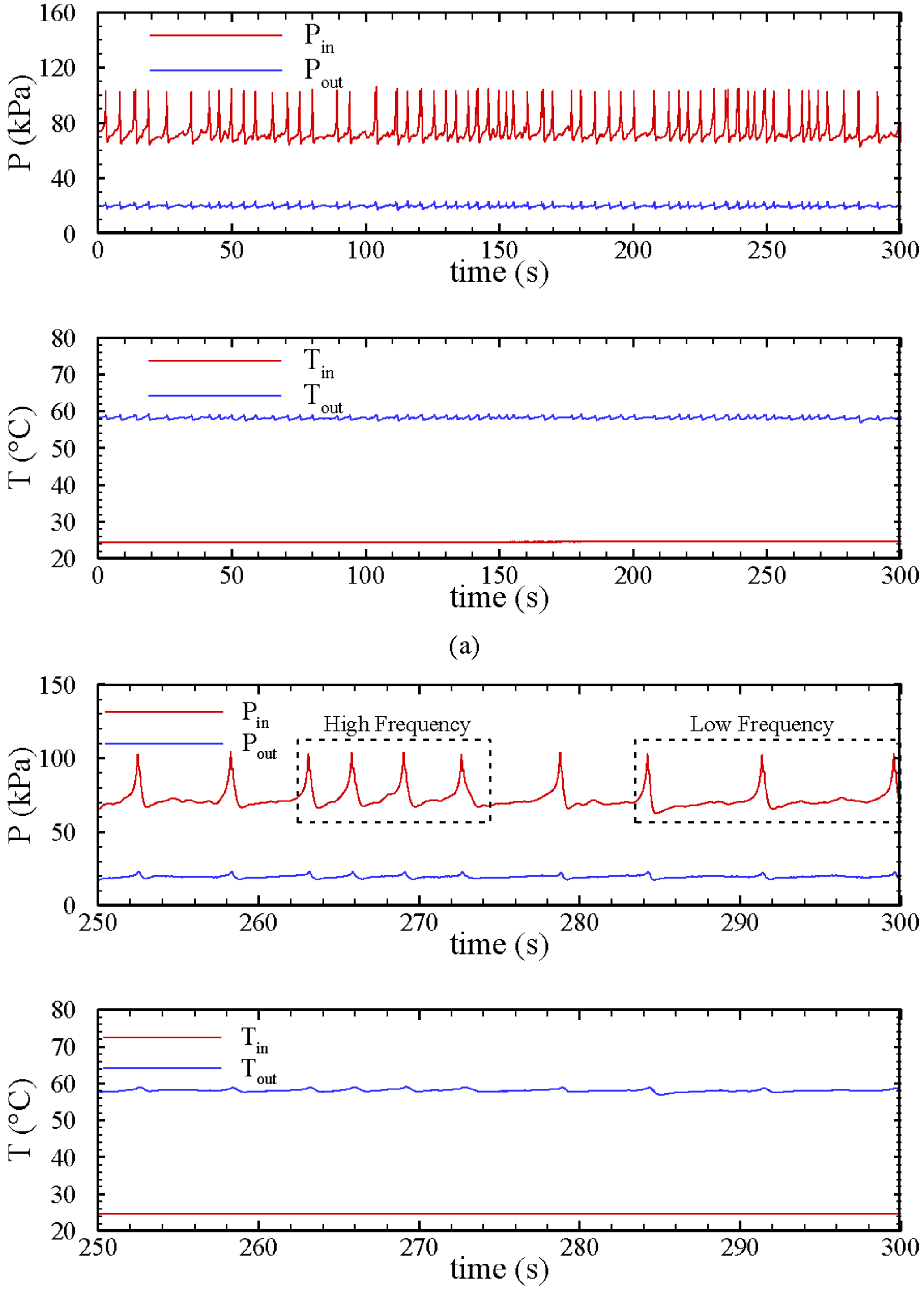

Figure 5.5: The transition instability between pressure-drop and density-wave oscillations (TPD) at the mass flux of 2990 kg/m^2·s (a) Oscillation in a period of 300s (b) Oscillation in a period of 50s.

As the mass flux increases up to 1546 kg/m^2·s, pressure-drop oscillation is observed at the onset of flow instability, as shown in Figure 5.6. The component of density-wave oscillation cannot be detected, and the pressure-drop oscillation occurs in systems having a compressible volume upstream of, or within, the heated section. For this class of instability, the dynamic instability is triggered by the static instability (Boure et al., 1973). The oscillation is periodic, and occurs at a low frequency and large amplitude. Similar oscillations were observed in previous works by Xu et al. (2004) and Wang and Cheng (2008). Xu et al. (2004) assumed that such slow transitional flow was caused by the switch of liquid and two-phase alternation. The flow oscillations could be self-sustained with mass flux feedback control. The pressure and temperature at the inlet and outlet exhibit a small phase shift, as shown in Figure 5.6b. The outlet temperature varies between subcooled temperature and the saturated temperature. When the heat flux increases, the mass flow rate decreases due to the large two-phase pressure drop, and a large bubble is created in the microtube. The bubble expands in both upstream and downstream directions, and bubble core moves downstream. After reaching the exit of the microtube, the bubble quickly moves out of the microtube due to the low pressure at the outlet. The mass flow rate increases sharply and the bulk liquid temperature drops to the subcooled level at the outlet. Then, the liquid temperature increases, and a new large bubble is created and grows. Wang and Cheng (2008) conducted flow visualization and found that the low pressure drop corresponded to the bubbly flow and the high pressure drop was caused by either elongated bubbly/slug flow or annular flow, depending on the mass flux.

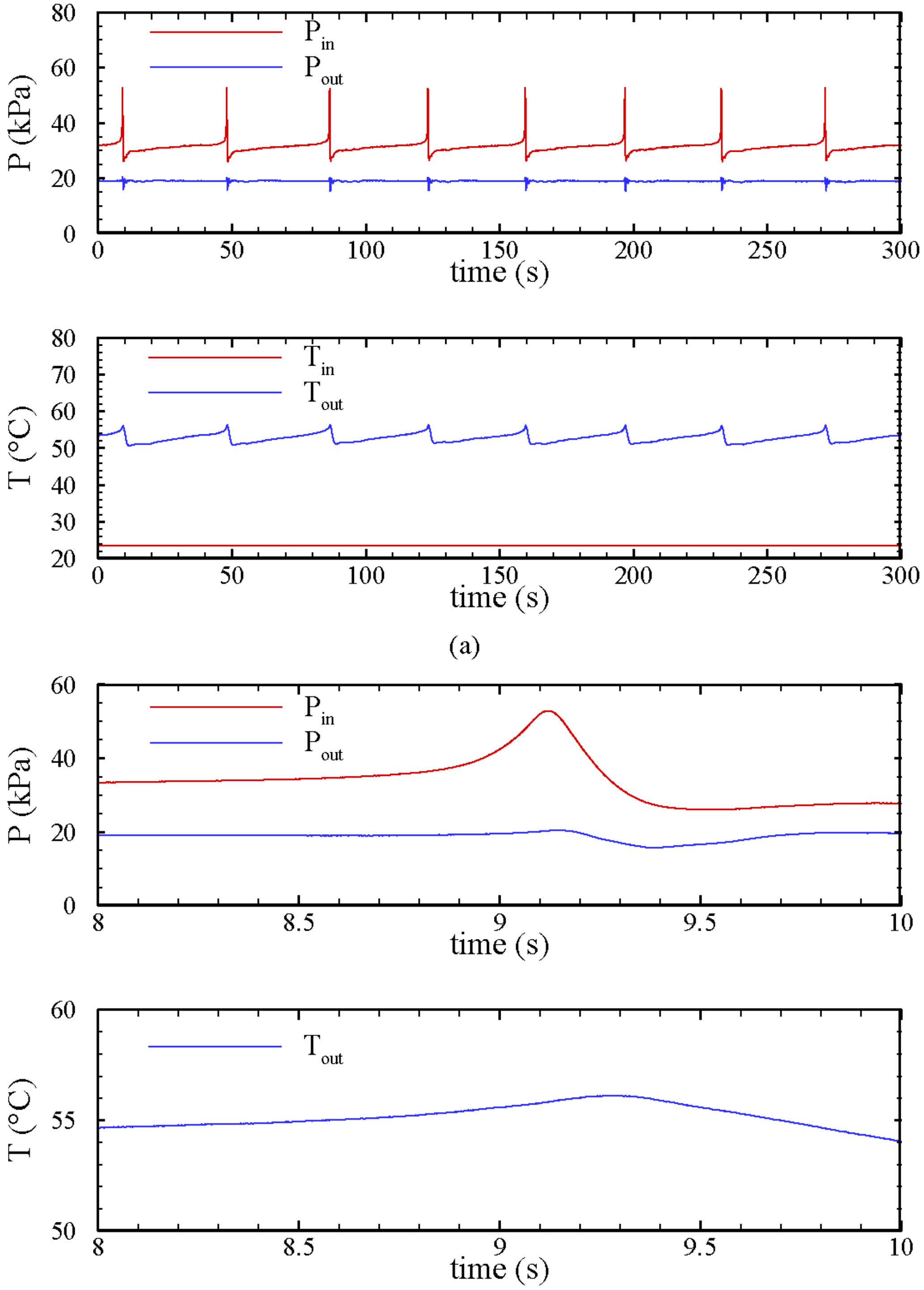

(a)

(b)

Figure 5.6: The pressure-drop oscillation at the mass flux of 1546 kg/m^2·s (a) Oscillation in a period of 300s (b) Oscillation in a period of 2s.

5.2.2 Oscillation Features

The frequency and amplitude at the onset of flow oscillations are shown in Figure 5.7. The frequency of oscillation decreases with increasing mass flux for G < 2400 kg/m^2·s, and increases with increasing mass flux for G > 2400 kg/m^2·s. Moreover, a large gradient of frequency versus mass flux is observed at low mass fluxes (< 1000 kg/m^2·s) and high mass fluxes (> 2700 kg/m^2·s). At low mass fluxes (< 1000 kg/m^2·s), the LD oscillation is observed, which is characterized by a high frequency and a small amplitude. As the mass flux increases, the oscillation changes from LD to LDP. The frequency decreases and the

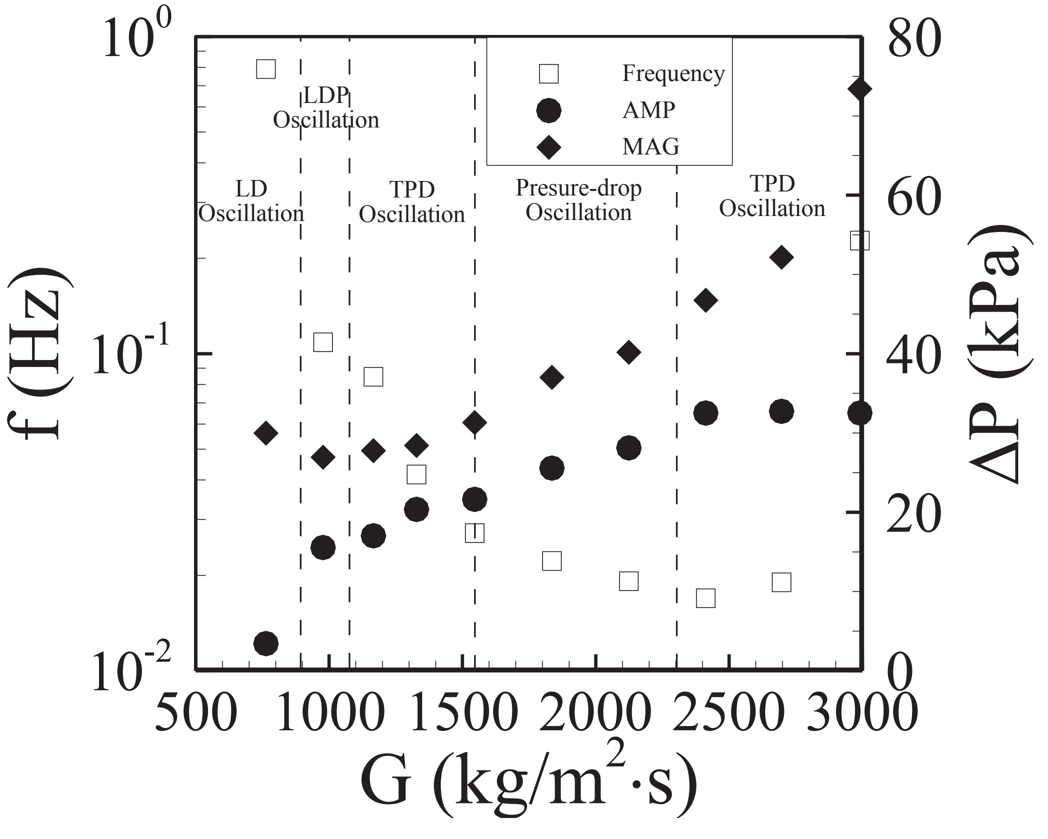

Figure 5.7: The oscillation frequency, magnitude and amplitude of pressure drop at the onset of flow instability in the single microtube without orifice.

amplitude increases due to the presence of pressure-drop oscillation. The pressure-drop oscillation appears as the mass flux increases further, resulting in a reduced frequency and increased amplitude. A transition from pressure-drop oscillation to density-wave oscillation is observed as the mass flux keeps increasing. It is characterized by a large amplitude and a frequency that is similar to that of the LD oscillation. However, the amplitude of TPD oscillation is much larger than that of the LD oscillation due to the initial high mass flux. It is noted that the oscillation amplitude (AMP) remains almost constant, but the time-averaged pressure drop (MAG) increases as mass flux increases in the TPD regime. Generally, as the mass flux increases, the oscillations type at the onset of flow instability changes from a static dominated oscillation to a dynamic dominated oscillation: LD, LDP, pressure-drop, to TPD oscillation.

5.3 Effect of Heat Flux on Flow Oscillation Frequency

Increasing the heat flux from the onset of flow instability causes intensified oscillations, as shown in Figure 5.8. Pure density-wave oscillation can be detected at high heat fluxes as mass flux is higher than 1546 kg/m^2·s. The corresponding frequency is close to 1 Hz. Figures 5.9 and 5.10 show the real-time inlet and outlet pressures at mass fluxes of 977 kg/m^2·s and 1546 kg/m^2·s. At the mass flux of 977 kg/m^2·s, LDP oscillation is detected at the onset of flow instability. As the heat flux increases, the density-wave oscillation becomes more dominant than the pressure-drop oscillation. The oscillation frequency remains lower than 1 Hz. At the mass flux of 1546 kg/m^2·s, an increasing trend of oscillation frequency is observed. Pure density-wave oscillation is detected at the heat flux of 14.8 W/cm^2. Therefore, the pure dynamic oscillations become more dominant

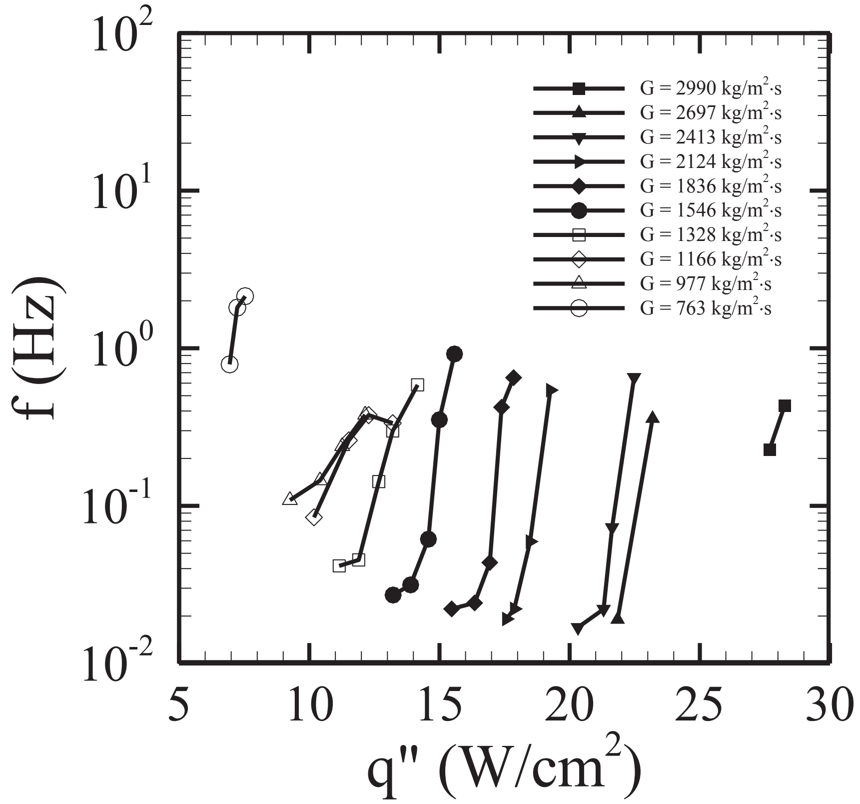

Figure 5.8: The effect of heat flux on oscillation frequency at different mass fluxes. (The mass flux represents the value at the onset of flow instability).

than the combination of static and dynamic oscillations as the heat flux increases further from the onset of flow instability. It is noted that, although oscillation frequency increases with increasing the heat flux at each mass flux, the oscillation amplitude remains approximately constant.

The comparison of the pressure drop of single-phase liquid flow and the onset of flow re-stability are shown in Figure 5.11. Compared to the single-phase liquid pressure drop at the same mass flux, the pressure drop at the flow re-stability boundary is much higher, and is caused by the higher two-phase pressure drop.

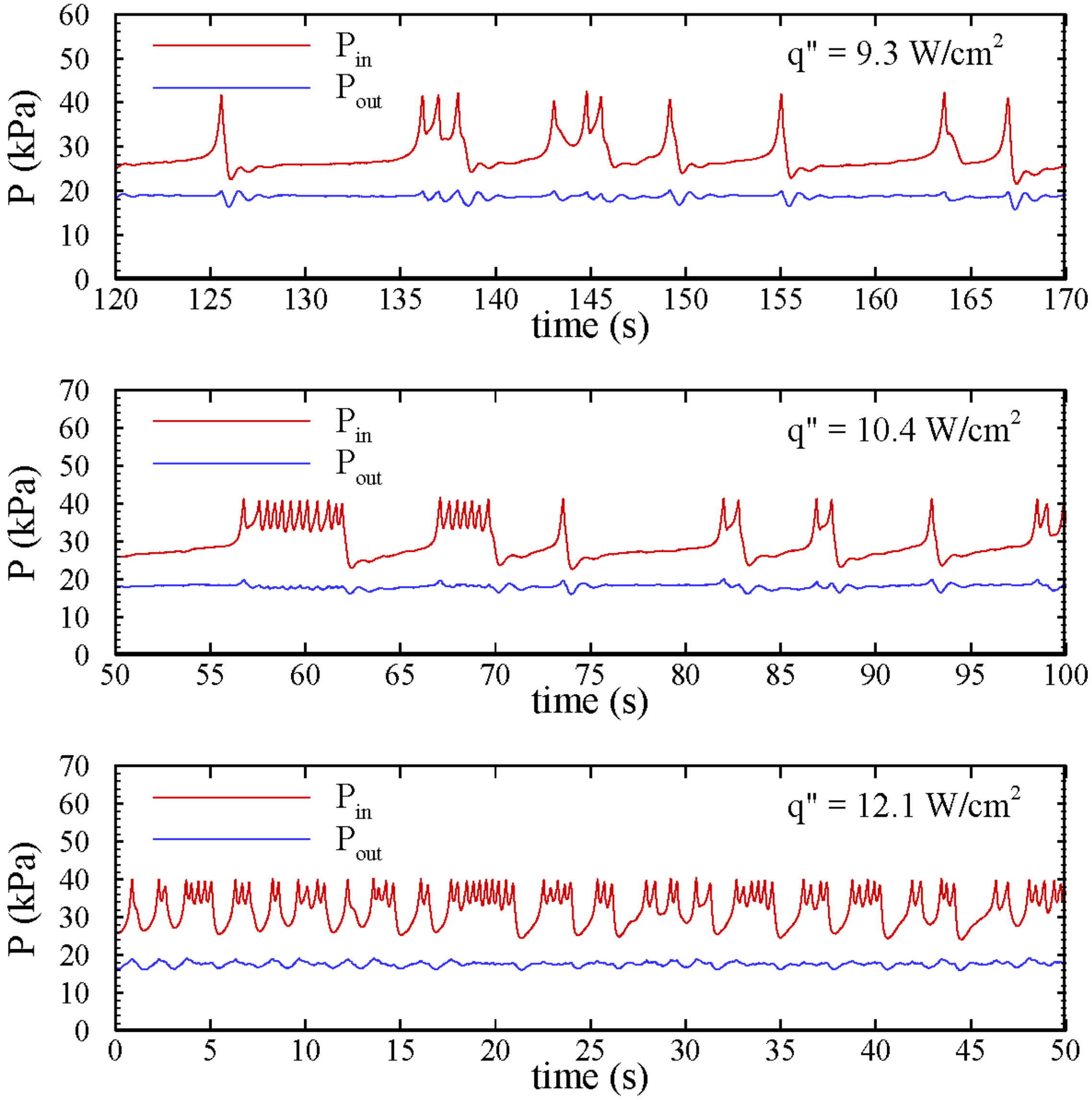

Figure 5.9: The effect of heat flux on the pressures at the mass fluxes of 977 kg/m^2·s.

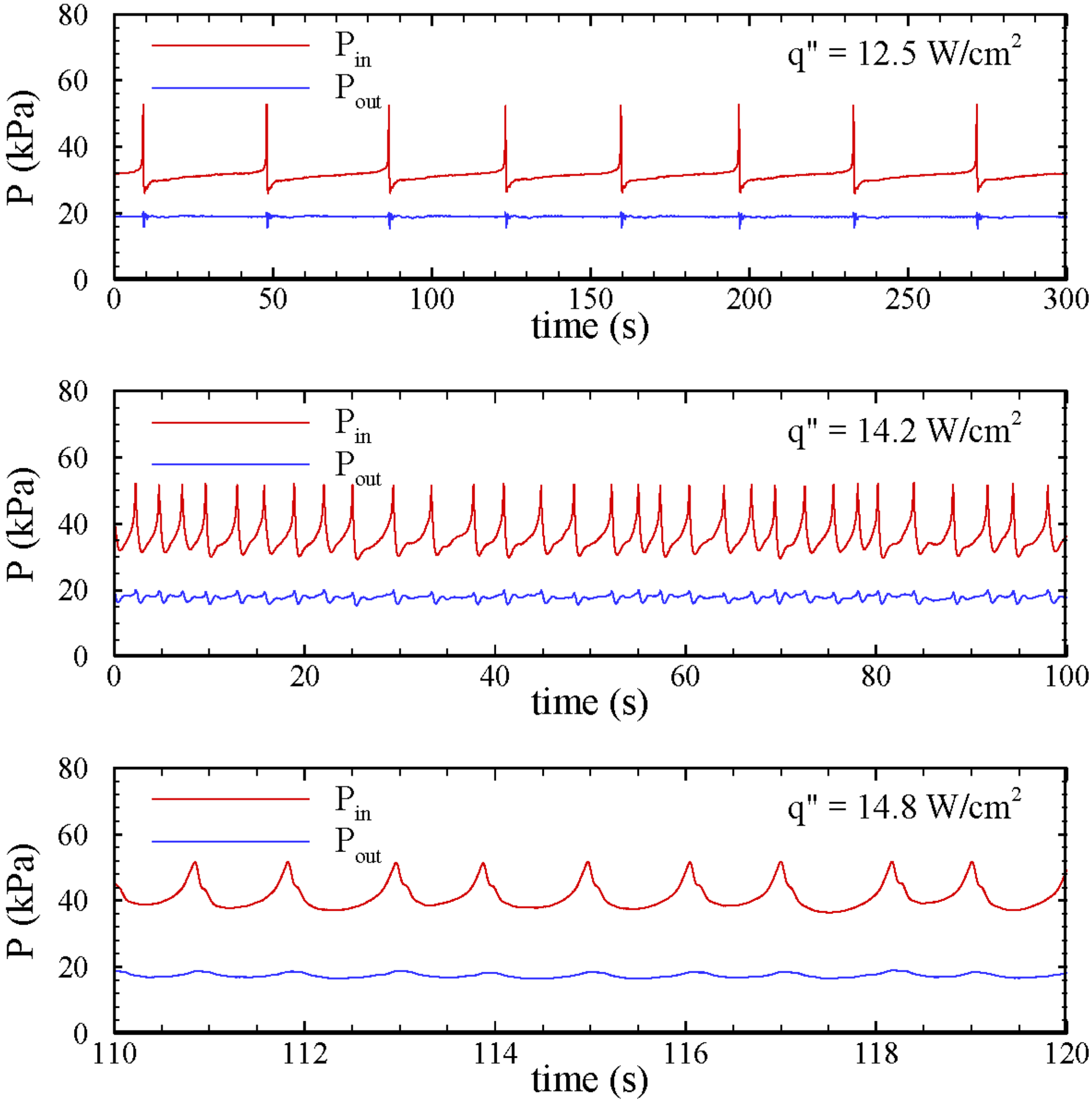

Figure 5.10: The effect of heat flux on the pressures at the mass fluxes of 1546 kg/m^2·s.

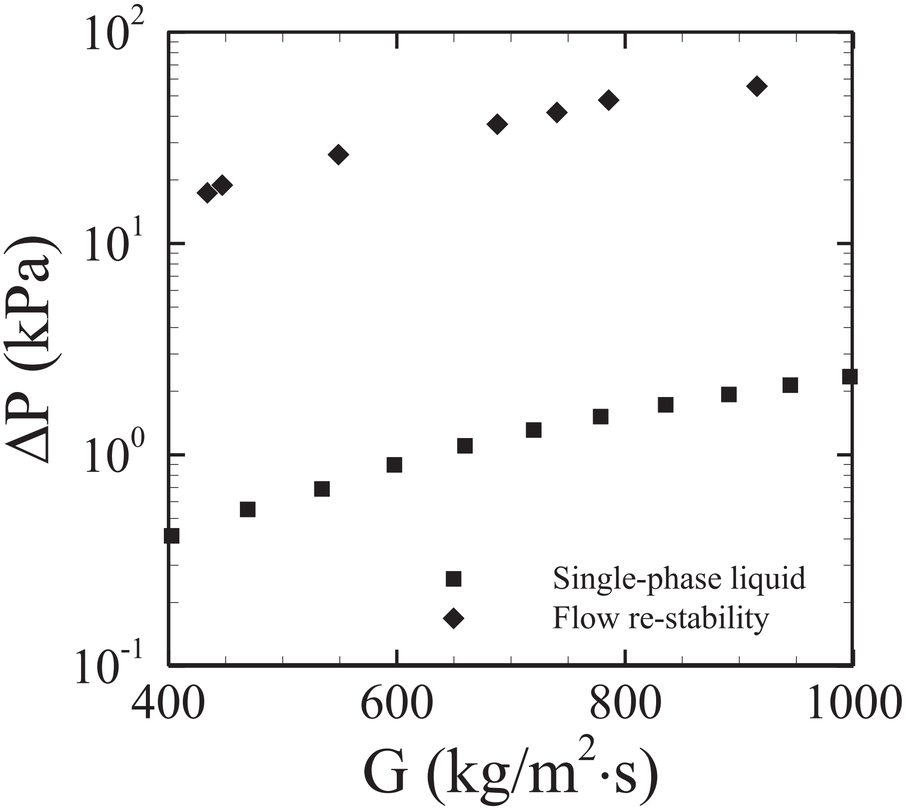

Figure 5.11: The pressure drop at different mass fluxes in the regimes of single liquid phase and onset of flow re-stability.

5.4 Flow Instability with Inlet Orifice

Three area ratios of orifices, 50%, 35%, and 20%, are selected for the present study. The effect of inlet orifice on flow instability is investigated. The real-time inlet pressure of the 20% area ratio orifice is shown in Figure 5.12-14 and compared to other microtubes. The heat flux and mass flux in the microtube with 20% orifice are maintained at the same level as the ones at the onset of flow instability in other microtubes. The outlet gage pressure is maintained at 17 kPa. At the low mass flux of 763 kg/m^2·s, the microtube with 20% orifice exhibits a slightly higher pressure drop. It suggests that the orifice with small area ratio is capable of stabilizing the flow at low mass fluxes without generating a large pressure drop. At the mass flux of 1166 kg/m^2·s, TPD oscillation is observed in the microtubes without orifice, with 50% and 35% orifices at the onset of flow instability. The inlet pressure in the microtube with 20% orifice is approximately equal to the maximum amplitude of oscillations. However, the time-averaged pressure is much larger than that in other microtubes. At the mass flux of 1836 kg/m^2·s, the pressure-drop oscillation is captured. The microtube with 20% orifice exhibits a much larger pressure difference than other microtubes at the same mass flux and heat flux. Nevertheless, the flow is very stable. The microtube with 20% orifice can handle the flow instability and increase the heat flux at the onset of flow instability. It is concluded that decreasing the area ratio of an orifice can enhance the flow stability. If the inlet pressure is larger than the maximum amplitude of oscillations, the orifice is capable of stabilizing the flow. As soon as the maximum inlet pressure of oscillations is known, the proper orifice size can be determined.

Figure 5.15 shows the heat flux at the onset of flow instability at mass fluxes varying from 700 to 3000 kg/m^2·s. The results show that there is negligible difference on heat flux at the onset of flow instability between the single microtube without orifice and the microtube with 50% orifice at a mass flux lower than 2000 kg/m^2·s. As the mass flux increases beyond 2000 kg/m^2·s, the heat flux responsible for launching the oscillations becomes obviously larger than that of the single microtube without orifice. The corresponding oscillation type is the dynamic oscillation. It indicates that a 50% orifice largely influences the dynamic oscillations and noticeably delays the onset of flow instability. For an area ratio of 35%, the heat flux at the onset of flow instability is

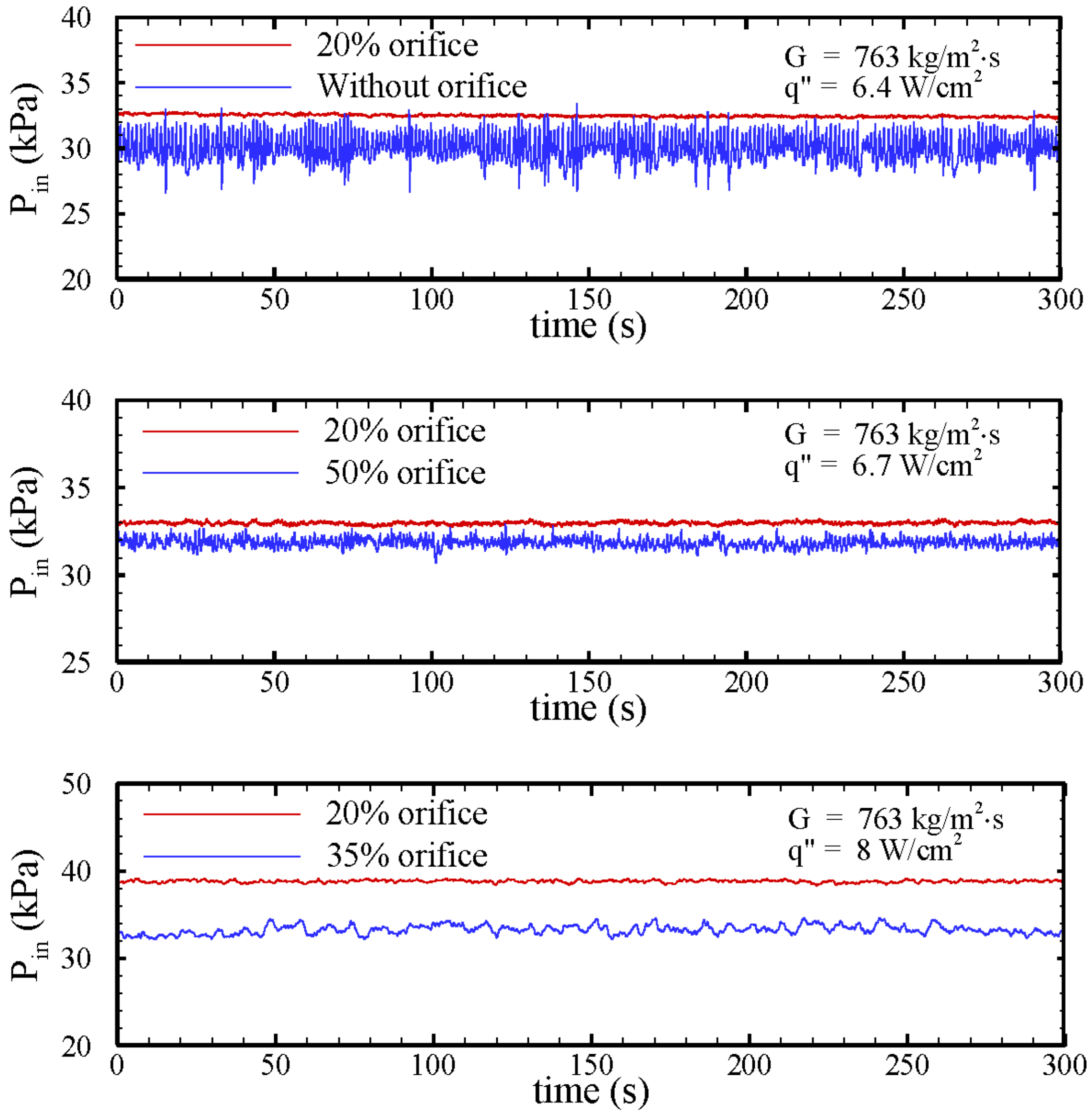

Figure 5.12: Comparisons of inlet pressure at the onset of flow instability in microtubes with and without orifices at $G = 763$ kg/m^2·s.

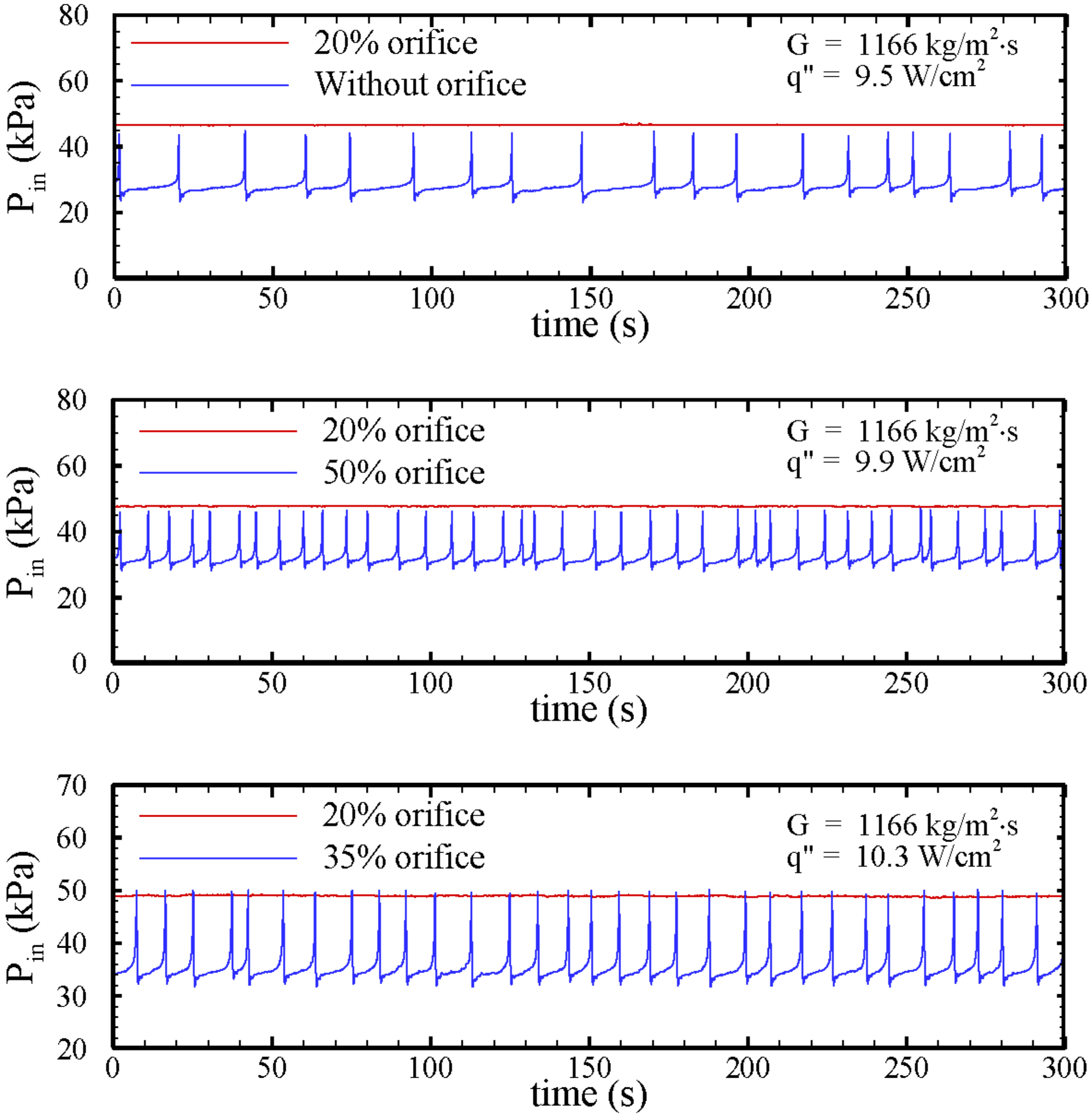

Figure 5.13: Comparisons of inlet pressure at the onset of flow instability in microtubes with and without orifices at $G = 1166$ kg/m^2·s.

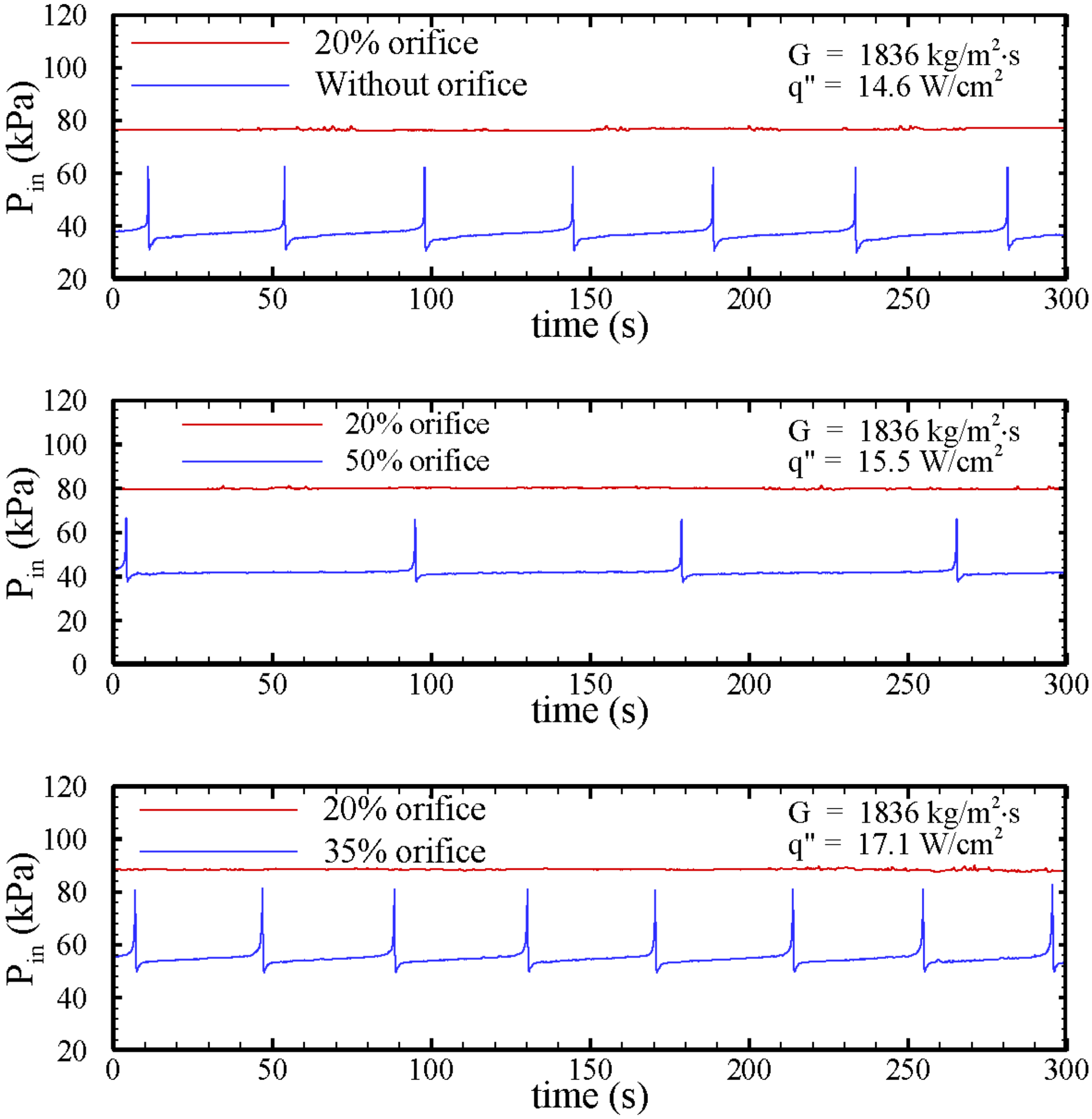

Figure 5.14: Comparisons of inlet pressure at the onset of flow instability in microtubes with and without orifices at G = 1836 kg/m^2·s.

increased. Flow instability at a mass flux larger than 2123 kg/m^2·s cannot be observed even if the heat flux increases up to 27 W/cm^2. Therefore, the orifices of 50% and 35% area ratios have better performance on flow stability at a mass flux higher than 2000 kg/m^2·s since a large inlet pressure is created at high mass flow rates. Bubbles are forced to move downstream due to a high upstream pressure that is larger than the vapor pressure. The reversed flow is blocked by the orifice. Only four mass fluxes are tested in the microtube with 20% orifice due to the extremely large pressure drop. The heat flux at the onset of flow instability is quite larger than the one recorded in other orifices, which illustrates that the 20% orifice can enhance the flow stability drastically at a mass flux

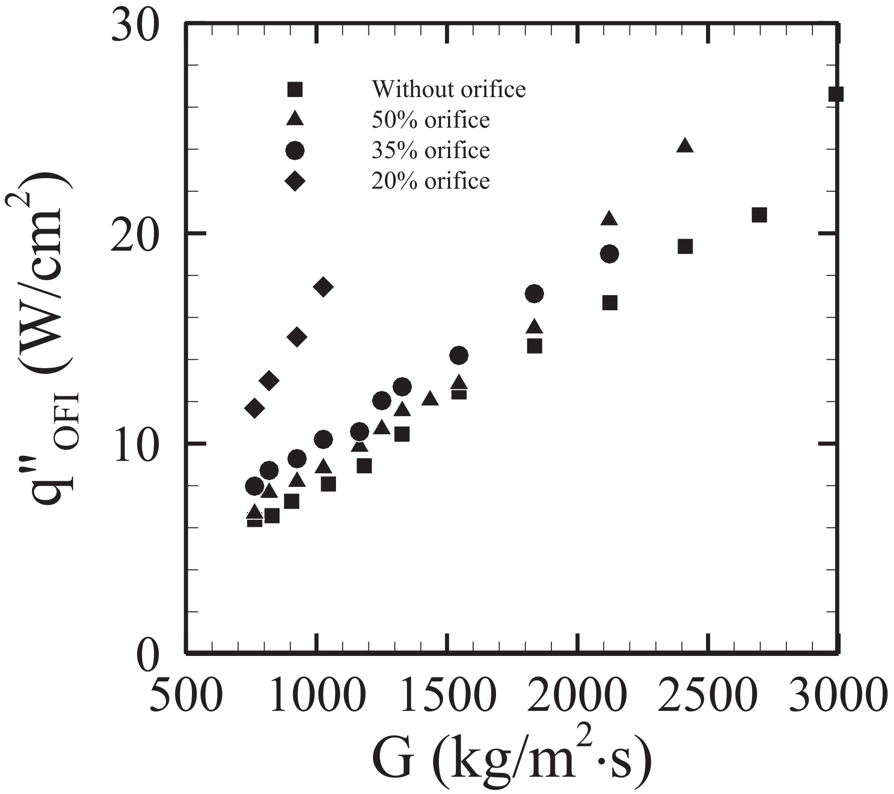

Figure 5.15: The heat flux at the onset of flow instability in the microtubes with different orifice sizes.

lower than 1000 kg/m^2·s.

Figure 5.16 shows the time-averaged pressure drop in the microtubes with different orifices at the onset of flow instability. Typically, the time-averaged pressure drop in the microtube with orifice is higher than the one in the single microtube, which is caused by an additional pressure drop in the orifice microtube. It is noted that the pressure drop increases with increasing mass flux, and then decreases suddenly. After that, the pressure drop increases again as mass flux increases. It could be explained by the oscillation type. Judging from the pressure and temperature distributions during a time span of 5 minutes, the first increasing trend observed is the LD oscillations. A large pressure drop is noted in

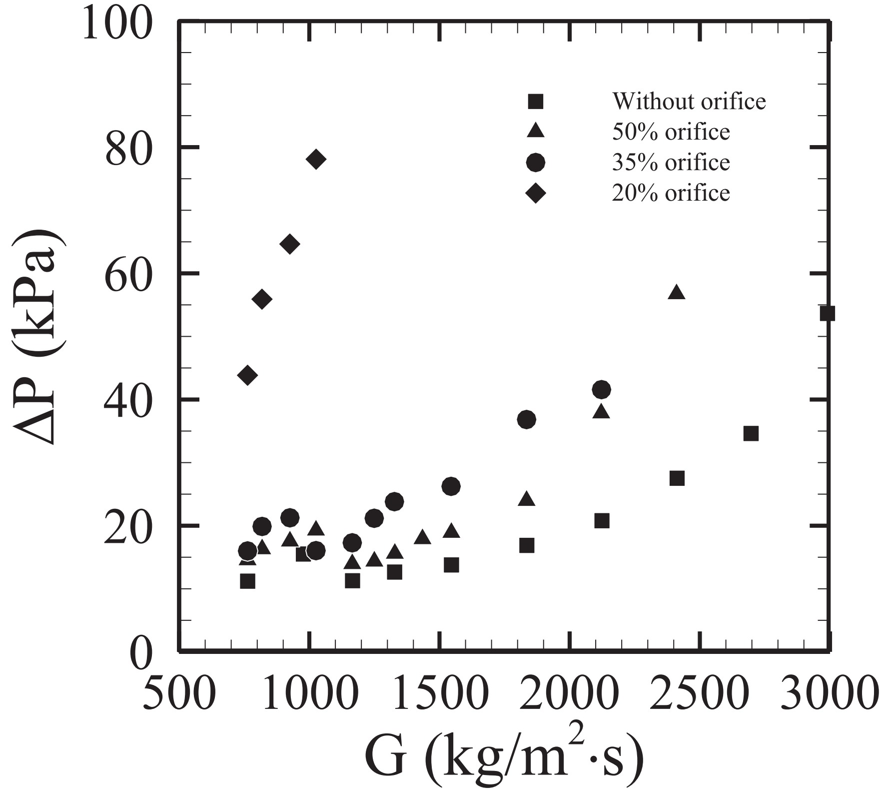

Figure 5.16: The time-averaged pressure drop at the onset of flow instability in the microtubes with different orifice sizes.

the microtube due to the Ledinegg oscillation. As the mass flux increases, the LDP oscillation occurs and the pressure drop increases as the Ledinegg oscillation remains dominant. The pressure drop decreases once the mass flux has reached a certain value since the dominant oscillation changes from static to dynamic. Ledinegg oscillation becomes secondary or disappears. Further increase in mass flux causes increased pressure drop.

Generally, the orifice is capable of stabilizing the flow, or delaying the flow oscillations at the same mass flux as the single microtube without orifice. An orifice area ratio that is larger than 35% does not significantly affect the onset of flow instability at low mass fluxes. However, it exhibits outstanding performance at high mass fluxes. Reducing the area ratio to 20% can dramatically increase the heat flux of the onset of flow instability at low mass fluxes; however, higher pressure drop is created. It is suggested that a large orifice area ratio can be used at high mass fluxes and a small orifice area ratio is suitable for low mass fluxes.

Chapter 6

6 Prediction of Onset of Flow Instability

Since the onset of flow instability is very close to the onset of significant void, the prediction of the onset of flow instability in the existing models from the literatures is alternated to the prediction of the onset of significant void. Some correlations have been proposed based on the saturated flow boiling heat flux at the exit of microchannel. All experiments and analytical models are developed in the channels without inlet orifice. The prediction of the onset of flow instability in single microchannel with inlet orifice is fundamental and has not been studied yet. In this chapter, a methodology to predict the onset of flow instability in single microtube with and without inlet orifice is proposed. The prediction is validated by comparing with experimental data. The effects of area ratio and saturation pressure on the onset of flow instability are studied and criterion of orifice selection is introduced at the end of this chapter.

6.1 Prediction Method

Whittle and Forgan (1967) found that the change in the slope of pressure drop against flow rate from positive to negative was always abrupt and the minimum pressure drop on the demand curve was approximately equal to the pressure drop under no-heating condition. Based on this phenomenon, a prediction concept is proposed stating that the onset of flow instability occurs as the pressure drop of single-phase liquid under no-heating condition is equal to the pressure drop of two-phase flow under heating condition at the same mass flow rate. Figure 6.1 shows the pressure drop against the heat flux at a constant mass flux. The horizontal dash line and dot dash line represent the single-phase liquid pressure drop under no heating condition for a given mass flux in the microtube with and without orifice. The solid line represents the pressure drop under heating condition in the microtube without orifice. Under heating condition, in single-phase liquid regime, the pressure drop decreases as heat flux increases since the liquid viscosity decreases as liquid temperature rises. As soon as boiling occurs (ONB), the pressure drop increases as heat flux increases due to the increased vapor quality. As the pressure drop of two-phase flow is smaller than the pressure drop of single-phase liquid under no-heating condition at mass flux of G, the system is stable. Otherwise, flow oscillation occurs. Therefore, the intersection of $\Delta P_{no\text{-}heating}$ line and the $\Delta P_{heating}$ curve at the mass flux of G is considered as the onset of flow instability.

The prediction methodology is proven by comparing the experimental data of pressure drop at OFI in the literatures (Stelling et al, 1996; Kennedy et al, 2000; Whittle and Forgan, 1967) with the calculated single-phase liquid pressure drop. The experimental data of pressure drop were obtained from the demand curve in literatures.

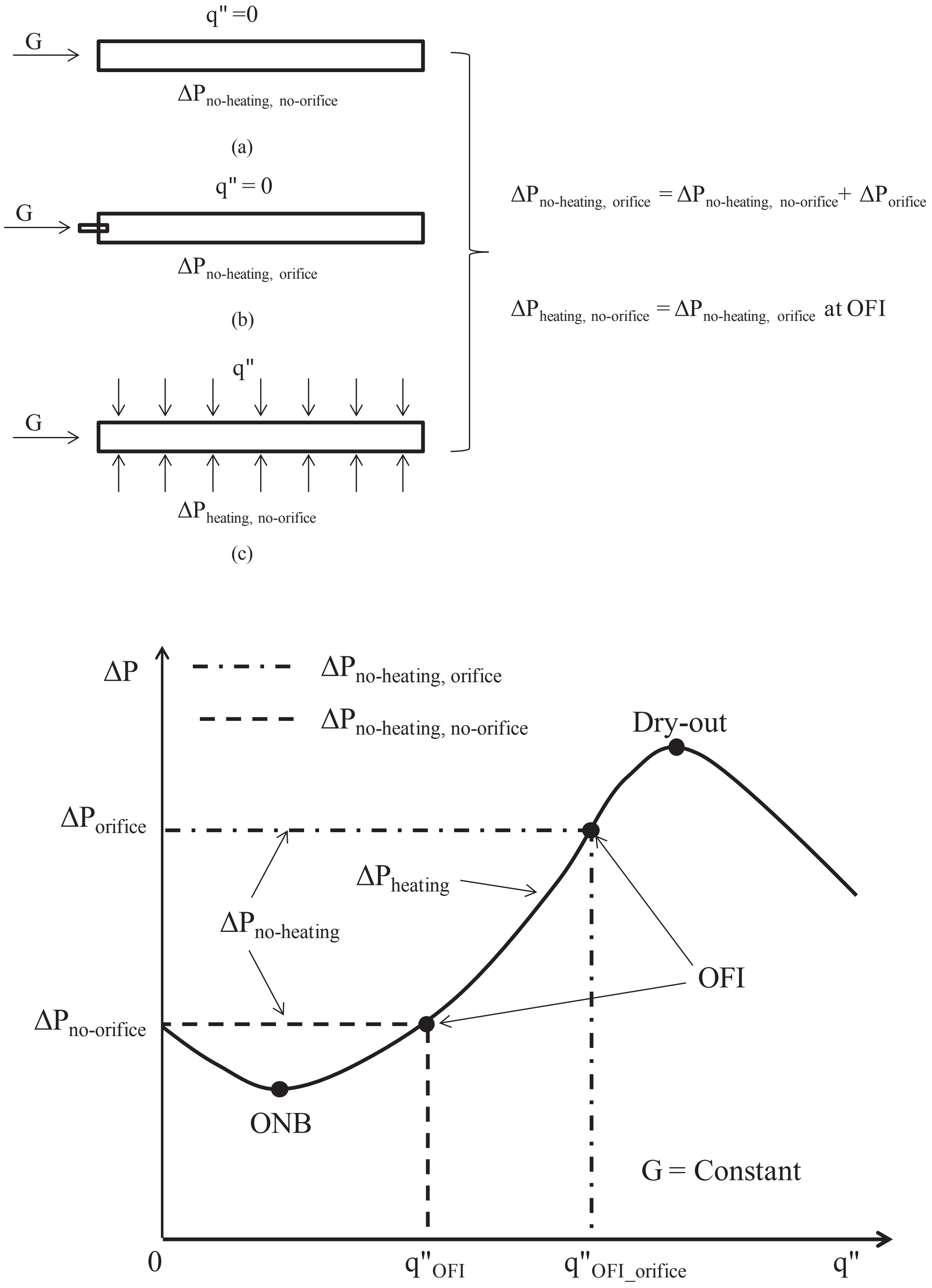

Figure 6.1: Schematic of the prediction of onset of flow instability. The horizontal dash line represents the pressure drop in (a); the horizontal dot dash line represents the pressure drop in (b); the solid line represents the pressure drop in (c).

The pressure drop in the microchannel without inlet orifice under no-heating condition is calculated using the corresponding mass flux at OFI,

$$\Delta P_{sp,unheated} = f\frac{G_{OFI}^{2} L}{2D\rho_{l}} \tag{6.1}$$

For laminar flow, the friction factor, *f*, is calculated as,

$$f_{L} = \frac{64}{Re}, Re \le 2000 \tag{6.2}$$

The turbulent flow was widely tested in the literatures. Since the inner surface roughness was usually not provided, the friction factor of turbulent flow is determined as,

$$f_{T} = \frac{0.3164}{Re^{0.25}}, Re \ge 4000 \tag{6.3}$$

Comparison of the pressure drop at OFI from the literatures and calculated pressure drop under no heating condition at G_{OFI} is shown in Figure. 6.2. It shows reasonable agreement.

6.2 Prediction Procedures

As mentioned above, the prediction of onset of flow instability in the microtube with orifice is dependent on two pressure drop predictions: the single-phase pressure drop in the microtube with orifice under no-heating condition, and two-phase pressure drop in the microtube without orifice under heating condition. Both two pressure drop predictions are independent and carried out in advance. The followings are the procedures of prediction of onset of flow instability:

1. The prediction of single-phase pressure drop in the microtube with orifice under no-

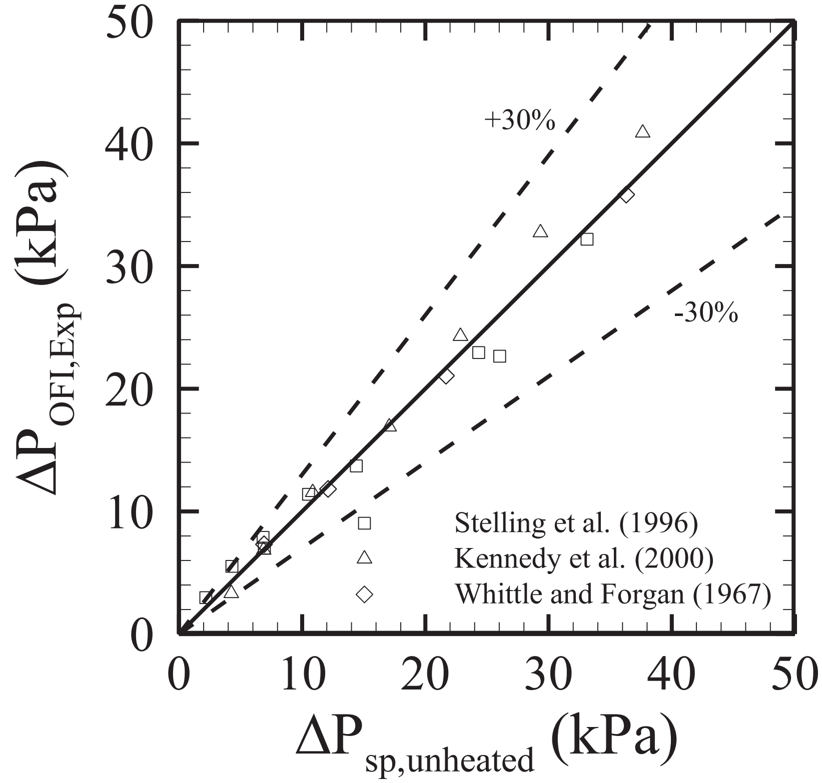

Figure 6.2: Comparisons of single-phase pressure drop under no heating condition and two-phase pressure drop under heating condition at the onset of flow instability.

heating condition: it can be viewed as the sum of two pressure drop components, the single-phase pressure drop in the main microtube and the additional pressure drop caused by inlet orifice.

2. Validation of the predication of two-phase pressure drop in the microtube without orifice under uniform heating condition: since there is no valid theoretical model to predict the two-phase pressure drop as single-phase pressure drop, the predicted two-phase pressure drop in the microtube without orifice is validated by comparing with the experimental data. In this step, a correlation of two-phase viscosity is proposed and the homogenous model is applied for the prediction of two-phase pressure drop. The mass

flux, heat flux, and the outlet pressure obtained in the experiment are used as the input data in the prediction. Figure 6.3 shows the pressure drop components in the experiment. Each pressure drop component has to be considered well in order to achieve a reasonable comparison.

3. Validation of the prediction of onset of flow instability: onset of flow instability occurs as the single-phase pressure drop under no-heating condition is equal to the two-phase pressure drop under uniform heating condition. The heat flux applied to the microtube starts from zero and increases with a small constant increment. In the current work, the increment of heat flux is set as 0.1 W/cm^2. The working fluid condition (single-phase or two-phase flow) should be determined first. At each given heat flux, the saturation

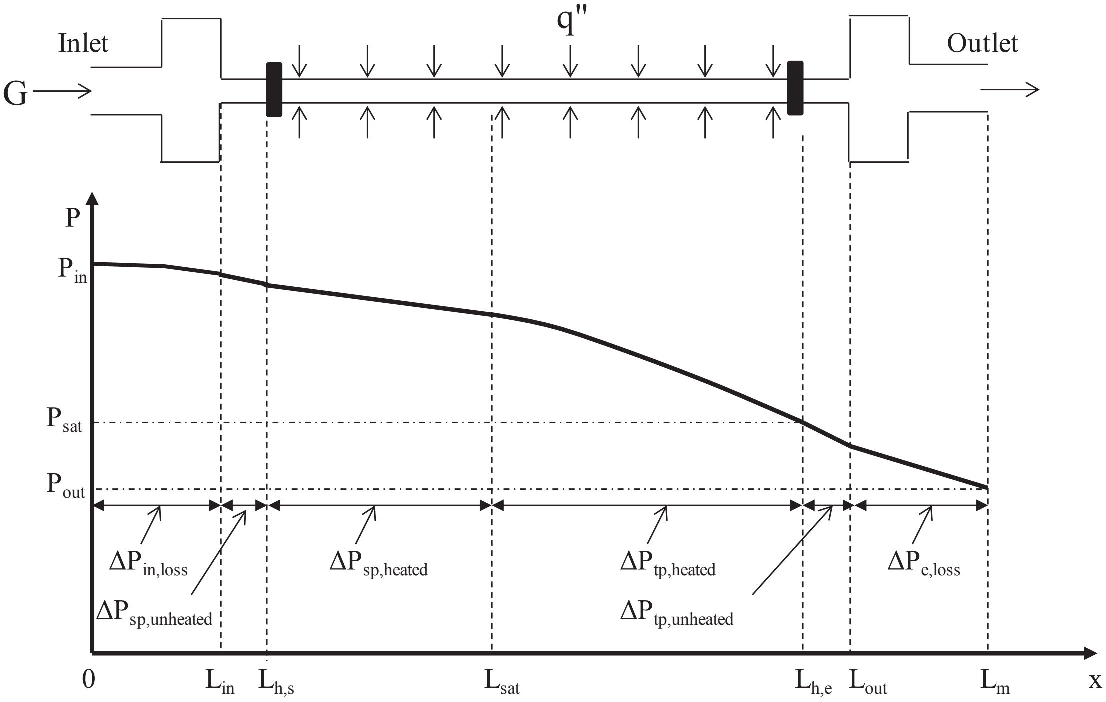

Figure 6.3: Schematic of pressure distribution between inlet and outlet measurement locations.

pressure at the exit of microtube needs to be determined since the measured outlet pressure is smaller than the saturation pressure at the exit of microtube due to the distance between the measured location and the exit of microtube. The pressure loss in the downstream support and hydraulic fittings is calculated. Then the saturation pressure at the exit of microtube is obtained. By applying the energy balance equation, enthalpy of working fluid at the exit of microtube is calculated. If the calculated enthalpy at the exit is smaller than the local saturation enthalpy, the working fluid is considered as single-phase flow. Otherwise, it is two-phase flow. Figure 6.4 shows the flow chart of prediction of onset of flow instability. It is noted that the pressure losses in the support and hydraulic fittings are excluded in the prediction of onset of flow instability.

4. Parameter study: as soon as the prediction of onset of flow instability is validated, the effects of mass flux, area ratio, and saturation pressure on the onset of flow instability are studied by applying the proposed methodology.

6.3 Prediction of Pressure Drop

6.3.1 Single-phase Pressure Drop in the Microtube with Orifice

In the current work, it is considered that the addition of an orifice only increases the upstream pressure at a given mass flux, and doesn't influence the two-phase flow, such as flow pattern and pressure drop. The additional pressure drop caused by orifice contains three components: contraction at the inlet of orifice, frictional pressure drop inside the orifice tube, and the expansion at the outlet of orifice:

$$\Delta P_{orifice} = \Delta P_{con} + \Delta P_{fr\_orifice} + \Delta P_{exp} \tag{6.4}$$

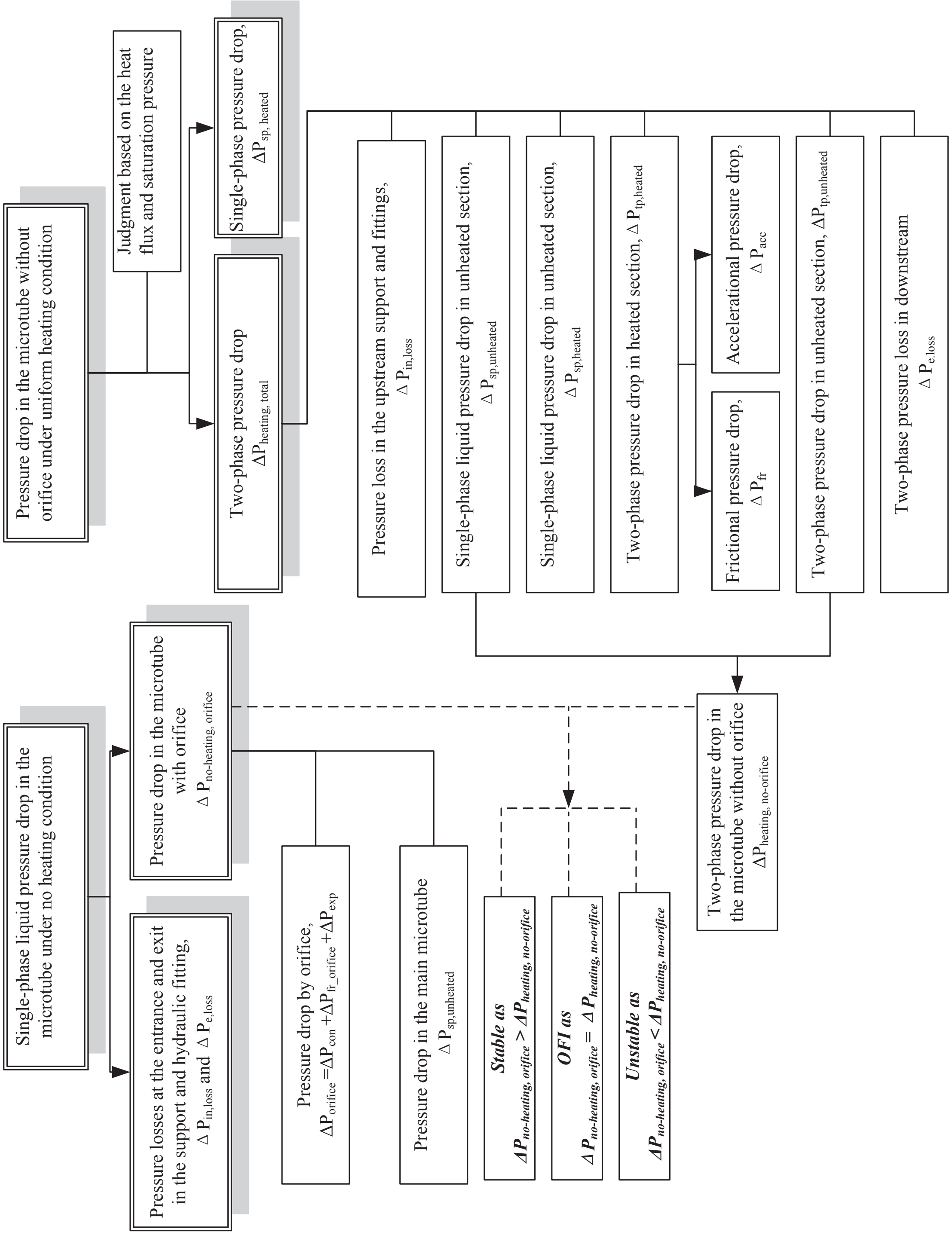

Figure 6.4: Flow chart indicating the prediction procedures of onset of flow instability.

The contraction and expansion coefficients are obtained from Munson et al. (2009). Hence, the pressure drop in the microtube with orifice under no heating condition can be determined as,

$$\Delta P_{no-heating,orifice} = \Delta P_{sp,unheated} + \Delta P_{orifice} \tag{6.5}$$

where, $\Delta P_{sp,unheated}$ is the single-phase liquid pressure drop in the main microtube under no-heating condition. It is calculated using Equation 6.1. The heat flux at OFI is increased by the addition of inlet orifice which causes higher pressure drop under no-heating condition, as shown in Figure 6.1 (dash dot line).

6.3.2 Two-phase Pressure Drop in the Microtube without Orifice

In order to determine q''_{OFI} at a given mass flux, the pressure drop curve in a uniformly heated microtube under steady state flow condition need to be obtained. The prediction of pressure drop is developed and validated by comparing with experimental data. The flow regimes can be classified into single-phase liquid and two-phase mixture. The pressure drop components in the microtube are presented in Figure 6.3. The total pressure drop is calculated as,

$$\Delta P_{heating,total} = \Delta P_{in,loss} + \Delta P_{sp,unheated} + \Delta P_{sp,heated} + \Delta P_{tp,heated} + \Delta P_{tp,unheated} + \Delta P_{e,loss} \tag{6.6}$$

At the entrance of microtube is only subcooled liquid. The upstream pressure loss $\Delta P_{in,loss}$ between the measured location and entrance of microtube has been determined (refer to Section 3.4.1). The friction factor can be calculated using Equations 6.2-6.3 for laminar and turbulent flow. In the transitional flow regime, there exists no proper friction factor correlation since it is dependent on the experimental facility. In the experiment, the transitional flow approximately starts at *Re* = 2000. The friction factor increases as *Reynolds number* increases, as shown in Figure 3.3. In order to predict the pressure drop in transitional flow, the friction factor is assumed a linear function of *Reynolds number*,

$$\begin{aligned} f_{TR} &= \frac{f_T(Re=4000)-f_L(Re=2000)}{2000}(Re-2000)+f_L(Re=2000) \\ &= 3.9\times10^{-6}\,Re+0.0242 \qquad\qquad 2000<Re<4000 \end{aligned} \tag{6.7}$$

The working fluid properties at the inlet temperature are used to calculate the pressure drop in the unheated section. The local properties are used to obtain the pressure drop in the heated section. The single-phase pressure drop in unheated and heated sections $\Delta P_{sp,unheated,}$ and $\Delta P_{sp,heated,}$ are calculated as,

$$\Delta P_{sp,unheated} = f\,\frac{G^2\left[L_{h,s}-L_{in}\right]}{2D_m\rho_{l,in}} \tag{6.8}$$

$$\Delta P_{sp,heated} = \int_{L_{h,s}}^{L_{sat}} f(x)\frac{G^2}{2D_m\rho_l(x)}dx \tag{6.9}$$

Thermal capacity is a function of temperature. The length of single-phase liquid regime is determined by the energy balance,

$$L_{sp} = L_{sat}-L_{h,s} = \frac{GA\left[C_{P,T_{sat}}\cdot T_{sat}-C_{P,T_{in}}\cdot T_{in}\right]}{q''\pi D_m} \tag{6.10}$$

Since the liquid properties of FC-72 are function of temperature, the curve fitting is performed based on the data from 3M Company and the equations used to calculate the properties are shown below:

$$\rho(x) = 1740 - 2.61T(x) \tag{6.11}$$

$$\mu(x) = \rho(x)\left(B\text{-}e^{A}\right) \tag{6.12}$$

where
$$A = -0.4787 - 3.295B + 0.6119B^2 - 0.3193B^3 \tag{6.13}$$

$$B = 10^{C} - 0.7 \tag{6.14}$$

$$C = 10^{11.93336 - 5.27691 og_{10}[T(x)+273]} \tag{6.15}$$

The homogenous model and separated model are commonly used to predict the two-phase flow pressure drop. The separated model usually requires the vapor viscosity of working fluid. Since the vapor viscosity of FC-72 is lack, the homogenous model is applied to predict the two-phase pressure drop in the present study. The two-phase pressure loss by contraction and expansion in downstream support and hydraulic fittings is calculated using the correlations proposed by Coleman (2004).

Contraction:
$$\Delta P_{tp,con} = \frac{G^2}{2\rho_l}\left[\left(\frac{1}{C_o} - 1\right)^2 + 1 - \frac{1}{\beta_{con}^2}\right]\Psi_h \tag{6.16}$$

Where
$$C_o = \frac{1}{0.639\left(1 - \frac{1}{\beta_{con}}\right)^{0.5} + 1} \tag{6.17}$$

$$\Psi_h = \left[1 + \chi_e\left(\frac{\rho_l}{\rho_v} - 1\right)\right];\ \beta_{con} > 1 \tag{6.18}$$

Expansion:
$$\Delta P_{tp,exp} = G^2\beta_{exp}\left(1 - \beta_{exp}\right)\frac{\Psi_s}{\rho_l} \tag{6.19}$$

where $$\Psi_s = 1 + \left(\frac{\rho_l}{\rho_v} - 1\right)\left(0.25\chi_e(1-\chi_e) + \chi_e^2\right);\ \beta_{exp} < 1 \tag{6.20}$$

The two-phase pressure drop at the exit section by contraction and expansion is calculate as,

$$\Delta P_{e,loss} = \Delta P_{tp,con} + \Delta P_{tp,exp} + \Delta P_{tp,i} \tag{6.21}$$

The two-phase pressure drop is dependent on the vapor quality, which is calculated using energy balance equation. The local saturation pressure, which is used to determine the local saturated temperature and two-phase flow properties, needs to be obtained. Since the pressure loss between the exit of the microtube and the measurement location of outlet pressure is significant, the actual microtube exit pressure is higher than the measured value. In addition, the vapor quality in the two-phase unheated section is constant. In order to calculate the vapor quality at the end of heated section $L_{h,e}$, the local pressure, P_{sat}, shown in Figure 6.3, should be obtained.

The saturation pressure, P_{sat}, is iteratively solved. First, P_{sat} is set as P_{out}. The vapor quality, saturated temperature, and heat of evaporation at $x = L_{h,e}$ are determined using P_{sat}. As soon as the vapor quality is known, the pressure drop between $L_{h,e}$ and L_m can be obtained. The new saturation pressure is determined by,

$$P'_{sat} = \Delta P_{e,loss} + \Delta P_{tp,unheated} + P_{out} \tag{6.22}$$

If the difference between P_{sat} and P'_{sat} is beyond 1kPa, the saturation pressure is set as,

$$P_{sat} = \frac{P'_{sat} + P_{out}}{2} \tag{6.23}$$

The iteration is carried out until the saturation pressure is found. Then, the corresponding vapor quality and saturated temperature are obtained. The two-phase pressure drop is composed of frictional and accelerational components,

$$\Delta P_{tp} = \Delta P_{fr} + \Delta P_{acc} \tag{6.24}$$

The accelerational pressure drop is calculated as,

$$dP_{acc} = G^2 \left\{ \left[\frac{(1-\chi)^2}{\rho_l \cdot (1-\alpha)} + \frac{\chi^2}{\rho_v \cdot \alpha} \right] - \left[\frac{(1-\chi_u)^2}{\rho_l \cdot (1-\alpha_u)} + \frac{\chi_u{}^2}{\rho_v \cdot \alpha_u} \right] \right\} \tag{6.25}$$

where,

$$\chi = \frac{q'' \pi D (x - L_{sp})}{G A h_{fg}} \tag{6.26}$$

$$\chi_u = \frac{q'' \pi D (x - dx - L_{sp})}{G A h_{fg}}, \ L_{sat} \le x \le L_{h,e} \tag{6.27}$$

$$\alpha = \frac{\rho_l - \rho_v}{1/\chi + (\rho_l / \rho_v - 1)} \tag{6.28}$$

$$\alpha_u = \frac{\rho_l - \rho_v}{1/\chi_u + (\rho_l / \rho_v - 1)} \tag{6.29}$$

The frictional pressure drop is determined using the homogenous model and is calculated as,

$$dP_{fr} = f_{tp} \frac{G^2}{2 \rho_{tp} D_m} dx \tag{6.30}$$

The two-phase flow *Reynolds number* and density are calculated by Equation 2.5-2.6. The friction factor of two-phase flow is calculated using Equation 6.2, 6.3, and 6.7 for different types of flow. Three existing models for two-phase flow viscosity without using vapor viscosity are selected,

Owens (1961)
$$\mu_{tp} = \mu_l \tag{6.31}$$

Garcia et al. (2003)
$$\mu_{tp} = \mu_l \frac{\rho_{tp}}{\rho_l} \tag{6.32}$$

Davidson et al. (1943)
$$\mu_{tp} = \mu_l \left(1 + \chi_e \frac{\rho_l - \rho_v}{\rho_v} \right) \tag{6.33}$$

Figure 6.5 shows the two-phase pressure drop comparisons of experimental data with homogenous models. Davidson et al.'s model over predicts the two-phase pressure drop at $G \leq 300$ kg/m^2·s and under predicts the two-phase pressure drop at $G > 450$ kg/m^2·s. Owens and Garcia et al.'s models under predict the two-phase pressure drop since they considered two-phase flow viscosity equal or less than liquid viscosity. Based on the current experimental data, a new correlation of two-phase flow viscosity is developed,

$$\mu_{tp} = 0.01 \cdot \mu_l \cdot \left[(0.0051G - 0.1127)(1-\chi)^{0.3} + \left(\chi \frac{\rho_l}{\rho_v} \right)^{-0.5} \right] \tag{6.34}$$

The pressure drop in the microtube under heating condition is the sum of single-phase and two-phase pressure drops,

$$\Delta P_{heating,no-orifice} = \Delta P_{sp,unheated} + \Delta P_{sp,heated} + \Delta P_{tp,heated} + \Delta P_{tp,unheated} \tag{6.35}$$

The working fluid saturated properties are determined by the local pressure, which is calculated backwards from outlet to inlet.

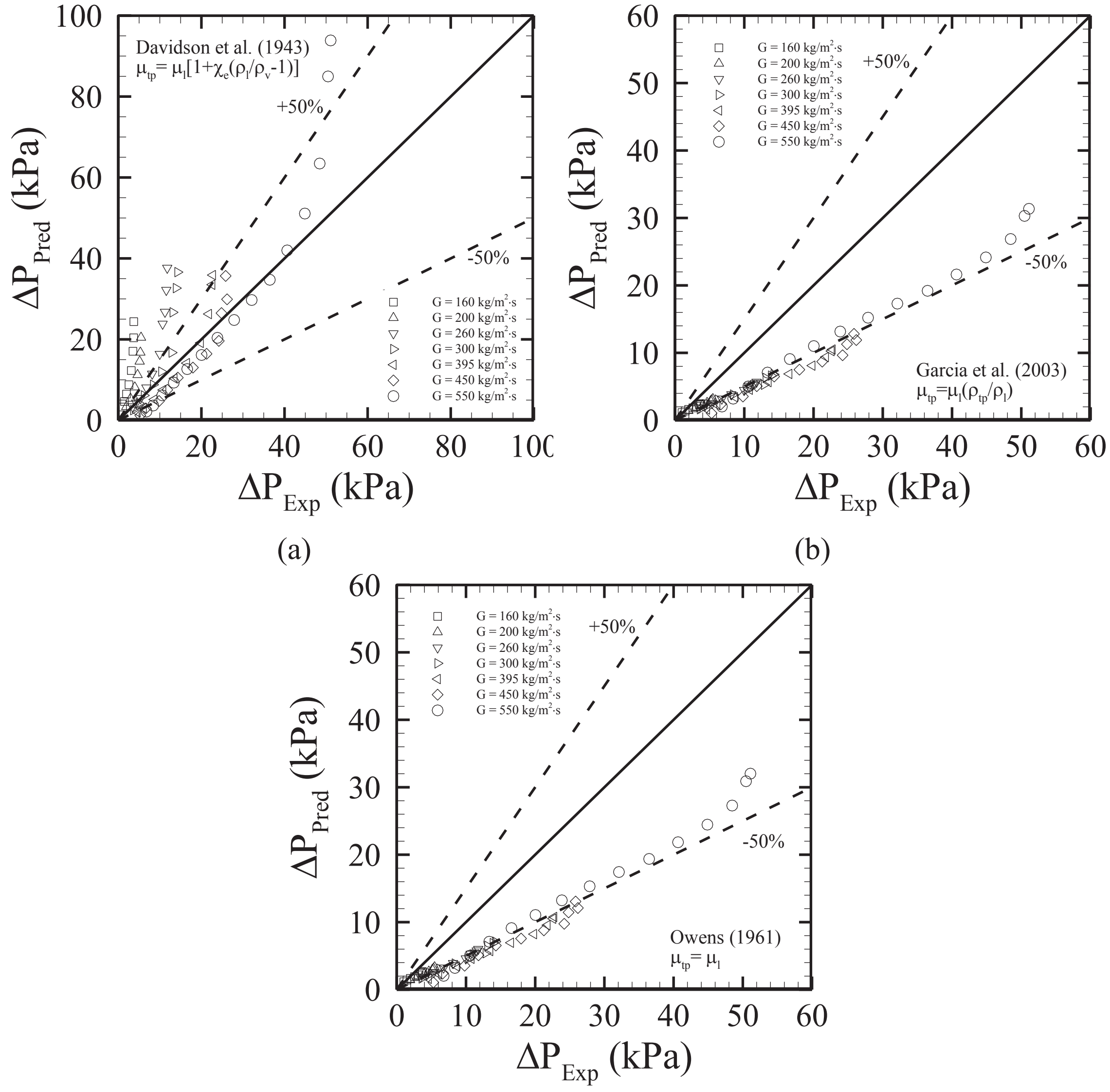

(a)

(b)

(c)

Figure 6.5: Comparisons of two-phase pressure drop between experiment and existing models.

6.4 Validations of Predictions

6.4.1 Validation of Pressure Drop Prediction

Since the prediction of onset of flow instability is dependent on the prediction of pressure drop, the validation of pressure drop prediction is first carried out by comparing with experimental data. The main microtube has a hydraulic diameter of 0.889 mm and a length of 150 mm in the experiment. The measured pressure drop includes pressure loss upstream and downstream between the measured locations and entrance/exit of microtube, $\Delta P_{in,loss}$, and $\Delta P_{e,loss}$. For proper comparison, the pressure loss is subtracted from the measured value. Figure 6.6 shows the pressure drop against heat flux at four mass fluxes. The comparisons of pressure drop in both single-phase and two-phase flow regimes show good agreement. The mean absolute error is calculated using Equation 4.1. The partial dry-out and subcooled flow boiling are excluded from database since the present prediction of pressure drop is only suitable for the saturated flow boiling. The mean absolute error is 5.3%, and the deviation is within 20% from the experiment, as shown in Figure 6.7.

6.4.2 Validation of Onset of Flow Instability

Figure 6.8 compares the onset of flow instability obtained from the experiment with the prediction in the microtubes with four inlet orifices. In the experiment, an orifice tube is assembled at the inlet to achieve the inlet restriction configuration. The inlet temperature is maintained at 24 °C. The mass flux varies from 760 to 3000 kg/m^2·s. The details of experiment could be found in Section 5.1. Generally, the present methodology

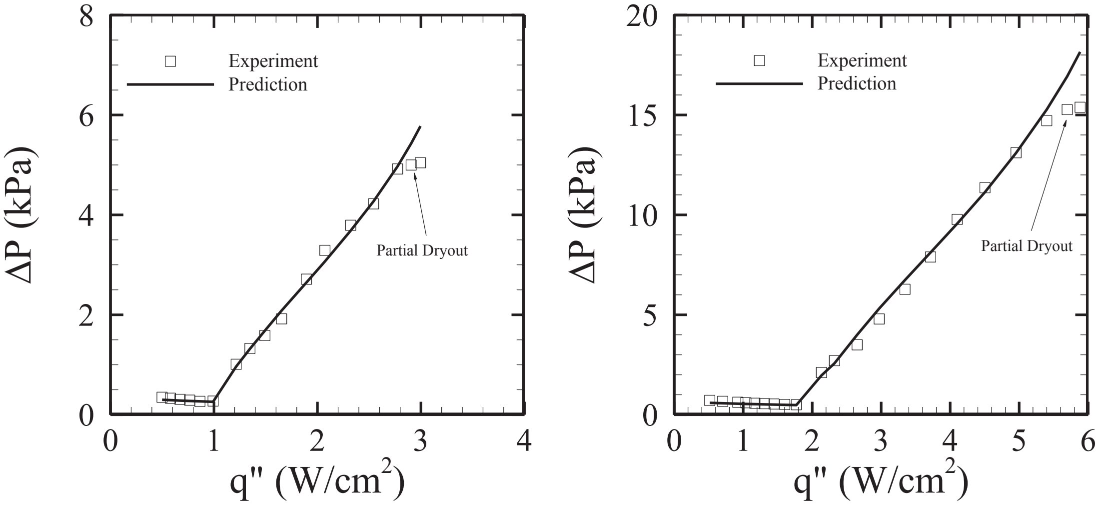

(a) G = 160 kg/m^2·s (b) G = 295 kg/m^2·s

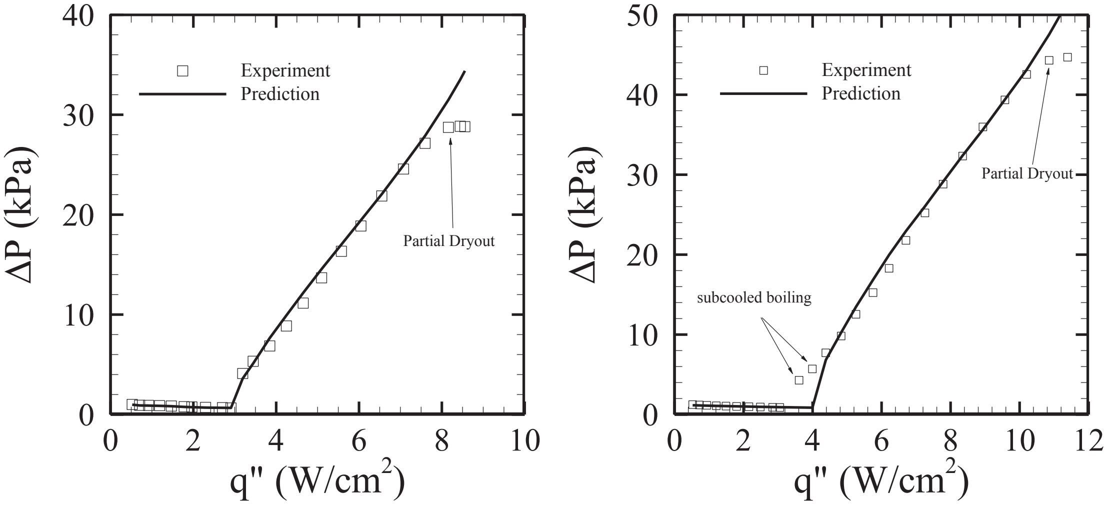

(c) G = 420 kg/m^2·s (d) G = 550 kg/m^2·s

Figure 6.6: Single-phase and two-phase pressure drop in the microtube at four mass fluxes.

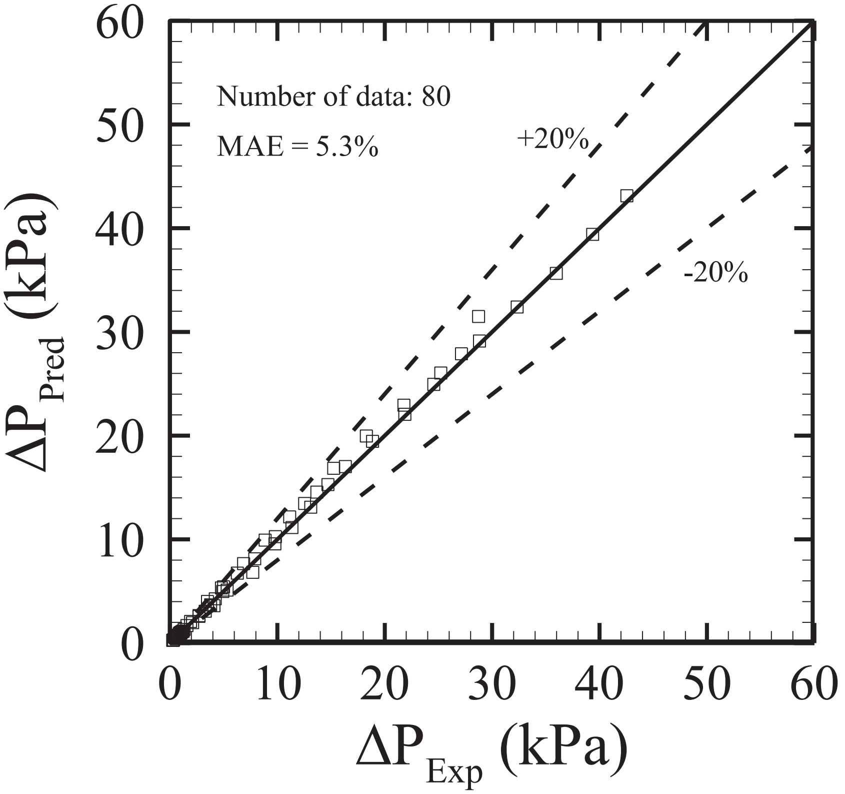

Figure 6.7: Comparisons of pressure drop between the prediction and experiment at four mass fluxes.

under predicts the onset of flow instability. In the microtube without inlet orifice, the prediction shows good agreement with the experiment at $G \leq 2200$ kg/m^2·s. However, at $G > 2200$ kg/m^2·s, the methodology under predicts the onset of flow instability. A similar trend is also observed in the microtube with 50% area ratio. It is considered that the underestimation is attributed to the correlation of two-phase flow viscosity. The correlation is developed based on the experimental data at $G \leq 550$ kg/m^2·s. The accuracy at high mass fluxes cannot be proven based on the current experimental facility since a large pressure drop is created at high mass fluxes. The system cannot be stabilized due to the limited pumping power. In the microtubes with 35% and 20% orifices, the predicted

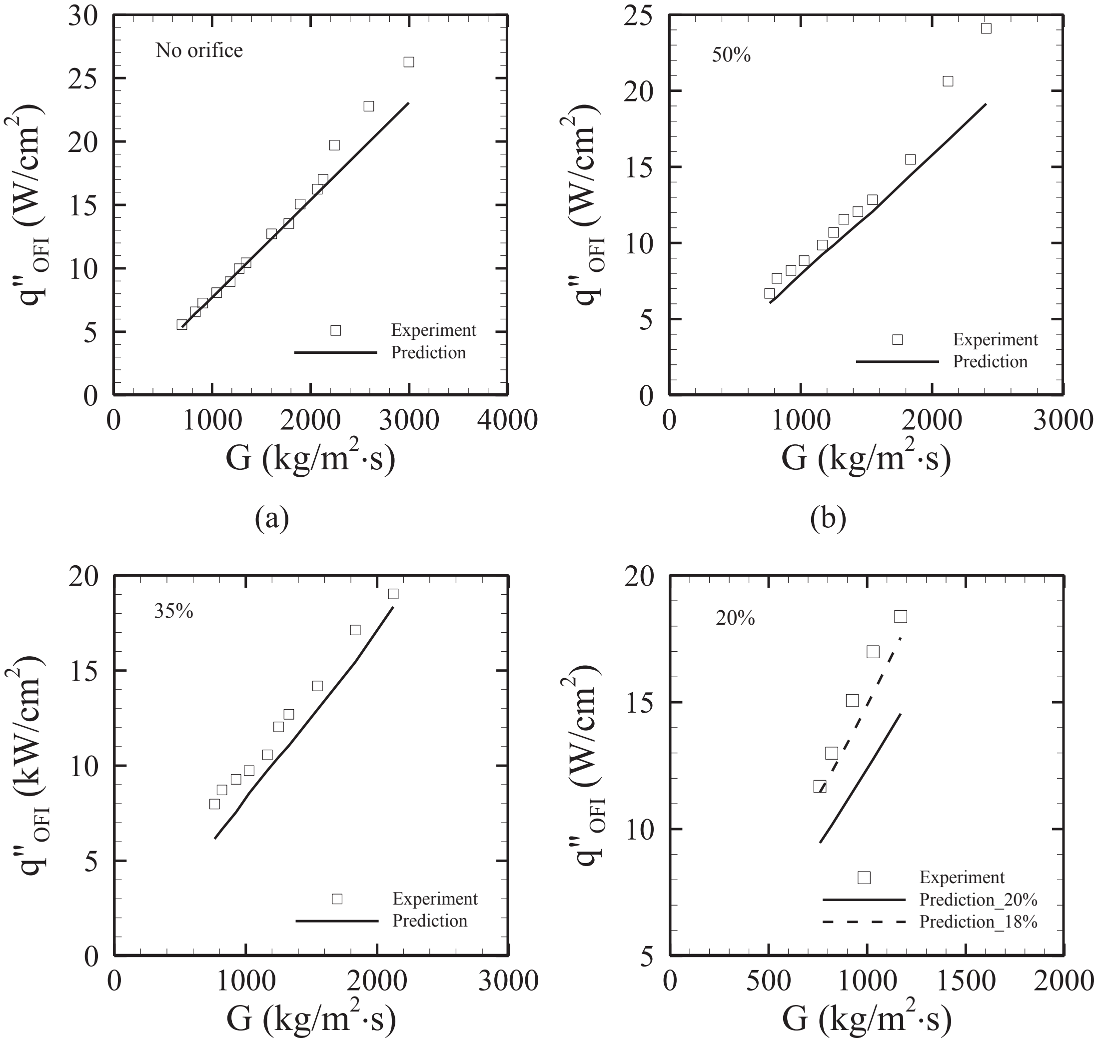

(a) (b)

(c) (d)

Figure 6.8: The predicted and measured onset of flow instability in the microtubes with and without orifices.

onset of flow instability is smaller than the measured values in the entire range of measurement, especially in the 20% orifice microtube. Since the maximum mass flux in the microtubes with 35% and 20% orifices is smaller than 2200 kg/m^2·s, the under-estimation of onset of flow instability is not caused by correlation of two-phase viscosity. The possibility causing the under prediction is the uncertainty of area ratio, as shown in

Table 3.1. The effect of area ratio uncertainty is significant in the small orifice microtube. Figure 6.8d shows the comparison of onset of flow instability between prediction and experiment in the microtube with 20% orifice. The predicted result using 18% area ratio is also present in this figure. It shows that the small change of area ratio can cause a significant increase of onset of flow instability. The comparison shows that the deviation and the mean absolute error between experiment and prediction are within 30% and 13%, respectively, as shown in Figure 6.9.

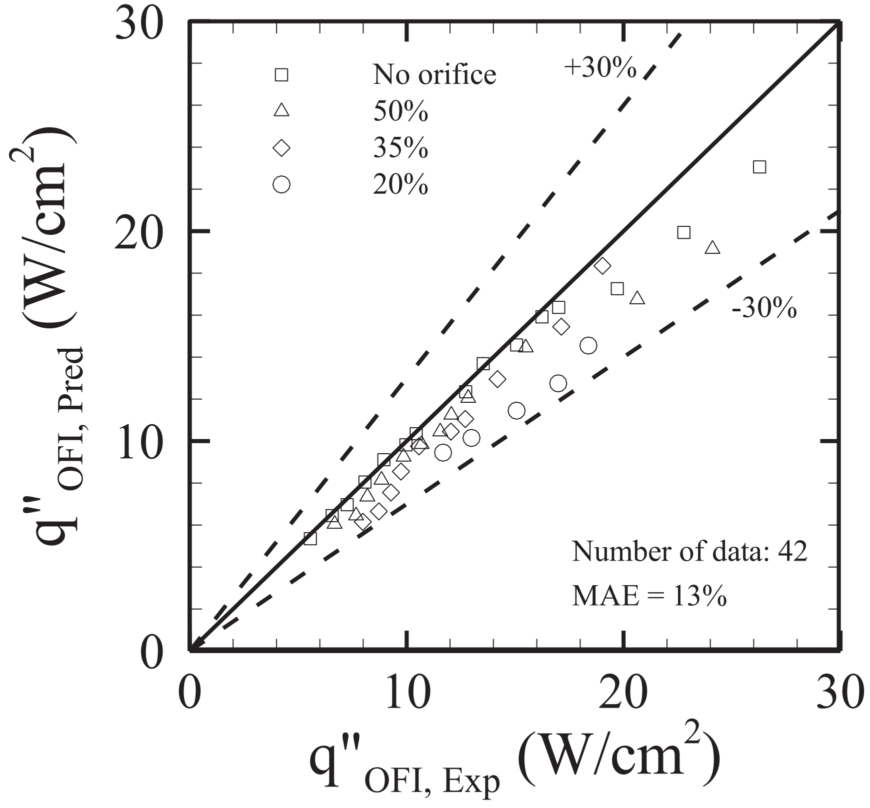

Figure 6.9: Comparison of the onset of flow instability between the experiment and prediction.

6.5 Study of Parameters

6.5.1 Effect of Area Ratio

The proposed method can reasonably predict the onset of flow instability in the microtube with hydraulic diameter of 0.889 mm at $G \leq 2200$ kg/m^2·s. The effect of area ratio on the onset of flow instability is studied within the valid range. The exit gage pressure and inlet temperature are set as 0 kPa and 24°C. Figure 6.10 shows the onset of flow instability in the microtube with various area ratios at four mass fluxes. The symbol "IEC" represents the flow instability eliminated completely. At $G = 100$ kg/m^2·s, the effect of inlet orifice can be neglected as the area ratio is smaller than 30% since the increased upstream pressure by inlet orifice is not sufficient to block the reversed flow. The flow instability is eliminated completely at $AR \leq 23\%$. The effect of area ratio becomes significant at high mass fluxes and small area ratios since the inlet orifice creates a considerable pressure drop. As the mass flux increases to 2000 kg/m^2·s, the area ratio smaller than 13% is able to eliminate the flow instability.

6.5.2 Effect of Saturation Pressure

Figure 6.11 shows the pressure drop for a mass flux of 500 kg/m^2·s under two saturation pressures in the microtube with 20% orifice. The effect of pressure on the single-phase pressure drop is negligible. The increase of saturation pressure is able to delay the onset of flow boiling since the saturation temperature is increased. In two-phase flow regime, the pressure drop at $P_{sat} = 200$ kPa is lower than one at $P_{sat} = 100$ kPa at the same heat flux. The same conclusion has also been reported by Kennedy et al. (2000), Roach et al.

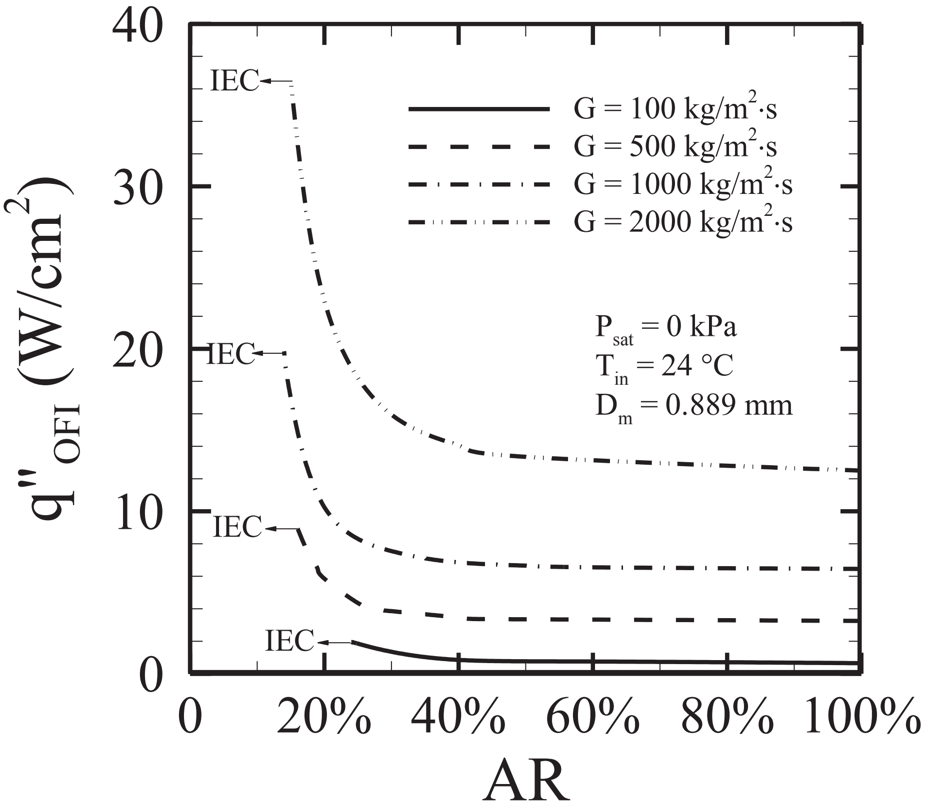

Figure 6.10: Effect of area ratio on the onset of flow instability.

(1999), and Stoddard et al. (2002). They found that mass flux at OFI decreased as the saturation pressure increased for the same inlet temperature and surface heat flux. It indicates that the OFI heat flux increases as saturation pressure increases for a given mass flux. Therefore, the heat flux required to obtain the same pressure drop at high saturation pressure is higher than one at low saturation pressure, which leads to the increase of the onset of flow instability with increasing saturation pressure.

Figure 6.12 shows the effect of saturation pressure on the onset of flow instability at two mass fluxes. It is noted that the difference of onset of flow instability at two mass fluxes, $\Delta q''_{OFI}$ increases as saturation pressure increases. It indicates that the effect of mass flux on OFI at high saturation pressure becomes more significant. Also, the effect of

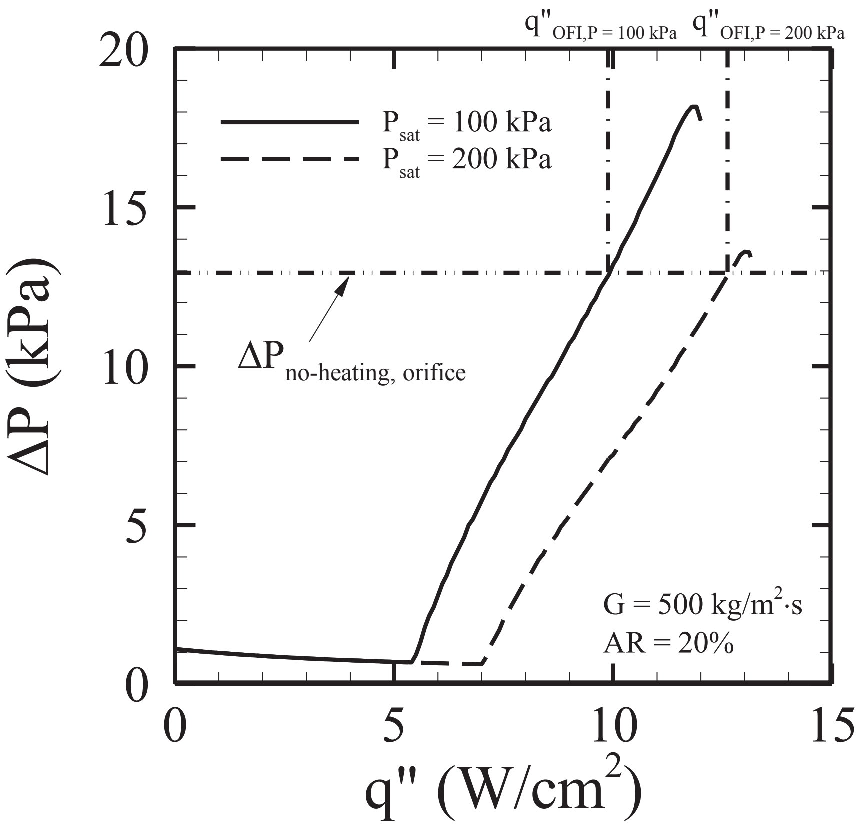

Figure 6.11: Pressure drop at G = 500 kg/m^2·s under two saturation pressures.

saturation pressure on OFI degrades as saturation pressure increases since the slope of onset of flow instability to saturation pressure decreases. At AR = 20%, the flow instability is eliminated completely as saturation pressure increases to 230 kPa at G = 500 kg/m^2·s and 540 kPa at G = 1000 kg/m^2·s, respectively. Therefore, at a certain area ratio, the increase of saturation pressure is also able to eliminate the flow instability.

6.5.3 Selection of Orifice Size

The critical heat flux is the limitation of flow boiling heat transfer in applications where the cooling system malfunctions. In the experimental work, it is found that the addition of an orifice is not able to increase the critical heat flux in single microtube. In

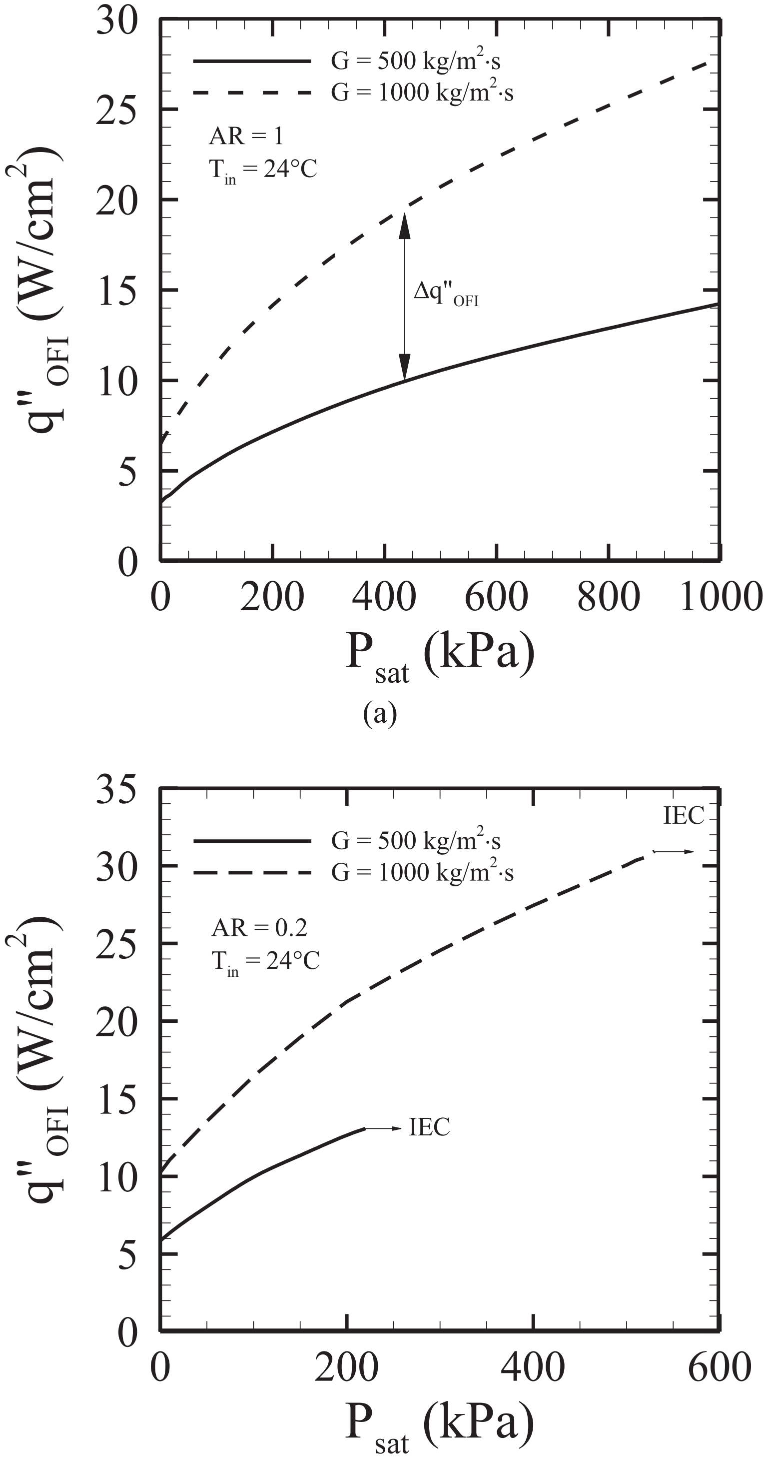

(a)

(b)

Figure 6.12: Effect of saturation pressure on the onset of flow instability.

microchannels, the flow oscillation caused by flow boiling always happens before the critical heat flux. The selection of orifice size follows the guide that the heat flux at OFI is no less than critical heat flux. As the hydraulic diameter is fixed, the criterion of orifice selection is described as,

$$q''_{OFI} \geq q''_{CHF} \tag{6.36}$$

It represents that the flow oscillation does not occur before the local burnout. The critical orifice size, which is determined as the heat flux at OFI is equal to the critical heat flux, can be solved. Any of orifice size smaller than critical orifice size is also able to eliminate the flow oscillation. In order to reduce the pumping power, the orifice size is selected as,

$$q''_{OFI}\left(AR_c\right) > q''_{CHF} > q''_{OFI}\left(AR_c - 1\%\right) \tag{6.37}$$

where, AR_c is the critical area ratio of inlet orifice. Figure 6.13 shows the selected area ratio at mass fluxes ranging from 100 to 2000 kg/m^2·s. The resolution of area ratio is 1%. It shows that the selected area ratio decreases as mass flux increases at $G \leq 700$ kg/m^2·s. At $700 \leq G \leq 1500$ kg/m^2·s, the selected area ratio maintains constant, 15%. As mass flux increases further, the selected area ratio increases.

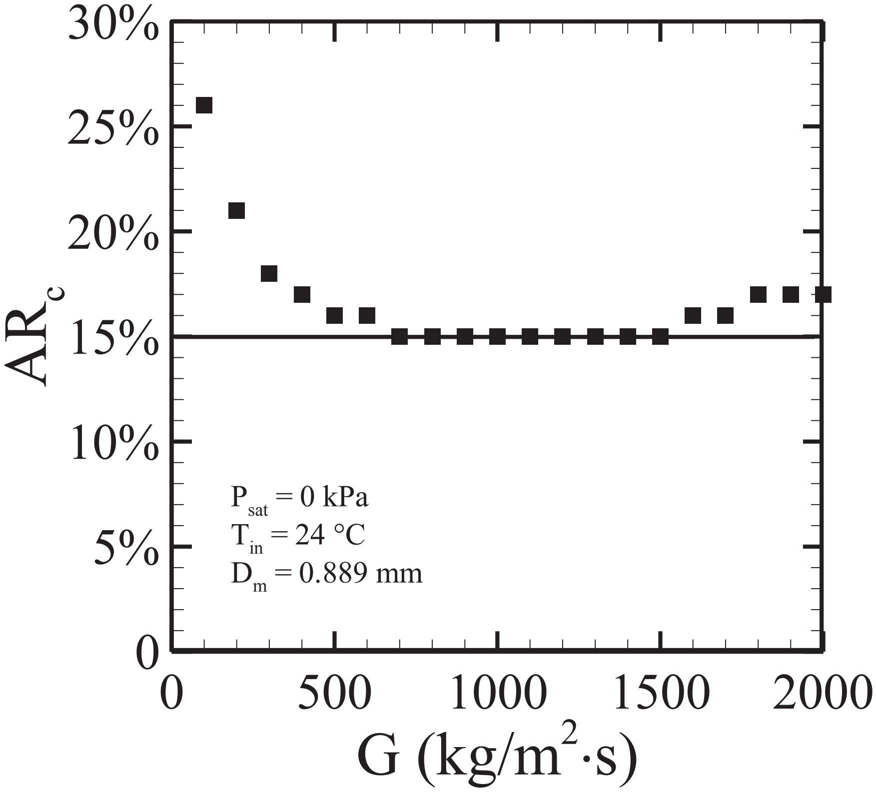

Figure 6.13: Critical area ratio at mass fluxes from 100 to 2000 kg/m^2·s.

Chapter 7

7 Closing

7.1 Conclusions and Contributions

In this work, the effects of inlet orifice on flow boiling heat transfer and flow instability in single horizontal stainless steel microtube with an inner diameter of 889 μm were experimentally investigated under uniform heating condition. Three different orifices, inlet area ratios of 20%, 35%, and 50%, respectively, were selected and tested at mass fluxes ranging from 700 - 3000 kg/m^2·s and heat fluxes varying from 6 - 27 W/cm^2. The results showed that the considerable increase in pressure drop at low mass fluxes was observed to be due to the inlet orifice. The ratio of pressure drop from the inlet orifice to the total pressure drop was reduced by increasing the mass flux, or vapor quality, which consequently increased the pressure drop along the microtube.

Two types of critical heat fluxes (CHF) were observed, normal CHF and premature CHF. The orifice did not enhance the normal CHF but increased premature CHF with decreasing the area ratio. From the point of view of heat transfer, two trends of heat transfer coefficient with vapor quality were observed. At G = 160 kg/m^2·s, the heat transfer coefficient decreased as vapor quality increased because nucleate boiling was predominant over the range of vapor quality. This tendency was caused by the suppression of bubble nucleation within a limited space. At $G > 160$ kg/m^2·s, the dominant heat transfer mechanism transitioned from nucleate boiling to forced convective boiling, and the heat transfer coefficient increased with saturation pressure. A new correlation of the heat transfer coefficient was developed with a mean absolute error of 32.7%. The effect of the inlet orifice on the flow boiling heat transfer coefficient was observed in the nucleate boiling region. However, the effect of the inlet orifice was negligible in the forced convective boiling region.

The inlet orifice was proven be efficient at stabilizing the flow during boiling. In the absence of an orifice at the inlet, four oscillation types, a combination of Ledinegg and density-wave oscillation, a combination of Ledinegg, density-wave, and pressure-drop oscillation, pressure-drop oscillation, and transition between pressure-drop and density-wave oscillation, were observed at the onset of flow instability. The high oscillation frequency and amplitude were caused by the component of density-wave and pressure-drop oscillations, respectively. The heat fluxes at the onset of flow instability in the microtubes with different orifices were measured in the tested range. Microtubes with orifices of 50% and 35% area ratios stabilized the flow at mass fluxes higher than 2000 kg/m^2·s, and the heat flux at the onset of flow instability was much larger than that of the microtube without inlet orifice. No significant change in performance was observed at lower mass flux. The orifice with a 20% area ratio had a better performance at low mass fluxes (< 1000 kg/m^2·s). It was concluded that, reducing the area ratio increased the heat flux at the onset of flow instability. Considering the pressure drop, an orifice with a large area ratio is recommended at high mass fluxes and an orifice with a small area ratio is more suitable for lower mass fluxes. Implementing an orifice in the design of microchannel heat sink has the potential to stabilize the flow without addition an active flow control**.**

In order to scientifically apply the orifice structure in the future design of microchannel heat sinks, the selection of an appropriate orifice size was introduced in order to eliminate the flow oscillation completely before local dry-out. A methodology to predict the onset of flow instability in single microtube was proposed. The prediction methodology considered the flow instability was initiated as the pressure drop in the microchannel under heating condition was higher than the pressure drop under no heating condition at a given mass flux. Since the prediction of OFI was dependent on the prediction of two-phase pressure drop in the heated microchannel, a correlation of two-phase flow viscosity using a homogenous mixture model was proposed. The comparison of two-phase pressure drop with experimental data showed a good agreement, with a mean absolute error of 5.3%. The prediction methodology was validated through comparisons with the single microtube experimental data with and without an inlet orifice. It showed reasonable agreement with a maximum deviation of 30% and a mean absolute error of 13%. The effects of area ratio and saturation pressure on the OFI at mass fluxes ranging from 100 to 2000 kg/m^2·s were studied using the present prediction methodology. The results showed that decreasing area ratio and increasing the saturation pressure improved flow stability. A criterion for the selection of orifice size was proposed, which stated that the size of orifice was determined as OFI heat flux in the channel with an orifice was equal to the critical heat flux. As the hydraulic diameter was 889 μm, a 15% area ratio was able to eliminate the flow instability completely at $100 \leq G \leq 2000$ kg/m^2·s.

7.2 Future Directions

Since the present work focuses on the fundamental research, a large amount of work needs to be carried out in the future to understand the complex phenomena of flow boiling in microchannels and acquire universal correlations. The following work may be conducted:

- The effect of area ratio on flow instability has been investigated in a microtube with a constant hydraulic diameter. It is necessary to carry out the experiments of flow instability in various main tube hydraulic diameters with a constant inlet orifice size. The target of this work is to find out the effect of main tube diameter on flow instability and provide more data for prediction of the onset of flow instability.
- Since the length of main tube was quite long (L/D = 170), the effect of the inlet orifice on flow conditions far from inlet of main tube was neglected. The reduced length of the main tube may influence the performance of the inlet orifice and particularly on pressure drop, onset of flow instability, and critical heat flux.
- In many applications, the tube orientation is vertical. Many researches have carried out the experimental studies on flow instability in vertical microchannel/microtube without an inlet orifice. Investigations into the performance of an inlet orifice in a single vertical microchannel, with both upward flow and downward flow, are also needed for the fundamental research.

- Since the flow boiling heat transfer and flow instability are relevant to two-phase flow pattern, flow visualization is the most efficient way to reflect the complex boiling phenomena. Through the flow visualization, bubble generation, growth, departure, and transition among different flow patterns are clearly obtained. The flow pattern map could be generated to provide the information for the future correlation and modeling.
- The straight microchannels have been studied extensively. The curved microchannels are seldom investigated. The future work can also extend to the study of curved microchannel, such as two-phase pressure drop, critical heat flux, and flow boiling heat transfer coefficient. The difference of inlet orifice performance in single curved microchannel from straight microchannel on flow stabilization needs to be exploited and discussed.

References

Agostini, B., Thome, J. R., Fabbri, M., Michel, B., Calmi, D., and Kloter, U., 2008, "High heat flux flow boiling in silicon multi-microchannels - Part I: Heat transfer characteristics of refrigerant R236fa", International Journal of Heat and Mass Transfer, 51, pp. 5400-14.

Agostini, B., Thome, J. R., Fabbri, M., Michel, B., Calmi, D., and Kloter, U., 2008, "High heat flux flow boiling in silicon multi-microchannels - Part II: Heat transfer characteristics of refrigerant R245fa", International Journal of Heat and Mass Transfer, 51, pp. 5415-25.

Agostini, B., Thome, J. R., Fabbri, M., Michel, B., Calmi, D., and Kloter, U., 2008, "High heat flux flow boiling in silicon multi-microchannels - Part III: Saturated critical heat flux of R236fa and two-phase pressure drops", International Journal of Heat and Mass Transfer, 51, pp. 5426-42.

Ahmas, S. Y., 1970, "Axial distribution of bulk temperature and void fraction in a heated channel with inlet subcooled", J HEAT TRANS-T ASME, 92, pp. 595-609.

Ali, R., Palm, B., and Maqbool, M. H., 2011, "Flow Boiling Heat Transfer Characteristics of a Minichannel up to Dryout Condition", J HEAT TRAN-T ASME, 133, pp. 081501 (10 pp.).

Bang, K. H., Kim, K. K., Lee, S. K., and Lee, B. W., 2011, "Pressure effect on flow boiling heat transfer of water in minichannels", International Journal of Thermal Sciences, 50, pp. 280-286.

Barber, J., Sefiane, K., Brutin, D., and Tadrist, L., 2009, “Hydrodynamics and heat transfer during flow boiling instabilities in a single microchannel”, Applied Thermal Engineering, 29, pp. 1299-1308.

Barlak, S., Yapc, S., and Sara, O. N., 2011, “Experimental investigation of pressure drop and friction factor for water flow in microtubes”, International Journal of Thermal Sciences, 50, pp. 361-368.

Basu, S., Ndao, S., Michna, G. J., Peles, Y., and Jensen, M. K., 2011, “Flow Boiling of R134a in Circular Microtubes-Part I: Study of Heat Transfer Characteristics”, J HEAT TRAN-T ASME, 133, pp. 051502 (9 pp.).

Basu, S., Ndao, S., Michna, G. J., Peles, Y., and Jensen, M. K., 2011, “Flow Boiling of R134a in Circular Microtubes-Part II: Study of Critical Heat Flux Condition”, J HEAT TRAN-T ASME, 133, pp. 051503 (9 pp.).

Beattie, D. R. H., and Whalley, P. B., 1982, “A Simplified Two-Phase Frictional Pressure Drop Prediction Method,” Int. J. Multiphase Flow, 8, pp. 83– 87.

Bertsch, S. S., Groll, E. A., and Garimella, S. V., 2009, “A composite heat transfer correlation for saturated flow boiling in small channels”, International Journal of Heat and Mass Transfer, 52, pp. 2110-2118.

Blasius, H., 1913, Das Ähnlichkeitsgesetz bei Reibungvorgägen in Flüssigkeiten, Forchg. Arb. Ing. -Wes., No. 131, Berlin.

Boure, J. A., Bergles, A. E., and Tong, L. S., 1973, “Review of two-phase flow instability”, Nuclear Engineering and Design, 25, pp. 165-92.

Bowers, M. B. and Mudawar, I., 1994, “High flux boiling in low flow rate, low pressure drop mini-channel and micro-channel heat sinks”, International Journal of Heat and Mass Transfer, 37, pp. 321-32.

Celata, G. P., Cumo, M, Dossevi, D., Jilisen, R .T. M., Saha, S. K., and Zummo, G., 2011, “Visualisation of flow boiling heat transfer in a microtube”, Heat and Mass Transfer, 47, pp. 941-949.

Celata, G. P., Saha, S. K., Zummo, G., and Dossevi, D., 2010, “Heat transfer characteristics of flow boiling in a single horizontal microchannel”, International Journal of Thermal Sciences, 49, pp. 1086-1094.

Chedester, R. C., and Ghiaasiaan, S. M., 2002, “A proposed mechanism for hydrodynamically-controlled onset of significant void in microtubes”, International Journal of Heat and Fluid Flow, 23, pp.769–775.

Cheng, P., and Wu, H. Y., 2006, “Mesoscale and microscale phase-change heat transfer”, Advances in Heat Transfer, 39, pp. 461-563.

Chisholm, D., 1973, “Pressure gradients due to friction during the flow of evaporation two-phase mixtures in smooth tubes and channels”, International Journal of Heat and Mass Transfer, 16, pp. 347– 358.

Choi, C., Shin, J. S., Yu, D. I., and Kim, M. H., 2011, “Flow boiling behaviors in hydrophilic and hydrophobic microchannels”, Experimental Thermal and Fluid Science, 35, pp. 816-824.

Cicchitti, A., Lombardi, C., Silvestri, M., Soldaini, G., and Zavattarelli, R., 1960, “Two-Phase Cooling Experiments—Pressure Drop, Heat Transfer and Burnout Experiments,” Energia Nucleare, 7, pp. 407–425.

Coleman, J. W., 2004, "An Experimentally Validated Model for Two-Phase Sudden Contraction Pressure Drop in Microchannel Tube Headers", Heat Transfer Engineering, 25, pp. 69-77.

Davidson, W. F., Hardie, P. H., Humphreys, C. G. R., Markson, A. A., Mumford, A. R., and Ravese, T., 1943, "Studies of Heat Transmission Through Boiler Tubing at Pressures from 500-3300 Lbs", Trans. ASME, 65, pp. 553-591.

Ding, Y., Kakac, S., and Chen, X. J., 1995, "Dynamic instabilities of boiling two-phase flow in a single horizontal channel", Experimental Thermal and Fluid Science, 11, pp. 327-342.

Diza, M. C., and Schmidt, J., 2007, "Experimental investigation of transient boiling heat transfer in microchannels", International Journal of Heat and Fluid Flow, 28, pp. 95-102.

Dukler, A. E., Wicks, M., and Cleveland, R. G., 1964, "Pressure Drop and Hold-Up in Two-Phase Flow. Part A—A Comparison of Existing Correlation, Part B—An Approach Through Similarity Analysis," AIChE J., 10, pp. 38– 43.

Fang, R., Jiang, W., and Khan, J., 2011, "Experimental study on the effect of synthetic jet on flow boiling instability in a microchannel", Proceedings of ASME 9th International Conference on Nanochannels, Microchannels, and Minichannels.

Farhadi, K. 2009, "A model for predicting static instability in two-phase flow systems", Progress in Nuclear Energy, 51, pp. 805-12.

Filonenko, G. K., 1954, "Hydraulic resistance in pipes", Teploenergetika, 1, pp. 40-44.

Galvis, E., and Culham, R., 2012, “Measurements and flow pattern visualization of two-phase flow boiling in single channel microevaporators”, International Journal of Multiphase Flow, 42, pp.52-61.

García, F., García, R., Padrino, J. C., Mata, C., Trallero J. L., and Joseph, D. D., 2003, “Power Law and Composite Power Law Friction Factor Correlations for Laminar and Turbulent Gas-Liquid Flow in Horizontal Pipelines”, International Journal of Multiphase Flow, 29, pp. 1605-1624.

Ghajar, A. J., Tang, C. C., and Cook, W. L., 2010, “Experimental investigation of friction factor in the transition region for water flow in minitubes and microtubes”, Heat Transfer Engineering, 31, pp. 646-657.

Gnielinski, V., 1976, “New Equations for Heat Transfer in Turbulent Pipe and Channel Flow.” International Chemical Engineering, 16, pp. 359-368.

Grigull, U. and Tratz, H., 1965, “Thermischer Einlauf in Ausgebildeter Laminarer Rohrströmung”, Int. J. Heat Mass Transfer, 8, pp. 669–678.

Hall, D. D. and Mudawar, I., 2000, “Critical heat flux (CHF) for water flow in tubes. II. Subcooled CHF correlations”, International Journal of Heat and Mass Transfer, 43, pp. 2605-40.

Harirchian, T. and Garimella, S. V., 2008, “Microchannel size effects on local flow boiling heat transfer to a dielectric fluid”, International Journal of Heat and Mass Transfer, 51, pp. 3724-35.

Harirchian, T. and Garimella, S. V., 2009, “Effects of channel dimension, heat flux, and mass flux on flow boiling regimes in microchannels”, International Journal of Multiphase Flow, 35, pp. 349-362.

Hassan, I., 2006, “Thermal MEMS Devices: A Decade of Progress and Challenges Ahead,” ASME Journal of Heat Transfer, 128, pp. 1221-1233.

Huh, C., Kim, J., and Kim, M. H., 2007, “Flow pattern transition instability during flow boiling in a single microchannel”, International Journal of Heat and Mass Transfer, 50, pp. 1049-1060.

Huo, X., Chen, L., Tian, Y. S., and Karayiannis, T. G., 2004, “Flow boiling and flow regimes in small diameter tubes”, Applied Thermal Engineering, 24, pp. 1225-39.

Hwang, Y. W. and Kim, M. S., 2006, “The pressure drop in microtubes and the correlation development”, International Journal of Heat and Mass Transfer, 49, pp. 1804-1812.

Inasaka, F., Nariai, H., and Shimura, T., 1989, “Pressure drops in subcooled flow boiling in narrow tubes”, Heat Transfer - Japanese Research, 18, pp. 70-82.

Jiang, L., Wong, M., and Zohar, Y., 2001, “Forced convection boiling in a microchannel heat sink”, Journal of Microelectromechanical Systems, 10, pp. 80-87.

Kakac, S. and Bon, B., 2008, “A review of two-phase flow dynamic instabilities in tube boiling systems”, International Journal of Heat and Mass Transfer, 51, pp. 399-433.

Kandlikar, S. G. and Balasubramanian, P., 2004, “An Extension of the Flow Boiling Correlation to Transition, Laminar, and Deep Laminar Flows and Microchannels”, Heat Transfer Engineering, 25, pp. 86-93.

Kandlikar, S. G., 2006, “Nucleation characteristics and stability considerations during flow boiling in microchannels”, Experimental Thermal and Fluid Science, 30, pp. 441-447.

Kandlikar, S. G., and Grande, W. J., 2002, “Evolution of microchannel flow passages-thermohydraulic performance and fabrication technology”, Proceedings of IMECE2002, ASME International Mechanical Engineering Congress & Exposition, November 17-22, New Orleans, Louisiana.

Kandlikar, S. G., Kuan, W. K., Willistein, D. A., and Borrelli, J., 2006, “Stabilization of flow boiling in microchannels using pressure drop elements and fabricated nucleation sits”, ASME Journal of Heat Transfer, 128, pp. 389-396.

Katto, Y., and Ohno, H., 1984, “An improved version of the generalized correlation of critical heat for the forced convective boiling in uniformly heated vertical tubes”, International Journal of Heat and Mass Transfer, 27, pp. 1641-1648.

Kennedy, J. E., Roach, G. M., Dowling, M. F., Abdel-Khalik, S. I., Ghiaasiaan, S. M., Jeter, U. M., and Quershi, Z. H., 2000, “The onset of flow instability in uniformly heated horizontal microchannels”, ASME. Journal of Heat Transfer, 122, pp. 118-125.

Kew, P., and Cornwell, K., 1997, “correlations for prediction of boiling heat transfer in small diameter channels”, Applied Thermal Engineering, 17, pp. 705-715.

Khater, H. A., El-Morshdy, S. E-D., and Ibrahim, M. A., 2007, “Thermal-hydraulic modeling of the onset of flow instability in MTR reactors”, Annals of Nuclear Energy, 34, pp. 194-200.

Kuznetsov, V. V. and Shamirzaev, A. S., 2009, “Flow Boiling Heat Transfer in Two-Phase Micro Channel Heat Sink at Low Water Mass Flux”, Microgravity Science and Technology, 21, pp. S305-11.

Lazarek, G. M., and Black, S. H., 1982, “Evaporative heat transfer, pressure drop and critical heat flux in a small vertical tube with R-113”, International Journal of Heat and Mass Transfer, 25, pp. 945-60.

Lee, H.J., and Lee, S.Y., 2001, “Heat transfer correlation for boiling flows in small rectangular horizontal channels with low aspect ratios”, International Journal of Multiphase Flow, 27, pp. 2043– 2062.

Lee, J. and Mudawar, I., 2009, “Critical heat flux for subcooled flow boiling in micro-channel heat sinks”, International Journal of Heat and Mass Transfer, 52, pp. 3341-3352.

Lee, J., and Mudawar, I., 2008, “Fluid flow and heat transfer characteristics of low temperature two-phase micro-channel heat sinks – Part 1: Experimental methods and flow visualization results”, International Journal of Heat and Mass Transfer, 51, pp. 4315-4326.

Lee, J., and Mudawar, I., 2005, “Two-phase flow in high-heat flux micro-channel heat sink for refrigeration cooling applications: Part I – pressure drop characteristics”, International Journal of Heat and Mass Transfer, 48, pp. 928-940.

Lee, S. C., and Bankoff S. G, 1993, “Prediction of the onset of flow instability in transient subcooled flow boiling”, Nuclear Engineering and Design, 139, pp. 149-159.

Lee, S.C., and Bankoff, S.G., 1998, “A comparison of predictive models for the onset of significant void at low pressures in forced-convection subcooled boiling”, Journal of Mechanical Science and Technology, 12, pp. 504-513.

Levy, S., 1967, "Forced convection subcooled boiling-prediction of vapor volumetric fraction", International journal of heat and mass transfer, 10, pp. 951-965.

Lew, P. A., and Cornwell, K., 1997, "Correlations for the prediction of boiling heat transfer in small-diameter channels", Applied Thermal Engineering, 17, pp. 705-715.

Lin, S., Kwok, C. C. K., Li, R. Y., Chen, Z. H., and Chen, Z. Y., 1991, "Local frictional pressure drop during vaporization of R-12 through capillary tubes" International Journal of Multiphase Flow, 17, pp. 95-102.

Lin, T-Y and Yang, C-Y, 2007, "An experimental investigation on forced convection heat transfer performance in micro tubes by the method of liquid crystal thermography", International Journal of Heat and Mass Transfer, 50, pp. 4736-4742.

Liu, D and Garimella, S. V., 2007, "Flow boiling heat transfer in microchannels", Journal of Heat Transfer, 129, pp. 1321-1332.

Liu, G., Xu, J., Yang, Y., and Zhang, W., 2010, "Active control of flow and heat transfer in silicon microchannels", Journal of Micromechanics and Microengineering, 20, pp. 045006 (16 pp.).

Lockhart, R.W. and Martinelli, R.C., 1949, "Proposed correlation of data for isothermal two-phase, two-component flow in pipes", Chemical Engineering Progress. 45 pp. 39–48.

Maranzana, G., Perry, I., and Maillet, D., 2004, "Mini- and micro-channels: influence of axial conduction in the walls", International Journal of Heat and Mass Transfer, 47, pp. 3993-4004.

Mauro, A. W., Thome, J. R., Toto, D., and Vanoli, G. P., 2010, “Saturated critical heat flux in a multi-microchannel heat sink fed by a split flow system”, Experimental Thermal and Fluid Science, 34, pp.81-92.

McAdams, W. H., Woods, W. K., and Bryan, R. L., 1942, “Vaporisation Inside Horizontal Tubes-II-Benzene–Oil Mixtures,” ASME J. Heat Transfer, 64, pp. 193–200.

Mishima, K., Hibiki, T., 1996, “Some characteristics of air–water two-phase flow in small diameter vertical tubes”, International Journal of Multiphase Flow, 22, pp.703–712.

Moffat, R. J., 1988, “Describing the uncertainties in experimental results”, Experimental Thermal and Fluid Science, 1, pp. 3-17.

Munson, B. R., Young, D. F., Okiishi, T. H., and Huebsch, W. W., Fundamentals of fluid mechanics, New Jersey: John Wiley &Sons, 2009.

Muwanga, R. and Hassan, I., 2006, “Local heat transfer measurements in microchannels using liquid crystal thermography: methodology development and validation”, J HEAT TRAN-T ASME, 128, pp. 617-26.

Muwanga, R., Hassan, I., and MacDonald, R., 2007, “Characteristics of flow boiling oscillations in silicon microchannel heat sinks”, Transactions of the ASME. Journal of Heat Transfer, 129, pp. 1341-51.

Oh, Jong-Taek, Pamitran, A. S., Choi, Kwang-Il, and Hrnjak, P., 2011, “Experimental investigation on two-phase flow boiling heat transfer of five refrigerants in horizontal small tubes of 0.5, 1.5 and 3.0 mm inner diameters”, International Journal of Heat and Mass Transfer, 54, pp. 2080-2088.

Owens, W. L., 1961, “Two -Phase Pressure Gradient”, ASME International Developments in Heat Transfer, Part II, pp. 363-368.

Park, J. E., and Thome, J. R., 2010, “Critical heat flux in multi-microchannel copper elements with low pressure refrigerants”, International Journal of Heat and Mass Transfer, 53, pp. 110-122.

Park, J. E., Thome, J. R., and Michel, B., 2009, “Effect of inlet orifice on saturated CHF and flow visualization in multi-microchannel heat sinks”, 25th Annual IEEE Semiconductor Thermal Measurement and Management Symposium, pp. 1-8.

Qi, S. L., Zhang, P., Wang, R. Z., and Xu, L. X., 2007 (a), “Flow boiling of liquid nitrogen in micro-tubes: part II - heat transfer characteristics and critical heat flux”, International Journal of Heat and Mass Transfer, 50, pp. 5017-30.

Qi, S. L., Zhang, P., Wang, R. Z., and Xu, L. X., 2007 (b), “Single-phase pressure drop and heat transfer characteristics of turbulent liquid nitrogen flow in micro-tubes”, International Journal of Heat and Mass Transfer, 50, pp. 1993-2001.

Qu, W. and Mudawar, I., 2004, “Measurement and correlation of critical heat flux in two-phase micro-channel heat sinks”, International Journal of Heat and Mass Transfer, 47, pp. 2045-2059.

Qu, W., and Mudawar, I., 2003, “Flow boiling heat transfer in two-phase micro-channel heat sinks - I. Experimental investigation and assessment of correlation methods”, International Journal of Heat and Mass Transfer, 46, pp. 2755-2771.

Qu, W., and Mudawar, I., 2003, “Measurement and prediction of pressure drop in two-phase microchannel heat sinks”, International Journal of Heat and Mass Trasnfer, 46, pp. 2737-2753.

Rands, C., Webb, B. W., and Maynes, D., 2006, “Characterization of transition to turbulence in microchannels”, International Journal of Heat and Mass Transfer, 49, pp. 2924-2930.

Revellin, R., and Thome, J. R., 2007, “A new type of diabatic flow pattern map for boiling heat transfer in microchannels”, Journal of Micromechanics and Microengineering, 17, pp. 788-796.

Revellin, R., and Thome, J. R., 2008, “A theoretical model for the prediction of the critical heat flux in heated microchannels”, International Journal of Heat and Mass Transfer, 51, pp.1216-1225.

Roach, G. M., Abdel-Khalik, S. I., Ghiaasiaan, S. M., Dowling, M. F., and Jeter, S. M., 1999, “Low-Flow Onset of Flow Instability in Heated Microchannels”, Nuclear Science and Engineering, 133, pp. 106-117.

Roday, A. P., and Jensen, M. K., 2009, “Study of the critical heat flux condition with water and R-123 during flow boiling in microtubes. Part I: Experimental results and discussion of parametric effects”, International Journal Heat and Mass Transfer, 52, pp. 3235-3249.

Roday, A. P., and Jensen, M. K., 2009, “Study of the critical heat flux condition with water and R-123 during flow boiling in microtubes. Part II: Comparison of data with correlations and establishment of a new subcooled CHF correlation”, International Journal Heat and Mass Transfer, 52, pp. 3250-3256.

Rogers, J. T., Salcudean, M., Abdullah, Z., McLeod, D., and Poirier, D., 1987, “The onset of significant void in up-flow boiling of water at low pressure and velocities”, International Journal of Heat and Mass Transfer, 30, pp. 2247-2260.

Saha, P., and Zuber, N., 1974, “Point of net vapor generation vapor void fraction in subcooled boiling”, Proceedings of the fifth international heat transfer conference, Tokyo, Japan.

Saisorn, S., Kaew-On, J., and Wongwises, S., 2010, “Flow pattern and heat transfer characteristics of R-134a refrigerant during flow boiling in a horizontal circular mini-channel”, International Journal of Heat and Mass Transfer, 53, pp. 4023-38.

Saitoh, S., Daiguji, H., and Hihara, E., 2005, “Effect of tube diameter on boiling heat transfer of R-134a in horizontal small-diameter tubes”, International Journal of Heat and Mass Transfer, 48, pp. 4973-84.

Saiton, S., Daiguji, H., and Hihara, E., 2007, “Correlation for boiling heat transfer of R-134a in horizontal tubes including effect of tube diameter”, International Journal of Heat and Mass Transfer, 50, pp. 5215-5225.

Schilder, B., Man, S. Y. C., Kasagi, N., Hardt, S., and Stephan, P., 2010, “Flow visualization and local measurement of forced convection heat transfer in a microtube”, J HEAT TRANS-T ASME, 132, pp. 031702 (9 pp.).

Sekoguchi, K., Nishikawa, K., Nakasatomi, M., Hirata, No., and Higuchi, H., 1974, “Flow boiling in subcooled and low quality regions - heat transfer and local void fraction”, Proceedings of fifth international heat transfer conference, pp. 180-184.

Shin, J. Y., Kim, M. S., and Ro, S. T., 1997m “Experimental study on forced convective boiling heat transfer of pure refrigerants and refrigerant mixtures in a horizontal tube”, International Journal of Refrigeration, 20, pp. 267-275.

Staub, F. W., 1968, “The void fraction in subcooled boiling - Prediction of the initial point of net vapor generation”, ASME Journal of Heat Transfer, 90, pp. 151-157.

Steinke, M. E., and Kandlikar, S. G., 2004, “An experimental investigation of flow boiling characteristics of water in parallel microchannels”, ASME Journal of Heat Transfer, 126, pp. 518-526.

Stelling, R. McAssey, E.V., Jr., Dougherty, T., and Yang, B.W, 1996, “The onset of flow instability for downward flow in vertical channels”, J HEAT TRANS-T ASME, 118, pp. 709-714.

Stoddard, R. M., Blasick, A. M., Ghiaasiaan S. M., Abdel-Khalik, S. I., Jeter, S. M., and Dowling M. F., 2002, “Onset of flowinstability and criticalheatflux in thinhorizontalannuli”, Experimental Thermal and Fluid Science, 26, pp. 1-14.

Tam, L. M., Tam, H. K., and Ghajar, A. J., 2011, “Simultaneous Heat Transfer and Pressure Drop Measurements for a Horizontal Micro-Tube”, Proceedings of ASME/JSME 2011 8th Thermal Engineering Joint Conference, Honolulu, Hawaii, USA.

Thome, J. R., 2004, “Boiling in microchannels: A review of experiment and theory”, International Journal of Heat and Fluid Flow, 25, pp. 128-139.

Tran, T. N., Wambsganss, M. W., and France, D. M., 1996, “Small circular- and rectangular-channel boiling with two refrigerants”, International Journal of Multiphase Flow, 22, pp. 485-98.

Tran, T.N., Chyu, M.C., Wambsganss, M.W., and France, D.M., 2000, “Two-phase pressure drop of refrigerants during flow boiling in small channels: an experimental investigation and correlation development”, International Journal of Multiphase Flow, 26, pp. 1739–1754.

Ullmann, A., and Brauner, N., 2007, “The prediction of flow pattern maps in minichannels”, Multiphase Sceience and Technology, 19, pp. 49-73.

Unal, H. C., 1975, “Determination of the initial point of net vapor generation in flow boiling systems”, International Journal of Heat and Mass Transfer, 18, pp. 1095-1099.

Wang, G. and Cheng, P., 2008, “An experimental study of flow boiling instability in a single microchannel”, International Communications in Heat and Mass Transfer, 35, pp. 1229-1234.

Wang, G., Cheng, P., and Bergles, A. E., 2008, “Effects of inlet/outlet configurations on flow boiling instability in parallel microchannels”, International Journal of Heat and Mass Transfer, 51, pp. 2267-2281.

Wang, G., Cheng, P., and Wu, H., 2007, “Unstable and stable flow boiling in parallel microchannels and in a single microchannel”, International Journal of Heat and Mass Transfer, 50, pp. 4297-4310.

Wang, Q., Chen, X. J., Kakac, S., and Ding, Y., 1994, “An experimental investigation of density-wave-type oscillations in a convective boiling upflow system”, International Journal of Heat and Fluid Flow, 15, pp. 241-246.

Wang, Q., Chen, X. J., Kakac, S., and Ding, Y., 1996, “Boiling onset oscillation: A new type of dynamic instability in a forced-convection upflow boiling system”, International Journal of Heat and Fluid Flow, 17, pp. 418-423.

Warrier, G. R., Dhir, V. K., and Momoda, L. A., 2002, “Heat transfer and pressure drop in narrow rectangular channels”, Experimental Thermal and Fluid Science, 26, pp. 53-64.

Whittle, R.H., and Forgan, R., 1967, “A correlation for the minima in the pressure drop versus flow-rate curves for sub-cooled water flowing in narrow heated channels”, Nuclear Engineering and Design, 6, pp. 89–99.

Wojtan, L., Revellin, R., and Thome, J. R., 2006, “Investigation of saturated critical heat flux in a single, uniformly heated microchannel”, Experimental Thermal and Fluid Science, 30, pp. 765-774.

Wu, H. Y., and Chen, P., 2003, “Boiling instability in parallel silicon microchannels at different heat flux”, International Journal of Heat and Mass Transfer, 47, pp. 3631-3641.

Wu, H. Y., and Cheng, P., 2003, “Liquid/two-phase/vapor alternating flow during boiling in microchannels at high heat flux”, International Communications in Heat and Mass Transfer, 30, pp. 295-302.

Wu, Z., Li, W., and Ye, S., 2011, “Correlations for saturated critical heat flux in microchannels”, International Journal of Heat and Mass Transfer, 54, pp. 379-389.

Xu, J. L., Zhou, J. J., Gan, Y. H., and Chen, Y., 2004, “Unsteady flow phenomenon in a heated microchannel at high heat fluxes”, Experimental Heat Transfer, 17, pp. 299-319.

Xu, J., Liu, G., Zhang, W., Li, Q., and Wang, B., 2009, “Seed bubbles stabilize flow and heat transfer in parallel microchannels”, International Journal of Multiphase Flow, 35, pp.773-790.

Xu, J., Zhou, J., and Gan, Y., 2005, “Static and dynamic flow instability of a parallel microchannel heat sink at high heat fluxes”, Energy Conversion and Management, 46, pp. 313-334.

Yang, C-Y, Wu, J-C, Chien, H-T, and Lu, S-R, 2003, "Friction characteristics of water, R-134a, and air in small tubes", Microscale Thermophysical Engineering, 7, pp. 335-348.

Yen, T.-H., Shoji, M., Takemura, F., Suzuki, Y., and Kasagi, N., 2006, "Visualization of convective boiling heat transfer in single microchannels with different shaped cross-sections", International Journal of Heat and Mass Transfer, 49, pp. 3884-3894.

Yen, T-H, Kasagi, N., and Suzuki, Y., 2003, "Forced convective boiling heat transfer in microtubes at low mass and heat fluxes", International Journal of Multiphase Flow, 29, pp. 1771-1792.

Yu, W., France, D.M., Wambsganss, M.W., and Hull, J.R., 2002 "Two phase pressure drop, boiling heat transfer, and critical heat flux to water in a small-diameter horizontal tube", International Journal of Multiphase Flow, 28, pp.927–941.

Zhang, W., Hibiki, T., Mishima, K., and Mi, Y., 2006, "Correlation of critical heat flux for flow boiling of water in mini-channels", International Journal of Heat and Mass Transfer, 49, pp. 1058-1072.

Publications

Journal Papers

1. Fan, Y. F. and Hassan, I. G., 2013, "Effect of Inlet Restriction on Flow Boiling Heat Transfer in a Horizontal Microtube", *J. Heat Transfer*, v 135, 021502.
2. Fan, Y. F. and Hassan, I. G., 2012, "Experimental Investigation of Flow Boiling Instability in a Single Horizontal Microtube with and without Inlet Restriction", *J. Heat Transfer,* v 134, 081501.
3. Fan, Y. F. and Hassan, I. G., 2013, "Prediction of Onset of Flow Instability in Single Microchannel with Inlet Restriction", *ready to submit.*

Referred Conference Proceedings

1. Fan, Y. F. and Hassan, I. G., "The Effect of Inlet Orifice on Critical Heat Flux and Flow Boiling Heat Transfer Coefficient in a Single Horizontal Microtube", *ASME 2013 Summer Heat Transfer Conference*, Minneapolis, MN, USA, July 14-16, 2013.
2. Fan, Y. F. and Hassan, I. G., "New Predictive Methodology of the Onset of Flow Instability in a Horizontal Microtube with Inlet Orifice", *ASME 2013 Summer Heat Transfer Conference*, *ASME 2013 Summer Heat Transfer Conference*, Minneapolis, MN, USA, July 14-16, 2013.
3. Fan, Y. F. and Hassan, I. G., "Experimental Investigation of Flow Boiling Instability in a Single Horizontal Microtube with Inlet Orifice", *2013 the 2nd international conference on Fluid Dynamics and Thermodynamics Technologies*, Istanbul, Turkey, March 15-16, 2013.

4. Fan, Y. F. and Hassan, I. G., “Numerical Investigation of a Swirl Micro Heat Sink”, *ASME 2011 9th International Conference on Nanochannels, Microchannels, and Minichannels*, Edmonton, Alberta, Canada, June 19-22, 2011.
5. Fan, Y. F. and Hassan, I. G., “Numerical Simulation of a Novel Jet-Impingement Micro Heat Sink with Cross Flow Under Non Uniform Heating Condition”, *ASME 2011 9th International Conference on Nanochannels, Microchannels, and Minichannels*, Edmonton, Alberta, Canada, June 19-22, 2011.

Conference Presentation

6. Fan. Y. F. and Hassan, I. G., “The Effect of Inlet Orifice on Flow Boiling Heat Transfer in a Single Microtube”, *CSME International Congress – 2012*, Winnipeg, Manitoba, Canada, June 4-6, 2012.

Poster

7. Fan, Y. F. and Hassan, I. G., “The Effect of Orifice on Flow Boiling Instability in a Single Horizontal Microtube”, *Sixth International Conference on Two-Phase Systems for Ground and Space Applications*, Cava de’ Tirreni (Napoli), Italy, September 25-28, 2011.

Appendix A: FC-72 Properties

Table A.1: Saturation Properties of FC-72

P	T_{sat}	C_p	h_{fg}	μ	ρ_l	ρ_v
(kPa)	(°C)	(J/kg·K)	(J/kg)	(Pa·s)	(kg/m^3)	(kg/m^3)
8.61	0	1011	99182	9.50E-04	1755	1.37
11.6	5	1019	98000	8.74E-04	1738	1.8
14.6	10	1026	96818	8.00E-04	1720	2.23
19	15	1034	95593	7.43E-04	1706	2.86
23.5	20	1042	94369	6.87E-04	1692	3.48
30	25	1050	93094	6.44E-04	1680	4.36
36.6	30	1057	91820	6.01E-04	1669	5.23
45.7	35	1065	90497	5.68E-04	1659	6.41
54.7	40	1073	89174	5.35E-04	1650	7.59
67.2	45	1080	87789	5.09E-04	1641	9.14
79.5	50	1088	86404	4.83E-04	1631	10.7
96	55	1096	84970	4.61E-04	1623	12.7
101	56.6	1098	84511	4.54E-04	1620	13.4
112	60	1104	83536	4.39E-04	1614	14.8
134	65	1111	82046	4.18E-04	1603	17.5
155	70	1119	80557	3.98E-04	1593	20.2
182	75	1127	79024	3.80E-04	1581	23.7
209	80	1135	77492	3.62E-04	1569	27.2
243	85	1142	75928	3.43E-04	1554	31.6
276	90	1150	74365	3.25E-04	1539	36
317	95	1158	72783	3.20E-04	1520	41.5
359	100	1165	71201	3.14E-04	1501	47
409	105	1173	69447	3.08E-04	1477	53.8
459	110	1181	67693	3.03E-04	1453	60.6
519	115	1189	65994	2.96E-04	1424	69.1

Table A. 1 (*continued*)

579	120	1196	64295	2.90E-04	1394	77.5
650	125	1204	62215	2.82E-04	1357	88
721	130	1212	60134	2.74E-04	1321	98.6
805	135	1219	57642	2.65E-04	1277	112
889	140	1227	55149	2.56E-04	1233	126
987	145	1235	52059	2.45E-04	1180	144
1085	150	1243	48969	2.34E-04	1128	162
1199	155	1250	45048	2.21E-04	1065	189
1313	160	1258	41128	2.08E-04	1003	215
1446	165	1266	35693	1.93E-04	930	259
1579	170	1274	30258	1.78E-04	858	303
1733	175	1281	12459	1.48E-04	714	485
1825	178	1286	1780	1.30E-04	628	594

Appendix B: Experimental Data

B.1 Two-phase Pressure Drop

Table B.1: in the microtube without inlet orifice at G = 160 kg/m^2·s

T_{in} = 23°C; P_{sat} = 10 kPa		**T_{in} = 23°C; P_{sat} = 45 kPa**		**T_{in} = 35°C; P_{sat} = 10 kPa**	
χ_7	ΔP (kPa)	χ_7	ΔP (kPa)	χ_7	ΔP (kPa)
0.35672	2.292394	0.094626	1.503416	0.18773	1.42112
0.441305	2.763788	0.157511	1.813379	0.27388	2.00525
0.567753	3.679494	0.240954	2.29702	0.3845	2.70234
0.707624	4.519324	0.322073	2.672174	0.49294	3.36786
0.795243	4.686131	0.417068	3.128428	0.61196	4.0379
0.891987	4.873281	0.503624	3.563714	0.65768	4.32929
		0.547763	3.788734	0.71684	4.5129
		0.645461	3.949622	0.75385	4.63275

Table B.2: in the microtube without inlet orifice at G = 295 kg/m^2·s

T_{in} = 23°C; P_{sat} = 10 kPa		**T_{in} = 23°C; P_{sat} = 45 kPa**		**T_{in} = 35°C; P_{sat} = 10 kPa**	
χ_7	ΔP (kPa)	χ_7	ΔP (kPa)	χ_7	ΔP (kPa)
0.037814	2.705619	0.023496	2.682735	0.211225	5.63278
0.11083	3.497597	0.086238	3.582068	0.280016	7.051678
0.182771	4.793592	0.170237	4.786261	0.35974	8.557139
0.265607	6.276818	0.260626	6.129415	0.437203	10.27569
0.348772	7.8946	0.362155	7.619034	0.464731	10.7779
0.435438	9.773532	0.456998	9.075198	0.557139	11.51829
0.52646	11.36231	0.561309	10.65361	0.650887	13.23063
0.629977	13.11218	0.670448	12.02151	0.748396	14.44531
0.730929	14.71539	0.794761	12.91462	0.808023	14.7598
0.79829	15.26891	0.801768	12.6573		
0.840656	15.38608				

Table B.3: in the microtube without inlet orifice at $G = 420$ kg/m^2·s

T_{in} = 23°C; P_{sat} = 10 kPa		**T_{in} = 23°C; P_{sat} = 45 kPa**		**T_{in} = 35°C; P_{sat} = 10 kPa**	
χ_7	ΔP (kPa)	χ_7	ΔP (kPa)	χ_7	ΔP (kPa)
0.00925	4.103458	0.006741	4.097189	0.00898	4.20128
0.049096	5.325267	0.067823	5.394961	0.07418	6.10013
0.111989	6.860877	0.135166	7.012724	0.12329	7.68464
0.174802	8.864088	0.207905	8.850818	0.18062	9.77151
0.238144	11.14685	0.285188	10.95624	0.24276	11.9459
0.307702	13.67835	0.364223	13.41561	0.30177	14.187
0.382421	16.33483	0.448716	15.85335	0.36699	16.7653
0.456192	18.86826	0.535321	18.33245	0.43235	19.2961
0.534972	21.87379	0.613899	20.96987	0.48297	21.1207
0.61698	24.5693	0.71613	23.01247	0.58224	25.1052
0.697503	27.14581	0.806749	24.21029	0.65569	27.6929
0.784998	28.7389	0.830246	23.92916	0.70658	29.5076
0.829491	28.8465			0.79423	30.3943
0.846764	28.80831			0.81612	30.3804

Table B.4: in the microtube without inlet orifice at $G = 550$ kg/m^2·s

T_{in} = 23°C; P_{sat} = 10 kPa		**T_{in} = 23°C; P_{sat} = 45 kPa**		**T_{in} = 35°C; P_{sat} = 10 kPa**	
χ_7	ΔP (kPa)	χ_7	ΔP (kPa)	χ_7	ΔP (kPa)
0.034712	7.713919	0.017676	6.754372	0.021956	5.137384
0.088417	9.818744	0.075129	8.947738	0.071319	6.776427
0.140125	12.53946	0.129178	11.31702	0.104702	8.400972
0.199855	15.24609	0.19589	13.933	0.155027	10.57994
0.255412	18.29107	0.264794	16.78223	0.212674	13.35835
0.312911	21.78591	0.335941	20.43731	0.271017	16.57888
0.378334	25.21855	0.404527	23.77104	0.3289	20.04283
0.440639	28.82188	0.479008	26.82836	0.393021	23.85532
0.506587	32.32906	0.551461	29.99685	0.456576	27.87376
0.574536	35.97453	0.631805	33.84898	0.523801	32.10306
0.648524	39.35418	0.718167	36.73389	0.588582	36.46377
0.721514	42.54411	0.771853	36.5456	0.664684	40.64206
0.797943	44.30942			0.742563	44.88293
0.861045	44.69661			0.820219	48.46315
				0.900297	50.4697
				0.923929	51.10175

Table B.5: in the microtubes with inlet orifices G = 160 kg/m^2·s

T_{in} = 23°C; P_{sat} = 10 kPa			
50%		**20%**	
χ_7	**ΔP (kPa)**	**χ_7**	**ΔP (kPa)**
0.071030624	0.77655	0.079194	0.719887
0.131931915	1.00137	0.232575	2.548786
0.200469728	1.30522	0.351307	3.27652
0.305532184	2.05003	0.472635	4.030066
0.402180247	2.4725	0.597011	4.941614
0.486117003	3.1195	0.734766	5.895467
0.612041953	3.86965	0.77602	6.014123
0.752220218	4.36738	0.820191	6.162501
0.803826508	4.23434		

Table B.6: in the microtubes with inlet orifices G = 295 kg/m^2·s

T_{in} = 23°C; P_{sat} = 10 kPa			
50%		**20%**	
χ_7	**ΔP (kPa)**	**χ_7**	**ΔP (kPa)**
0.032887991	2.24636	0.026842	4.374905
0.081303697	3.25697	0.082917	5.059321
0.141853854	3.59147	0.15514	6.175217
0.203231522	4.71761	0.231864	7.467576
0.261204958	5.16266	0.31746	8.97079
0.317115903	6.50445	0.401537	10.31778
0.4249552	7.80285	0.494948	12.12586
0.535013524	8.92115	0.593054	14.00561
0.625440322	9.87817	0.662801	15.05598
0.707687721	10.455	0.768215	16.78312
0.760631	10.5563	0.875353	17.59072
		0.887164	17.61616

Table B.7: in the microtubes with inlet orifices G = 420 kg/m^2·s

T_{in} = 23°C; P_{sat} = 10 kPa			
50%		**20%**	
χ_7	**ΔP (kPa)**	**χ_7**	**ΔP (kPa)**
0.027200537	4.43209	0.037959	8.216697
0.061687357	5.34954	0.094204	9.744548
0.101669081	6.31108	0.1571	11.45438
0.14406492	7.61325	0.22197	13.39402
0.20369049	9.57021	0.290476	15.75205
0.29179043	11.8407	0.359133	18.13256
0.346008365	13.2947	0.435367	20.94522
0.49039505	17.8952	0.511157	23.65722
0.63133144	22.3295	0.592055	26.56877
0.677382935	23.2738	0.675078	29.48235
0.720321911	23.2146	0.756985	31.83884
0.762326874	23.4371	0.787631	31.00998
		0.811536	30.75694

Table B.8: in the microtubes with inlet orifices G = 550 kg/m^2·s

T_{in} = 23°C; P_{sat} = 10 kPa			
50%		**20%**	
χ_7	**ΔP (kPa)**	**χ_7**	**ΔP (kPa)**
0.007980591	7.00362	0.009233	11.00004
0.083197734	10.2674	0.060934	12.79886
0.152674692	13.7572	0.112669	14.99558
0.244837429	17.2122	0.164189	17.36487
0.323266663	20.5542	0.220925	20.1493
0.374026472	23.9763	0.276697	23.24756
0.470995336	26.6335	0.337851	26.63836
0.522202201	31.286	0.400038	29.95545
0.606701355	33.5886	0.464128	33.47709
0.641296851	35.1345	0.532777	37.21567
0.66668625	36.5522	0.597752	40.98584
		0.678268	43.052
		0.718776	46.7833
		0.793639	50.27267
		0.845929	48.73561

Table B.9: in the microtube with 20% inlet orifice

T_{in} = 23°C; P_{sat} = 45 kPa							
G = 160 kg/m^2·s		**G = 295 kg/m^2·s**		**G = 420 kg/m^2·s**		**G = 550 kg/m^2·s**	
χ_7	**ΔP (kPa)**	**χ_7**	**ΔP (kPa)**	**χ_7**	**ΔP (kPa)**	**χ_7**	**ΔP (kPa)**
0.073137	1.041265	0.094961	5.097433	0.03813	8.092094	0.018636	11.93724
0.217629	2.536557	0.180169	6.152724	0.106069	9.571546	0.081322	13.84781
0.343688	3.136469	0.266082	7.334704	0.183513	11.52372	0.139956	16.22513
0.47687	3.780875	0.361144	8.740638	0.254123	13.27784	0.208118	18.90854
0.609745	4.537691	0.4599	10.2919	0.326785	15.51193	0.267563	21.8035
0.710392	5.050838	0.564891	11.84358	0.410813	17.89551	0.336654	24.73497
0.744627	4.830748	0.673339	13.33193	0.491543	20.34729	0.411651	28.35502
		0.781422	14.49696	0.580627	23.07792	0.484586	31.96404
		0.846344	15.01275	0.67326	25.96848	0.559407	35.39624
		0.854431	14.65482	0.768153	28.15997	0.640679	39.30988
				0.830071	28.60744	0.717285	42.4165
				0.848262	28.25461	0.796579	45.13167
						0.897361	48.30945

B.2 Critical Heat Flux

Table B.10: in the microtubes with and without inlet orifice

	G (kg/m^2·s)	**q"$_{CHF}$ (kW/m^2)**		
		Without inlet orifice	**50%**	**20%**
T_{in} = 23 °C **P_{sat} = 10 kPa**	160	31.24710728	32.14930055	32.59481913
	200	36.35453389		
	260	50.34758812	50.00199912	51.20233699
	300	55.41515917		
	395	70.89801667	71.16396588	76.51463846
	450	78.9328047		
	520	98.59504383	91.96776635	97.41303898
	550	113.8918586	119.2271261	106.1406753
	650	69.89833177	94.89807258	121.0251356
	760	82.1402137	106.2481475	149.4995625
	870	92.15474473	132.9728403	177.5634211
T_{in} = 35 °C **P_{sat} = 10 kPa**	160	30.51446541		32.7082
	295	61.01067269		63.16532
	420	89.00867816		90.73467
	550	116.063765		122.2169
T_{in} = 23 °C **P_{sat} = 45 kPa**	160	26.29577795		26.92156
	295	50.97098695		52.21905
	420	75.3148298		77.54
	550	103.8605036		105.96

B.3 Flow Boiling Heat Transfer Coefficient

Table B.11: G = 160 kg/m^2·s, T_{in} = 23 °C, and P_{sat} = 10 kPa

Without inlet orifice										
q" (kW/m^2)	χ_3	χ_4	χ_5	χ_6	χ_7	h_3 (kW/m^2·°C)	h_4 (kW/m^2·°C)	h_5 (kW/m^2·°C)	h_6 (kW/m^2·°C)	h_7 (kW/m^2·°C)
16.6			0.050	0.132	0.215			22901.42	10934.89	12813.09
18.4			0.102	0.193	0.284			14605.07	10757.03	11431.28
20.5		0.064	0.165	0.267	0.369		15109.13	12703.46	9477.51	10712.66
22.3		0.110	0.221	0.332	0.443		14163.66	11566.73	9435.52	8385.10
25.4	0.062	0.189	0.316	0.443	0.569	11990.57	12842.49	12511.10	8555.30	6526.34
27.6	0.106	0.244	0.382	0.520	0.657	14485.92	13149.43	12308.68	7403.57	5130.11
28.7	0.129	0.272	0.416	0.559	0.702	14546.93	12799.38	10558.03	5560.50	2635.29
29.5	0.145	0.292	0.440	0.587	0.734	10457.19	10740.84	7422.52	5480.97	1676.19
20% inlet orifice										
17.50			0.095	0.186	0.276			27927.24	5588.69	11920.59
20.41		0.078	0.183	0.287	0.392		13360.80	16316.72	6310.47	10177.44
23.42	0.034	0.154	0.274	0.393	0.513	11251.11	13748.37	18495.32	7431.62	7964.70
26.50	0.095	0.230	0.364	0.499	0.634	8666.59	10501.09	15141.80	8482.10	6705.70
29.89	0.164	0.316	0.467	0.619	0.771	7573.08	11540.80	13377.29	7969.10	6063.24
30.92	0.183	0.340	0.497	0.653	0.809	8050.32	15453.49	51080.16	9775.77	5228.79
32.01	0.211	0.374	0.537	0.700	0.863	7486.64	15445.24	28914.06	7129.77	1608.05

Table B.12: G = 160 kg/m^2·s, T_{in} = 35 °C, and P_{sat} = 10 kPa

Without inlet orifice										
q" (kW/m^2)	χ_3	χ_4	χ_5	χ_6	χ_7	h_3 (kW/m^2·°C)	h_4 (kW/m^2·°C)	h_5 (kW/m^2·°C)	h_6 (kW/m^2·°C)	h_7 (kW/m^2·°C)
16.14		0.099	0.181	0.262	0.344		15149.33	11188.72	9143.35	11415.64
18.24	0.069	0.162	0.255	0.347	0.440	18283.12	12970.29	11028.60	9988.61	10507.90
20.11	0.102	0.205	0.307	0.409	0.511	18055.89	15540.99	11994.48	10233.12	8084.99
22.12	0.143	0.255	0.368	0.481	0.593	15448.66	12612.36	11751.98	9828.53	6075.94
24.11	0.186	0.309	0.432	0.554	0.677	13846.12	13159.76	12789.07	8890.98	5952.16
25.19	0.209	0.337	0.465	0.593	0.722	13274.73	11445.27	7956.46	6141.42	3338.76
26.30	0.233	0.367	0.501	0.634	0.768	11479.13	13975.14	9433.54	5554.56	1623.31
20% inlet orifice										
19.42	0.095	0.195	0.294	0.394	0.494	15081.58	29833.65	39129.96	7243.62	8769.36
22.28	0.154	0.268	0.382	0.496	0.610	10914.26	27663.35	26025.22	5564.00	8173.19
25.30	0.225	0.355	0.485	0.614	0.744	8357.54	14790.40	11923.37	4395.94	3964.06
26.92	0.263	0.402	0.541	0.679	0.818	7606.73	11808.32	8877.53	3434.41	1952.61
28.06	0.299	0.445	0.592	0.738	0.885	4605.07	6574.38	4274.09	2172.32	871.05

Table B.13: G = 160 kg/m^2·s, T_{in} = 23 °C, and P_{sat} = 45 kPa

Without inlet orifice										
q" (kW/m^2)	χ_3	χ_4	χ_5	χ_6	χ_7	h_3 (kW/m^2·°C)	h_4 (kW/m^2·°C)	h_5 (kW/m^2·°C)	h_6 (kW/m^2·°C)	h_7 (kW/m^2·°C)
17.18					0.110					15815.13
18.86				0.076	0.173				15725.52	21593.43
20.77			0.043	0.150	0.256			18523.63	15491.59	17993.63
22.77			0.104	0.221	0.338			15168.80	19471.69	19698.95
24.95		0.049	0.177	0.305	0.433		34687.93	13595.54	16804.85	17204.72
27.05		0.103	0.242	0.381	0.520		42443.36	14844.88	15745.90	15655.89
28.08		0.131	0.276	0.420	0.564		20830.74	14268.05	13445.27	13450.97
20% inlet orifice										
19.99			0.046	0.151	0.257			111793.57	7356.27	34611.49
23.05		0.022	0.144	0.265	0.387		148498.23	81492.17	8254.76	23455.50
26.28		0.106	0.245	0.384	0.522		182825.60	73714.78	9440.78	21104.52
29.50	0.034	0.190	0.346	0.502	0.658	15512.20	17294.24	22638.62	10144.25	17707.60
31.77	0.089	0.257	0.424	0.591	0.759	16470.02	23306.43	35149.33	10814.02	11080.85
32.71	0.113	0.288	0.462	0.636	0.811	17008.16	32935.06	737895.87	9004.30	1206.80

Table B.14: G = 295 kg/m^2·s, T_{in} = 23 °C, and P_{sat} = 10 kPa

Without inlet orifice										
q" (kW/m^2)	χ_3	χ_4	χ_5	χ_6	χ_7	h_3 (kW/m^2·°C)	h_4 (kW/m^2·°C)	h_5 (kW/m^2·°C)	h_6 (kW/m^2·°C)	h_7 (kW/m^2·°C)
21.34					0.025					10730.39
23.23					0.066					10235.02
26.51				0.063	0.139				7017.47	10578.80
29.71			0.039	0.125	0.210			7711.83	6595.27	9873.52
33.45		0.004	0.101	0.197	0.293		17532.86	8119.21	7699.15	10304.15
37.16		0.054	0.161	0.267	0.374		13106.66	7983.37	7702.06	10649.60
41.01		0.106	0.224	0.343	0.461		11526.63	7543.18	7452.01	11151.28
45.04	0.031	0.162	0.292	0.422	0.552	13085.80	10839.97	7434.49	7598.00	11534.70
49.55	0.081	0.224	0.367	0.510	0.652	17361.35	13169.80	8464.11	8817.62	11239.50
54.00	0.129	0.286	0.441	0.597	0.751	19395.73	14893.48	10466.24	11243.92	11190.91
56.96	0.162	0.326	0.490	0.653	0.816	22702.75	16309.05	10709.38	13913.12	11031.26
58.83	0.188	0.358	0.528	0.698	0.866	18254.15	15782.80	11530.28	15271.45	3698.64
20% inlet orifice										
22.89										8137.37
25.46				0.039	0.113				4918.23	8703.03
28.72			0.018	0.101	0.185			11290.98	5149.97	8639.68
32.15			0.074	0.167	0.261			10805.01	5510.47	8966.93
35.96		0.032	0.137	0.241	0.346		11483.39	10448.93	6036.83	10240.38
39.66		0.084	0.199	0.314	0.429		11124.44	10650.71	6619.90	10988.01
43.78	0.013	0.140	0.267	0.394	0.521	10113.02	10739.97	10533.12	7248.16	11318.14
48.10	0.059	0.199	0.339	0.478	0.617	9625.62	10770.87	11663.17	7972.83	12537.00
51.16	0.093	0.241	0.390	0.538	0.685	10901.71	11734.93	14331.74	11166.04	12085.13
55.83	0.143	0.305	0.467	0.628	0.789	11337.19	12606.73	16184.76	12843.92	10796.69
60.54	0.198	0.374	0.549	0.724	0.898	11088.14	12993.44	19361.69	16544.56	4256.81
61.06	0.207	0.385	0.562	0.739	0.915	11883.11	13815.17	22003.07	17767.92	2160.26

Table B.15: G = 295 kg/m^2·s, T_{in} = 35 °C, and P_{sat} = 10 kPa

Without inlet orifice										
q" (kW/m^2)	χ_3	χ_4	χ_5	χ_6	χ_7	h_3 (kW/m^2·°C)	h_4 (kW/m^2·°C)	h_5 (kW/m^2·°C)	h_6 (kW/m^2·°C)	h_7 (kW/m^2·°C)
26.40		0.049	0.125	0.202	0.278		75694.38	10510.83	14696.97	9181.35
29.77	0.011	0.098	0.185	0.271	0.358	55863.92	29079.34	9752.30	9408.65	10775.46
33.38	0.052	0.150	0.247	0.344	0.441	43259.64	23091.39	9524.67	8915.58	11910.89
34.58	0.066	0.167	0.268	0.368	0.469	18252.66	16078.01	8208.29	8324.19	10466.68
38.23	0.104	0.217	0.328	0.440	0.551	17116.77	14542.73	8473.36	9166.05	10799.69
42.50	0.160	0.284	0.408	0.532	0.656	22252.85	11404.32	8343.69	8848.16	10214.38
46.58	0.207	0.344	0.480	0.616	0.751	21578.48	16345.11	9512.58	8625.22	8235.41
50.97	0.259	0.409	0.558	0.706	0.854	28955.94	19412.18	10066.97	8560.44	4262.03
20% inlet orifice										
27.58		0.073	0.154	0.235	0.316		16248.96	14620.50	7302.35	8914.33
32.23	0.041	0.136	0.231	0.326	0.420	9185.96	10912.63	11789.50	7389.40	8981.82
35.98	0.079	0.186	0.292	0.397	0.503	8996.29	10557.95	12905.92	8039.92	10453.59
39.72	0.121	0.238	0.355	0.472	0.589	8342.93	9616.07	11716.25	7901.80	10620.98
43.87	0.165	0.295	0.424	0.553	0.682	7955.80	9673.64	12330.22	9100.11	9221.01
48.08	0.212	0.354	0.495	0.636	0.777	8384.42	12079.17	18822.33	12813.29	9173.98
50.75	0.246	0.397	0.546	0.695	0.844	8487.95	8548.77	8162.01	5192.50	3856.08
52.22	0.267	0.422	0.577	0.731	0.885	10257.24	10023.29	9213.91	5107.63	2029.65

Table B.16: G = 295 kg/m^2·s, T_{in} = 23 °C, and P_{sat} = 45 kPa

q" (kW/m^2)	χ_3	χ_4	χ_5	χ_6	χ_7	h_3 (kW/m^2·°C)	h_4 (kW/m^2·°C)	h_5 (kW/m^2·°C)	h_6 (kW/m^2·°C)	h_7 (kW/m^2·°C)
Without inlet orifice										
27.79					0.047					30426.52
30.65				0.022	0.112					30783.96
34.33				0.095	0.196					28599.36
38.05			0.063	0.175	0.287			29690.98	14082.45	24021.35
42.19		0.017	0.142	0.267	0.391		59166.57	35374.70	16878.92	22126.71
46.37		0.074	0.211	0.348	0.485		52398.69	29407.94	16337.43	25267.09
50.71		0.141	0.291	0.441	0.591		33227.06	22663.13	19161.82	24215.61
55.49	0.043	0.208	0.373	0.538	0.702	28150.73	23823.25	18549.70	15740.69	19647.83
60.68	0.106	0.286	0.466	0.645	0.824	45693.69	30201.00	34303.55	25057.99	16534.05
61.01	0.113	0.295	0.476	0.657	0.837	32305.40	33432.77	27943.44	29926.13	2886.28
20% inlet orifice										
30.66				0.029	0.120				8087.40	33113.74
34.34			0.003	0.105	0.207			33055.53	7588.41	27028.62
38.21			0.069	0.183	0.296			25526.70	7536.70	23620.52
42.21		0.015	0.141	0.266	0.392		17380.42	13988.12	6663.35	21670.54
46.36		0.076	0.214	0.352	0.490		23144.51	17887.09	7265.57	20508.99
50.94		0.140	0.292	0.444	0.595		19121.52	18250.72	7833.50	25651.17
55.49	0.042	0.208	0.373	0.538	0.703	15363.03	17110.22	17755.58	9004.30	24037.52
60.10	0.096	0.275	0.454	0.632	0.810	14294.13	16555.63	18957.35	10963.27	14853.62
62.72	0.132	0.319	0.506	0.692	0.878	14895.09	17506.98	22759.83	12984.71	4988.25
63.17	0.141	0.330	0.519	0.708	0.896	16600.06	17990.66	21094.82	11892.83	1903.48

Table B.17: G = 420 kg/m^2·s, T_{in} = 23 °C, and P_{sat} = 10 kPa

q" (kW/m^2)	χ_3	χ_4	χ_5	χ_6	χ_7	h_3 (kW/m^2·°C)	h_4 (kW/m^2·°C)	h_5 (kW/m^2·°C)	h_6 (kW/m^2·°C)	h_7 (kW/m^2·°C)
Without inlet orifice										
31.92					0.030					10634.00
34.45				0.001	0.070				8325.68	10220.12
38.46				0.055	0.132				9382.08	10325.43
42.47			0.023	0.109	0.194			9871.22	7977.23	10334.53
46.52			0.068	0.162	0.256			9427.77	8423.80	10415.50
50.96		0.013	0.117	0.221	0.324		19243.86	9769.07	8843.29	11100.78
55.75		0.056	0.170	0.284	0.397		20670.32	10891.06	9953.92	12354.72
60.46		0.099	0.223	0.346	0.469		19760.40	11277.49	10372.44	13301.26
65.50	0.008	0.144	0.278	0.412	0.546	27361.60	17144.07	11149.21	10485.22	13713.25
70.74	0.045	0.192	0.337	0.482	0.627	23655.90	17291.18	11196.46	11262.71	14726.79
75.96	0.080	0.238	0.394	0.550	0.705	36211.61	20609.14	12168.64	12397.83	14942.03
81.59	0.121	0.290	0.459	0.626	0.792	27716.00	22893.75	13487.48	13441.31	15234.53
84.45	0.144	0.319	0.493	0.666	0.837	37877.81	24896.53	17464.58	13028.09	8923.54
85.57	0.154	0.331	0.508	0.683	0.857	30552.71	23531.78	17609.77	22952.92	4712.68
20% inlet orifice										
29.82					0.004					10213.16
33.51					0.059					10358.76
37.17				0.039	0.115				5956.86	10500.26
41.16			0.009	0.093	0.177			12380.32	6356.04	10034.13
45.26			0.055	0.148	0.241			12332.77	6600.49	10522.46
49.59		0.003	0.106	0.208	0.309		10166.97	9766.18	6594.20	10656.28
53.98		0.043	0.154	0.266	0.376		11023.14	9883.27	6413.51	10692.07
58.87		0.087	0.209	0.330	0.451		10136.54	9587.58	6999.49	11725.66
63.73		0.130	0.262	0.394	0.525		11156.51	11085.66	7728.53	14574.15
68.91	0.033	0.177	0.320	0.463	0.604	11969.48	12393.96	12269.70	7734.32	13837.28
74.25	0.070	0.225	0.380	0.533	0.686	10588.91	10834.22	11669.95	8428.53	14609.31
79.56	0.106	0.273	0.438	0.603	0.767	10048.40	10813.04	11806.63	9252.13	14950.85
81.50	0.125	0.296	0.465	0.634	0.801	11242.76	12739.49	11987.88	6533.35	5853.23
83.05	0.142	0.317	0.490	0.663	0.834	11466.46	12846.77	11047.75	6255.30	2011.56

Table B.18: $G = 420$ kg/m^2·s, $T_{in} = 35$ °C, and $P_{sat} = 10$ kPa

q" (kW/m^2)	χ_3	χ_4	χ_5	χ_6	χ_7	h_3 (kW/m^2·°C)	h_4 (kW/m^2·°C)	h_5 (kW/m^2·°C)	h_6 (kW/m^2·°C)	h_7 (kW/m^2·°C)
Without inlet orifice										
25.03				0.019	0.071				7247.33	10643.47
28.72			0.010	0.069	0.127			8824.08	6641.11	9511.40
31.06			0.037	0.101	0.164			7946.71	7023.33	9287.40
34.54		0.004	0.076	0.147	0.218		16238.17	7387.70	6812.67	9527.31
38.41		0.040	0.119	0.198	0.278		16878.25	8080.65	7402.71	9914.62
42.31		0.075	0.162	0.250	0.338		16119.41	8986.61	8304.39	10799.78
46.74	0.017	0.115	0.213	0.310	0.407	20440.56	14554.77	9032.58	8838.04	12050.63
50.98	0.046	0.153	0.260	0.366	0.472	21503.87	15336.04	9578.18	9708.86	13633.83
55.67	0.077	0.195	0.311	0.428	0.543	21299.33	15440.77	9924.55	9744.67	14776.88
60.31	0.115	0.242	0.369	0.495	0.621	17005.32	13698.25	9203.05	9542.39	15052.77
65.57	0.151	0.290	0.428	0.566	0.702	17530.42	14640.58	9711.66	9421.89	15025.64
74.02	0.214	0.370	0.525	0.680	0.834	26899.82	17454.79	10970.47	14126.44	13525.35
75.31	0.227	0.386	0.544	0.702	0.858	25279.95	19077.70	13580.29	17709.89	3909.17
20% inlet orifice										
40.86					0.061					45886.92
44.87				0.035	0.129				8776.40	36762.52
49.40				0.103	0.206				7608.64	30856.15
53.98			0.050	0.163	0.276			18959.17	7953.28	39540.11
58.48			0.102	0.224	0.347			24981.23	8180.51	36334.09
63.69		0.029	0.163	0.297	0.430		21150.42	19048.26	8326.63	34982.98
68.75		0.075	0.220	0.365	0.509		22765.42	22808.87	10177.38	35785.44
74.11		0.129	0.286	0.442	0.597		19127.08	18521.94	9369.51	33925.45
79.68	0.016	0.185	0.354	0.522	0.689	16858.47	17315.56	17531.16	9454.78	32711.70
85.64	0.059	0.241	0.422	0.603	0.782	19199.99	20053.75	20387.18	11312.29	36748.15
89.42	0.091	0.281	0.470	0.658	0.845	19021.85	19130.19	20586.85	12089.29	16599.71
90.73	0.103	0.296	0.488	0.680	0.870	16571.76	17501.39	18224.26	12788.04	3324.75

Table B.19: G = 420 kg/m^2·s, T_{in} = 23 °C, and P_{sat} = 45 kPa

Without inlet orifice										
q" (kW/m^2)	χ_3	χ_4	χ_5	χ_6	χ_7	h_3 (kW/m^2·°C)	h_4 (kW/m^2·°C)	h_5 (kW/m^2·°C)	h_6 (kW/m^2·°C)	h_7 (kW/m^2·°C)
38.46					0.028					43528.88
42.34				0.002	0.089				22771.92	36648.35
46.39				0.060	0.156				17433.10	31967.54
50.84			0.018	0.123	0.228			17789.15	13823.36	33161.64
55.49			0.075	0.190	0.304			16114.07	14388.90	30665.62
60.56			0.131	0.257	0.383			16822.58	17306.38	36006.61
65.61		0.055	0.192	0.329	0.465		148651.06	16761.19	17627.66	36825.31
70.89		0.107	0.255	0.403	0.551		126933.05	19565.67	19841.01	37877.00
75.62		0.154	0.312	0.470	0.628		71863.42	17468.36	17616.63	35786.79
81.99		0.216	0.388	0.560	0.731		59484.45	15476.23	17004.22	34927.07
87.37	0.090	0.274	0.457	0.639	0.820	356206.90	56771.21	16935.61	19635.53	26757.87
89.01	0.103	0.291	0.478	0.664	0.849	47514.44	33676.56	16962.97	17746.69	4550.54
20% inlet orifice										
22.35					0.028					172685.81
26.44				0.040	0.093				11868.14	48438.61
29.67			0.022	0.082	0.143			13379.87	11106.89	34160.31
33.24			0.064	0.132	0.200			12706.32	10174.38	25835.77
37.24		0.033	0.110	0.186	0.263		16902.23	15594.07	11967.05	30090.49
41.07		0.067	0.152	0.237	0.322		16029.52	18573.26	13337.33	35637.26
45.23	0.011	0.106	0.200	0.294	0.388	28573.42	13827.95	12720.19	11335.64	23862.43
49.43	0.040	0.144	0.248	0.351	0.454	21804.15	13446.68	14005.54	13022.78	24021.00
52.48	0.065	0.176	0.286	0.396	0.505	33635.35	16187.08	15815.36	13334.97	22829.96
58.79	0.110	0.235	0.359	0.482	0.605	24503.83	14657.33	15975.93	14734.20	24612.07
63.57	0.143	0.278	0.413	0.547	0.679	28869.20	15948.13	17598.95	15599.90	28598.98
66.99	0.165	0.308	0.450	0.591	0.731	16810.03	16211.11	18591.95	15267.46	34040.82
72.59	0.210	0.364	0.517	0.669	0.821	20347.31	19972.44	30834.61	21366.98	40806.76
73.95	0.222	0.379	0.534	0.689	0.843	24842.85	22972.60	32221.72	34668.73	7509.49

Table B.20: G = 550 kg/m^2·s, T_{in} = 23 °C, and P_{sat} = 10 kPa

q" (kW/m^2)	χ_3	χ_4	χ_5	χ_6	χ_7	h_3 (kW/m^2·°C)	h_4 (kW/m^2·°C)	h_5 (kW/m^2·°C)	h_6 (kW/m^2·°C)	h_7 (kW/m^2·°C)
Without inlet orifice										
39.95					0.006					11078.89
43.83					0.052					10649.90
48.29				0.029	0.104				10368.62	10208.03
52.58				0.072	0.154				9216.18	10707.17
57.52			0.032	0.122	0.213			11050.30	9636.19	11085.22
62.17			0.069	0.168	0.266			9997.50	9848.88	11699.08
67.05		0.001	0.109	0.216	0.323		22649.17	10310.48	10182.99	12621.44
72.57		0.037	0.154	0.270	0.386		22226.86	10684.97	10777.28	13128.20
77.82		0.071	0.197	0.323	0.447		22096.66	11327.59	10555.98	13614.55
83.49		0.106	0.242	0.377	0.511		22510.74	11644.19	11340.36	14285.73
89.37		0.143	0.289	0.434	0.578		22862.09	12586.42	11937.83	15716.07
95.73	0.025	0.183	0.340	0.496	0.650	38156.86	26586.19	14367.83	12971.67	17181.14
102.03	0.054	0.223	0.391	0.557	0.722	45040.42	29542.29	14609.02	13939.64	18449.43
108.56	0.089	0.269	0.447	0.624	0.799	51960.15	32597.74	16155.54	17202.77	19541.32
113.89	0.121	0.308	0.495	0.680	0.863	40391.74	29198.71	17493.91	15525.42	9807.22
20% inlet orifice										
38.77					0.026					13010.87
42.85				0.007	0.077				7530.96	12840.34
45.63				0.052	0.129				7133.77	12125.63
49.78			0.011	0.095	0.179			10108.32	6732.79	12035.29
54.56			0.050	0.142	0.234			11421.79	7396.87	12533.47
59.35			0.089	0.189	0.289			10598.58	7036.85	13039.96
64.11		0.022	0.131	0.240	0.349		10541.40	9777.79	6997.89	13916.81
69.40		0.056	0.174	0.292	0.409		11848.79	11384.74	7661.25	14861.53
74.64		0.090	0.218	0.346	0.472		11619.46	11332.13	7935.41	16056.45
80.18		0.128	0.266	0.403	0.539		12009.44	12358.13	8576.38	17540.35
85.51	0.013	0.162	0.311	0.458	0.604	12256.37	11630.30	11550.93	8565.44	19297.73
91.76	0.051	0.211	0.370	0.528	0.684	12355.12	12261.15	12366.06	9056.55	21168.80
98.15	0.062	0.230	0.396	0.560	0.723	12682.05	12661.79	13321.57	9582.01	18657.69
104.54	0.092	0.271	0.448	0.623	0.797	14128.54	14379.53	15183.47	10523.70	18072.62
111.15	0.124	0.309	0.493	0.675	0.855	14803.32	15676.83	19182.78	9668.50	4861.11

Table B.21: G = 550 kg/m^2·s, T_{in} = 35 °C, and P_{sat} = 10 kPa

Without inlet orifice										
q" (kW/m^2)	χ_3	χ_4	χ_5	χ_6	χ_7	h_3 (kW/m^2·°C)	h_4 (kW/m^2·°C)	h_5 (kW/m^2·°C)	h_6 (kW/m^2·°C)	h_7 (kW/m^2·°C)
33.44				0.028	0.081				7747.36	17916.54
37.12			0.005	0.065	0.124			8907.34	7040.06	10219.00
41.16			0.041	0.107	0.173			8555.18	7223.68	9698.39
45.16			0.072	0.145	0.218			8465.29	7664.56	9718.88
49.56		0.027	0.108	0.189	0.269		21007.95	8985.75	8157.65	10048.84
54.15		0.057	0.146	0.234	0.322		25305.29	9519.80	8502.78	10682.76
58.90		0.087	0.184	0.281	0.377		18920.44	8950.12	9332.80	11444.78
63.91	0.013	0.119	0.225	0.331	0.435	253618.80	24391.10	10412.15	9644.75	12500.98
69.07	0.037	0.153	0.267	0.382	0.495	167874.26	23273.59	10856.94	10671.11	13965.15
74.24	0.064	0.189	0.313	0.436	0.559	614054.71	24821.67	10908.70	10745.46	15487.44
79.71	0.088	0.223	0.357	0.490	0.622	21866.89	17075.41	10176.83	10577.98	16160.30
85.53	0.116	0.261	0.405	0.548	0.690	41819.21	22998.87	11432.51	11982.04	17658.18
91.25	0.146	0.301	0.455	0.608	0.759	89409.83	24413.02	11930.03	12647.34	18559.64
101.13	0.199	0.370	0.540	0.709	0.876	108768.87	30434.48	13255.97	14344.04	20015.10
103.86	0.218	0.394	0.569	0.742	0.913	73285.62	34555.40	15656.50	19751.44	4825.33
20% inlet orifice										
32.34				0.010	0.061				16301.32	28280.09
34.20				0.027	0.081				15885.55	20754.96
36.02				0.046	0.103				11933.25	16062.63
39.62			0.023	0.087	0.150			15436.06	12656.42	12640.34
43.81			0.059	0.130	0.200			11903.61	10569.74	12330.07
48.22		0.016	0.095	0.173	0.251		24581.65	13281.85	12577.28	13235.73
52.47		0.044	0.130	0.216	0.301		27928.03	14618.27	13074.68	14957.32
57.25		0.075	0.169	0.263	0.357		20895.11	14093.01	12769.15	14670.40
62.13	0.003	0.107	0.210	0.313	0.415	113425.40	22787.04	15399.26	14063.73	15861.13
67.03	0.025	0.138	0.250	0.361	0.472	43300.37	17391.62	14131.91	12778.49	16866.41
72.12	0.048	0.169	0.291	0.411	0.530	109086.09	19637.42	14983.22	16707.40	17945.03
77.54	0.071	0.203	0.334	0.464	0.593	28860.96	23109.44	16717.55	16758.42	18374.51
83.24	0.098	0.240	0.381	0.521	0.659	36052.08	28276.85	18918.28	17974.96	19327.69
89.13	0.126	0.278	0.429	0.579	0.728	38756.68	37254.29	22633.60	21448.77	21039.17
96.54	0.168	0.332	0.496	0.657	0.818	42822.21	37289.72	26222.68	25991.41	23782.30
99.34	0.185	0.354	0.522	0.688	0.853	47615.36	44527.54	25883.10	23572.91	17047.02
106.14	0.230	0.410	0.588	0.764	0.939	46172.08	40092.66	25767.25	25963.79	3881.94

Table B.22: G = 550 kg/m^2·s, T_{in} = 23 °C, and P_{sat} = 45 kPa

Without inlet orifice										
q" (kW/m^2)	χ_3	χ_4	χ_5	χ_6	χ_7	h_3 (kW/m^2·°C)	h_4 (kW/m^2·°C)	h_5 (kW/m^2·°C)	h_6 (kW/m^2·°C)	h_7 (kW/m^2·°C)
52.56					0.035					69707.55
57.07				0.002	0.092				22647.43	64552.25
61.75				0.046	0.145				24052.62	56968.12
66.80				0.104	0.210				19759.14	51601.36
72.59			0.044	0.161	0.277			25769.29	21347.62	50012.26
78.08			0.095	0.221	0.347			22706.13	22656.10	49434.12
83.53		0.007	0.143	0.279	0.414		334186.42	21504.44	21013.94	49196.94
89.68		0.049	0.195	0.341	0.487		164968.69	21773.97	19857.89	49659.69
95.53		0.089	0.246	0.402	0.557		147369.65	22302.25	23349.78	55155.29
101.70		0.136	0.304	0.470	0.636		126840.75	22483.96	22791.50	56234.57
108.55		0.188	0.367	0.545	0.722		211400.06	23865.40	23490.78	56388.56
113.06	0.040	0.228	0.415	0.601	0.785	372077.87	119012.55	29148.87	16114.89	2578.79
20% inlet orifice										
52.22					0.035					30479.61
56.91				0.005	0.097				11361.59	25474.81
61.95				0.055	0.155				9893.58	24059.53
67.15			0.004	0.113	0.223			21137.69	9428.52	20264.35
71.86			0.045	0.163	0.281			19256.91	9038.84	19499.93
77.54			0.094	0.222	0.349			19295.26	9892.88	21294.70
83.28		0.010	0.148	0.285	0.422		20010.35	18214.60	9745.55	20120.77
88.95		0.051	0.199	0.346	0.493		21323.98	21071.90	10746.89	19533.26
95.14		0.093	0.252	0.410	0.567		20596.20	21196.81	10623.87	19950.59
101.50		0.140	0.310	0.479	0.647		18208.20	18305.86	10916.59	20000.89
107.99	0.000	0.183	0.364	0.544	0.722	22219.50	20547.88	20239.88	11699.82	30832.66
114.23	0.037	0.230	0.421	0.611	0.800	19845.48	19760.15	20288.54	12799.17	40958.27
122.22	0.087	0.294	0.499	0.703	0.905	22583.98	21879.92	23428.88	15015.78	4771.15

B.4 Flow Instability

Table B.23: onset of flow instability and onset of flow re-stability

T_{in} = 23 °C and P_{sat} = 17 kPa					
Onset of flow instability				**Onset of flow re-stability**	
G (kg/m^2·s)	**q"$_{OFI}$ (W/cm^2)**	**G (kg/m^2·s)**	**q"$_{OFI}$ (W/cm^2)**	**G (kg/m^2·s)**	**q"(W/cm^2)**
693.872	5.560058	1777.943	13.53169	434.046	15.45968
763.234	6.387411	1835.640	14.64585	434.047	15.7351
829.849	6.569908	1893.908	15.06832	447.050	15.89245
904.973	7.256794	2067.855	16.24307	498.434	15.89245
977.308	8.621944	2069.462	15.50518	536.309	16.20716
1045.944	8.078997	2124.184	16.70268	548.808	17.38945
1166.134	9.515758	2125.837	17.00636	585.926	17.38945
1183.260	8.945267	2241.802	19.70805	646.527	18.52049
1274.934	9.968889	2412.744	19.38029	670.326	19.3003
1327.850	10.45364	2589.695	22.78191	688.009	19.3003
1344.262	10.44334	2696.826	20.87693	740.207	19.95929
1546.014	12.46161	2990.448	26.62111	785.533	21.44766
1603.996	12.72122	2995.571	26.26928	915.452	23.50929

Table B.24: oscillation features at the onset of flow instability

T_{in} = 23 °C and P_{sat} = 17 kPa			
G(kg/m^2·s)	**f (Hz)**	**AMP (kPa)**	**MAG (kPa)**
763.234	0.79013	2.635199	28.55465
977.308	0.108703	6.820001	33.02059
1166.134	0.084562	14.12808	29.83341
1327.850	0.041599	16.73276	31.36536
1546.014	0.027189	17.07351	32.2829
1835.640	0.022193	25.56928	37.0145
2124.184	0.019166	28.12641	40.17824
2412.744	0.016941	32.51978	46.73939
2696.826	0.019018	32.73384	52.16761
2990.448	0.227404	32.52242	73.40794

Table B.25: onset of flow instability in the microtubes with inlet orifices

50% inlet orifice		35% inlet orifice		20% inlet orifice	
G ($kg/m^2 \cdot s$)	**q''_{OFI} (W/cm^2)**	**G ($kg/m^2 \cdot s$)**	**q''_{OFI} (W/cm^2)**	**G ($kg/m^2 \cdot s$)**	**q''_{OFI} (W/cm^2)**
762.878	6.67625	762.878	7.975299	762.759	11.6828
818.737	7.666463	818.737	8.722778	818.228	12.9904
925.725	8.190847	925.725	9.282967	925.149	15.0724
1026.403	8.836061	1026.403	10.2	1026.083	17.4515
1165.046	9.859683	1165.046	10.56549		
1250.300	10.68979	1250.300	12.04321		
1328.470	11.55295	1328.470	12.70255		
1435.154	12.0632	1545.533	14.1944		
1545.533	12.84062	1834.498	17.13127		
1834.784	15.48794	2122.532	19.02559		
2121.210	20.62929	2410.490	27		
2411.617	24.09702				